PhD-FSTM-2026-071
The Faculty of Science, Technology and Medicine

DISSERTATION

Defence held on 17/06/2026 in Luxembourg

to obtain the degree of

DOCTEUR DE L'UNIVERSITÉ DU LUXEMBOURG

EN INFORMATIQUE

by

Carlos Luis MARCOS ROJAS

COMBINING TECHNIQUES FOR THE RECEPTION OF SIGNALS FROM SATELLITE CONSTELLATIONS WITH PATH DIVERSITY AT THE USER TERMINAL

Dissertation defence committee

Dr Juan Carlos Merlano Duncan, dissertation supervisor
Research Scientist, Université du Luxembourg

Dr Joel Grotz
Senior Manager, SES S.A., Luxembourg.

Dr Eva Lagunas, Chair
Assistant Professor, Université du Luxembourg

Dr Ignacio Rodríguez Larrad
Ramón y Cajal Research Fellow, University of Oviedo

Dr Symeon Chatzinotas,
Professor, Université du Luxembourg

Combining Techniques for the Reception of Signals from Satellite Constellations with Path Diversity at the User Terminals

Carlos Luis Marcos Rojas

Abstract

The large-scale deployment of non-terrestrial networks (NTNs) based on non-geostationary orbit (NGSO) satellite constellations is transforming the design paradigm of satellite communication systems. The availability of multiple simultaneously visible satellites at the user terminal (UT) enables the exploitation of spatial diversity through cooperative transmission. However, practical realization of such techniques is severely constrained by symbol-level time misalignment caused by differential propagation delays, satellite motion, and heterogeneous onboard clocks. These impairments fundamentally challenge the applicability of classical transmit-diversity techniques, such as space–time block coding (STBC), which rely on strict synchronization assumptions that are rarely satisfied in realistic satellite environments.

This doctoral thesis investigates the feasibility of combining signals from distributed satellite transmitters at the user terminal under realistic timing, synchronization, and hardware constraints. The research focuses on UT-assisted diversity combining strategies that do not rely on global channel state information at the gateway and that remain robust to symbol-time misalignment. A comprehensive modeling framework is first developed to characterize waveform misalignment resulting from differential orbital dynamics and clock mismatch in low Earth orbit (LEO) constellations. Based on this model, a novel sample time misalignment estimation and distributed compensation architecture is proposed, combining coarse frame-level synchronization with fine symbol-time tracking using delay-locked loop and Kalman-filter-based techniques for the estimation, and a distributed control loop between UT and satellite for the compensation.

Building on this synchronization framework, the thesis introduces a low-complexity UT receiver architecture capable of combining STBC-encoded signals under imperfect symbol-time alignment. The proposed approach explicitly incorporates time-misalignment information into the diversity-combining process, enabling effective mitigation of inter-symbol interference induced by asynchronous waveform arrival. An analytical formulation of the com-

bining scheme is presented, along with an efficient numerical implementation that exploits block-circulant matrix structures and Fourier-domain processing to significantly reduce computational complexity.

The performance of the proposed algorithms is thoroughly evaluated through numerical simulations using DVB-S2X waveforms under realistic satellite impairments, including Doppler shifts, power imbalance, and imperfect channel estimation. To validate practical feasibility, a real-time hardware test-bed based on National Instruments (NI) universal software radio peripheral (USRP) platforms and field programmable gate array (FPGA) accelerated processing is developed. Experimental results demonstrate close agreement with theoretical and simulation outcomes, confirming that the proposed UT-based diversity combining achieves stable signal-to-interference-plus-noise ratio (SINR) gains and robust operation even under symbol-time misalignment. Overall, this thesis advances the state of the art in cooperative satellite communications by demonstrating that practical transmit diversity can be achieved at the UT without stringent synchronization requirements at the gateway. The proposed techniques contribute to scalable, resilient, and hardware-validated solutions suitable for future non-terrestrial networks.

Preface

This Ph.D. thesis was conducted between August 2022 and May 2026 at the Interdisciplinary Centre for Security, Reliability, and Trust (SnT) at the University of Luxembourg. The research was supervised by Dr. Juan Carlos Merlano Duncan at SnT, research scientist level I in SIGCOM research group at SnT, University of Luxembourg. Additionally, the thesis was undertaken in partnership with Société Européenne des Satellites (SES) in Luxembourg, represented by Dr. Joel Grotz.

Support for the Thesis

This Ph.D. thesis has received support from the Luxembourg National Research Fund (FNR), through the CORE Project (ARMMONY): Ground-based distributed beamforming harmonization for the integration of satellite and Terrestrial networks, under Grant FNR16352790. The significant support provided by SIGCOM is also acknowledged with gratitude.

Acknowledgments

I would like to begin by expressing my appreciation to my supervisor Dr. Juan Carlos Merlano Duncan, for his support and guidance. I also want to thank my coworkers at SIGCOM Dr. Jorge L. Gonzalez Rios, Dr. Luis M. Garces Socarras, Dr. Raudel Cuiman Marquez, Dr. Liz Martinez Marrero, Dr. Vu Nguyen Ha, and Prof. Symeon Chatzinotas, whose vast knowledge helped improve this research in every aspect.

Carlos Luis Marcos Rojas

Luxembourg, 17 June. 2026

Contents

List of Figures

List of Tables

Abbreviations

3GPP	Third Generation Partnership Project
5G	Fifth Generation of Mobile Communications
5G NR	5G New Radio
6G	Six Generation of Mobile Communications
ADC	Analog to Digital Converter
APSK	Amplitude and Phase-Shift Keying
HPAs	High-Power Amplifiers
AWGN	Additive White Gaussian Noise
AGC	Automatic Gain Control
BER	Bit Error Rate
BCH	Bose-Chaudhuri-Hocquenghem
CRLB	Cramér-Rao Lower Bound
CSI	Channel State Information
CP-OFDM	Cyclic Prefix OFDM
DAC	Digital to Analog Converter
DFT-s OFDM	Discrete Fourier Transform-spread OFDM
DSP	Digital Signal Processing
DVB-S2X	Digital Video Broadcasting - Second Generation Satellite Extensions
DVB-RCS2	Second Generation Digital Video Broadcasting – Return Channel Satellite
DLL	Delay Locked Loop
FDOA	Frequency Difference Of Arrival
FEC	Forward Error Correction
FFT	Fast Fourier Transform
FPGA	Field Programmable Gate Array
GNSS	Global Navigation Satellite Systems

GPS	Global Positioning System
ISI	Inter-Symbol Interference
ICI	Inter-Carrier Interference
LabVIEW	Laboratory Virtual Instrument Engineering Workbench
LMS	Land Mobile Satellite
LEO	Low Earth Orbit
LoS	Line of Sight
LDPC	Low-Density Parity-Check
MEO	Medium Earth Orbit
MRC	Maximum Ratio Combining
MTO	Multiple Timing Offsets
NOMA	Non-Orthogonal Multiple Access
NTN	Non-terrestrial Network
NGSO	Non-geostationary Orbit
NI	National Instruments
OFDM	Orthogonal Frequency-Division Multiplexing
OTFS	Orthogonal Time Frequency Space
O-U	Ornstein-Uhlenbeck
PAPR	Peak-to-Average Power Ratio
PDSC	Physical Data Shared Channel
PUSC	Physical Uplink Shared Channel
QPSK	Quadrature Phase Shift Keying
RAAN	Right Ascension of the Ascending Node
RF	Radio Frequency
SFO	Sampling Frequency Offset
SDR	Software Defined Radio
SER	Symbol Error Rate
STK	Systems Tool Kit
SNR	Signal to Noise Ratio
SINR	Signal to Interference plus Noise Ratio
SRRC	Square Root Rise Cosine
STBC	Space Time Block Code

STTC	Space Time Trellis Coding
TDOA	Time Difference Of Arrival
TED	Time Error Detection
UT	User Terminal
USRP	Universal Software Radio Peripheral

Notations

	Bold lowercase and uppercase letters represent vectors and matrices, respectively.
$(\cdot)^*$	Conjugate operator.
$(\cdot)^T$	Transpose operator.
$(\cdot)^H$	Conjugate transpose operator.
$\|\cdot\|_F^2$	The Frobenius norm squared of a matrix.
$\otimes$	The Kronecker product.
$\circledast$	Circular convolution.
$*$	Lineal convolution.
s_R	Real part of complex scalar.
s_I	Imaginary part of complex scalar.
$\mathbb{E}[\cdot]$	Expected value.
$\mathcal{N}(0, \sigma^2)$	Gaussian random variable with zero mean and variance σ^2.

Chapter 1

Introduction

This chapter introduces the concept of spatial diversity at the user terminal enabled by cooperative transmission in satellite communication systems, as a means of enhancing link resilience and ensuring robust connectivity in next-generation NTN. In particular, STBC is discussed as an attractive solution due to its low decoding complexity and favorable spectral efficiency. The chapter then examines the impact of symbol-time misalignment on the received STBC signal structure, highlighting the inherent limitations of conventional synchronous combining techniques and the practical constraints of current satellite technologies in tracking and compensating symbol-level timing offsets in distributed systems.

1.1 From Independent Satellites to Cooperative Networks

Satellite communication systems are undergoing a profound transformation driven by the large-scale deployment of non-geostationary satellite constellations. In contrast to traditional geostationary Earth orbit (GEO) systems, which rely on a small number of satellites operating at an altitude of approximately 35,786 km, modern constellations exploit LEO and medium Earth orbit (MEO) satellites to provide global coverage with reduced latency and increased spatial reuse. This paradigm shift is primarily motivated by the need for ubiquitous broadband connectivity, resilient communication infrastructures, and tight integration with terrestrial fifth- and sixth-generation (5G/6G) wireless networks [1–3].

While LEO satellites typically orbit at altitudes below 1500 km, resulting in round-trip latencies on the order of tens of milliseconds, which is comparable to or even lower than those of long-haul terrestrial networks [1]. MEO constellations, operating at altitudes between

approximately 7,000 km and 25,000 km, offer an intermediate trade-off between latency, coverage footprint, constellation size, and have traditionally been employed for global navigation satellite systems (GNSS), such as the global positioning system (GPS) and Galileo [4]. Recent proposals envision the joint exploitation of LEO and MEO layers in a multi-tier architecture to combine low latency with improved coverage continuity and robustness [2].

The unprecedented scale of emerging constellations, often comprising hundreds to tens of thousands of satellites, introduces both opportunities and challenges. On the one hand, dense satellite deployments enable high capacity through aggressive frequency reuse, flexible beamforming, and dynamic user association. On the other hand, the large number of satellites and their rapid orbital motion result in highly time-varying network topologies, strong Doppler effects, and frequent handovers, which significantly complicate synchronization, resource management, and interference mitigation [5, 6].

Early satellite communication systems were primarily designed according to a "bent-pipe" architecture, in which each satellite operated independently and simply relayed signals between gateways and user terminals. In such systems, inter-satellite coordination was minimal, and all signal processing and resource allocation were performed at ground stations [4]. While this approach is still viable for certain applications, it fails to fully exploit the spatial diversity and macro-diversity inherently available in large LEO and MEO constellations.

The availability of multiple satellites simultaneously visible to a given user terminal opens the door to cooperative transmission techniques, in which several satellites jointly serve the same user or group of users. This concept is closely related to coordinated multi-point (CoMP) transmission in terrestrial cellular networks, where multiple base stations coordinate their transmissions to improve cell-edge performance and reduce inter-cell interference [7]. When applied to satellite systems, cooperative transmission can significantly enhance link reliability, increase spectral efficiency, and improve coverage probability, particularly in dense constellations [8, 9].

From an information-theoretic perspective, multi-satellite cooperation allows the downlink to be modeled as a distributed multi-input multi-output (MIMO) system, where spatially separated satellites act as a virtual antenna array [7]. Practical realizations of this concept include coherent joint transmission, non-coherent joint transmission, and coordinated scheduling or beamforming, each offering different performance-complexity trade-offs [8, 9].

1.1.1 Enabling Technologies for Cooperative Satellite Transmission

The realization of cooperative transmission in large LEO and MEO constellations relies on several key technological enablers. First, inter-satellite links (ISLs), implemented using radio-frequency or optical technologies, provide the backbone for exchanging synchronization information, channel state information (CSI), and user data among satellites [2]. Optical ISLs, in particular, offer high data rates and low latency, but impose stringent pointing, acquisition, and tracking requirements.

Second, accurate time, frequency, and phase synchronization among satellites is a fundamental prerequisite for coherent cooperation. Due to the high orbital velocities of LEO satellites, carrier Doppler shifts can reach several tens of kilohertz, and their temporal variation induces fast carrier-phase drift [5, 10]. In contrast, symbol-timing drift evolves on a slower time scale and is dominated by long-term clock offsets and Doppler rate variations. This separation of time scales has motivated architectures in which certain impairments are mitigated at the satellite side through pre-compensation, while residual errors are handled at the UT [6, 11].

Third, advances in regenerative satellite payloads enable on-board baseband processing, flexible beamforming, and adaptive resource allocation, which are essential for scalable cooperative operation [1]. Unlike transparent payloads, regenerative payloads allow satellites to perform modulation, coding, and synchronization tasks locally, thereby reducing latency and relieving the ground segment.

1.1.2 Spatial Diversity in Satellite Communication Systems

The rapid evolution of satellite communication systems toward distributed architectures and multi-satellite constellations is transforming the design paradigm for next-generation user terminals. Modern systems increasingly rely on cooperative clusters of satellites and multiple gateways to deliver high-throughput, low-latency connectivity across diverse regions [12]. Within this trend, transmit diversity has emerged as a key technique, leveraging spatial diversity to mitigate fading and improve link reliability [13]. Transmit-diversity schemes such as STBC, space-time trellis coding (STTC), and maximum ratio combining (MRC) have demonstrated notable gains in bit error rate (BER), and SINR under realistic propagation impairments [14–17].

In parallel, NGSO satellite constellations are rapidly expanding and are expected to en-

hance global connectivity [18]. Simultaneous multi-satellite signal use can significantly improve spectral efficiency and link robustness [19]. In this context, STBC stands out as a promising technique due to its signal-to-noise ratio (SNR) improvements up to 3 dB when combining equal-power signals [20,21]. Moreover, STBC provides symbol-level diversity with low computational cost and is agnostic to the transmitter's knowledge of UT CSI, making it suitable for dynamic NGSO environments [22–24].

A rigorous analytical characterization of STBC performance in satellite environments has been provided for land mobile satellite (LMS) channels governed by shadowed-Rician fading. In [25], orthogonal STBC transmission over independent and correlated LMS channels is studied in detail, with closed-form expressions derived for symbol error rate, diversity order, and ergodic capacity. The results demonstrate that Alamouti-based transmission can effectively exploit spatial diversity even under severe shadowing conditions and that channel correlation, while degrading capacity, does not reduce the achievable diversity order. The analysis explicitly highlights the suitability of STBC schemes for satellite systems as they do not rely on transmitter-side CSI, thereby addressing a critical practical limitation of satellite links.

Complementary to analytical studies, simulation-based investigations have examined the integration of Alamouti STBC with multicarrier transmission schemes. In [26], a 2×2 MIMO-OFDM system employing Alamouti coding is evaluated under flat-fading conditions using quadrature phase shift keying (QPSK) modulation and AWGN. The reported BER results confirm that STBC-based MIMO-OFDM architectures significantly outperform single-antenna and non-diversity systems, while additional analyses of channel coefficients in the real, imaginary, and magnitude domains illustrate the diversity gains enabled by Alamouti coding. These results further support the practicality of combining STBC with OFDM to combat fading effects in frequency-flat channels.

The applicability of STBC techniques to realistic satellite use cases has also been investigated from a system-level perspective. In [27], a coded STBC-OFDM architecture is proposed for ship-borne satellite communications to enable reliable high-speed data transmission in maritime environments. Alamouti coding is employed to counter rain attenuation and shadowing, while OFDM mitigates multipath effects caused by sea surface reflections and ship motion. Simulation results show substantial BER improvements as the number of transmit and receive antennas increases. Despite incorporating realistic propagation impair-

ments, the system model assumes perfect synchronization and accurate channel knowledge at the receiver, simplifying the decoding of the STBC signals.

Beyond point-to-point satellite links, several works have explored diversity combining in cooperative and hybrid satellite–terrestrial architectures. Cooperative relay-based satellite–terrestrial communication networks have been analyzed in [28], where spatial diversity and relaying protocols are shown to enhance reliability and outage performance. Although STBC is not the sole focus of this work, the analysis reinforces the importance of diversity mechanisms in satellite-assisted networks.

More recently, hybrid satellite–terrestrial relay networks employing STBC at the satellite node have been investigated in conjunction with advanced multiple-access techniques. In [29], Alamouti coding is applied at the satellite transmitter in a non-orthogonal multiple access (NOMA) framework, combined with amplify-and-forward terrestrial relaying and receive antenna selection at the users. Exact and asymptotic outage probability expressions are derived for shadowed-Rician satellite links and Nakagami-m terrestrial channels, showing that the achievable diversity order depends jointly on the STBC configuration, relay antenna count, and user ordering. The study further confirms that Alamouti coding effectively alleviates CSI requirements at the satellite, albeit under the assumption of ideal symbol alignment required for preserving code orthogonality.

Cooperative transmission using multiple satellites and terrestrial repeaters has also been explored in the context of physical layer security. In [30], cooperative STBC-based schemes are proposed for LEO satellite systems, where multiple satellites and repeaters jointly transmit Alamouti-coded signals to enhance secrecy performance. By exploiting spatial diversity, the proposed schemes significantly degrade the error performance of potential eavesdroppers while maintaining reliable communication with legitimate users. As with other cooperative STBC-based approaches, perfect synchronization among the cooperating transmitters and receivers is implicitly assumed to ensure correct STBC decoding.

Across the existing literature, STBC-based diversity combining is consistently shown to be an effective and practical technique for improving performance in satellite, satellite–terrestrial, and hybrid communication systems. Analytical and simulation-based results demonstrate robustness against fading severity, shadowing, and channel correlation, provided that the orthogonality conditions of the STBC are preserved. Nevertheless, a common underlying assumption across all reviewed contributions is the availability of perfect symbol-level

synchronization at the receiver. Whether in LMS channels, STBC-OFDM maritime systems, cooperative relay networks, NOMA-based hybrid architectures, or cooperative LEO satellite schemes, symbol time alignment is implicitly required to enable linear STBC decoding and achieve the predicted diversity gains.

1.1.3 Timing Synchronization in Cooperative Non-Terrestrial Networks

Despite its advantages, the practical implementation of transmit diversity in distributed satellite systems faces significant challenges. Chief among these is stringent time alignment: conventional systems assume synchronous waveform arrival, but distributed satellite signals inherently suffer from multiple timing offsets (MTOs) and time difference of arrival (TDOA) due to large geometric separations and variable propagation paths [31,32]. These impairments are further exacerbated by long delays, Doppler effects, and lack of centralized synchronization [33]. Even with inter-satellite synchronization loops, UT position uncertainty and dynamic propagation differences make perfect alignment at the receiver difficult [34–36].

Recent studies on relay-based cooperative systems and TDOA-based localization provide useful insights into synchronization algorithms and performance limits [37, 38]. In addition, [39] presents a Cramér–Rao lower bound (CRLB) formulation for the design of TDOA and frequency difference of arrival (FDOA) estimators in satellite signal-processing applications. Prior works have also studied timing-synchronization protocols for mitigating clock drift in wireless sensor networks [40, 41]. Moreover, [42] reports experimental results for a proportional–integral (PI)-based fine-synchronization algorithm capable of reducing clock deviations between nodes to below 15μs. However, these methods rely on the exchange of dedicated synchronization packets that must be demodulated and decoded before timing compensation can be performed.

On the other hand, existing synchronization techniques for non-terrestrial and GNSS-based systems primarily focus on absolute time recovery or single-link synchronization and therefore do not address the relative symbol-level alignment required for distributed multi-satellite cooperative transmission. Classical satellite and GNSS synchronization methods target carrier, frame, and symbol timing with respect to a global reference [43,44], while recent NGSO multi-satellite cooperation studies relax the assumption of perfect synchronization and instead rely on receiver-side interference mitigation or waveform robustness to residual timing offsets [45, 46]. Although these approaches enable partial cooperative gains, they

inherently limit coherent symbol-level combining under large and time-varying propagation-induced misalignment. In parallel, TDOA- and FDOA-based techniques using satellite signals have been widely studied in localization and time-transfer contexts [39, 47].

One research direction focuses on achieving extremely high absolute timing accuracy across communication network nodes using GNSS. In [48], a time synchronization framework combining BeiDou and GPS observations is proposed, achieving synchronization precision on the order of tens of picoseconds. The work analyzes clock bias, measurement noise, and error compensation mechanisms and demonstrates that GNSS-referenced timing can provide a highly stable and precise time base for communication networks. However, timing in this study is treated purely as a clock-level reference shared among nodes. Propagation delay differences, satellite motion, and waveform superposition effects are outside the scope of the analysis, and no mechanism is provided to align transmitted waveforms observed at a receiver.

Timing synchronization challenges specific to NTN are further investigated in [49], which focuses on uplink synchronization between user terminals and gateways. The authors analyze the accumulation of time drift due to satellite mobility and clock offsets and propose a drift-measurement-based compensation method to maintain uplink timing alignment over time. The contribution lies in modeling timing evolution and drift compensation at the link and protocol level. Nevertheless, synchronization is considered on a per-link basis, assuming a single active transmitter, and the work does not address multi-satellite transmission scenarios or waveform-level alignment among distributed transmitters.

Receiver-side timing estimation and tracking constitute another important class of solutions. In [50], a single-symbol iteration-based delay-locked loop (DLL) is proposed for 5G new radio (NR) positioning, enabling fast convergence and improved timing tracking accuracy using limited observation windows. Similarly, [51] studies near-optimal joint estimation of timing offset and carrier frequency offset in integrated LEO satellite and terrestrial 5G systems under high Doppler and fast channel variation. In both works, timing is estimated at the receiver to support synchronization, demodulation, or positioning. However, the estimated timing parameters are not fed back into the transmission process, and the frameworks do not consider how multiple simultaneously transmitting satellites could be temporally aligned at the waveform level.

The impact of LEO satellite motion on orthogonal frequency-division multiplexing (OFDM) timing is analyzed in depth in [52]. This work demonstrates that non-uniform Doppler shifts

in broadband LEO systems induce significant sampling frequency offset (SFO), leading to cumulative timing drift, phase rotation, inter-carrier interference (ICI), and inter-symbol interference (ISI). Closed-form expressions are derived to quantify these impairments, and an ephemeris-based compensation scheme is proposed, involving fast Fourier transform (FFT) window repositioning and frequency-domain phase compensation. Satellite trial experiments confirm substantial demodulation performance gains after compensation. Despite this detailed analysis of timing distortion and correction, the proposed approach operates on a single transmitter–receiver link and does not address timing coordination among multiple transmitting satellites.

Coordinated transmission from multiple LEO satellites is explicitly considered in [53], where a multi-satellite orthogonal time frequency space (OTFS) based transmission framework is proposed for 6G LEO systems. The study demonstrates that coordinated transmission can significantly enhance reliability and spectral efficiency when signals are jointly detected in the delay–Doppler domain. Timing is included in the system model, but coherent or sufficiently accurate alignment across satellites is implicitly assumed. The paper does not provide a concrete waveform-level time alignment mechanism, nor does it analyze the effect of residual inter-satellite timing misalignment on system performance.

Time estimation using OFDM satellite signals is further explored in [54], which proposes a bandwidth-efficient TDOA estimation framework using partial OFDM data. Performance bounds are derived, and data selection strategies are introduced to reduce signaling overhead. The extracted timing information serves as a measurement for differential positioning, rather than for transmission coordination. Consequently, timing estimation is measurement-oriented and is not coupled to waveform generation or alignment among transmitters.

Taken together, these works address timing from complementary perspectives: clock-level synchronization using GNSS references [48], uplink and link-level synchronization in NTN [49], receiver-side timing estimation and tracking [50,51], single-link OFDM timing distortion compensation [52], coordinated multi-satellite transmission assuming implicit alignment [53], and timing estimation for positioning [54]. However, none of these studies explicitly addresses waveform-level time alignment for distributed multi-satellite transmissions in NTN. In particular, timing estimates are not integrated with transmitter-side waveform control, and alignment among concurrently transmitting satellites is assumed rather than ensured. This observation identifies a clear research gap and motivates the development of explicit waveform

time alignment strategies for distributed multi-satellite NTN systems.

1.1.4 Diversity Combining at the UT vs CSI-aware Precoding and Distributed Beamforming

An alternative to diversity combining at the UT could be gateway-based precoding or distributed beamforming. However, this choice should be driven primarily by the availability and reliability of global CSI and synchronization. Precoding and distributed beamforming are preferable in architectures with tightly synchronized gateways, low CSI feedback latency, and stable propagation conditions, where accurate CSI enables effective inter-beam interference suppression and maximizes spectral efficiency. In contrast, UT-side diversity combining should be favored in multi-satellite or multi-gateway systems subject to differential delays, asynchronous transmissions, or rapidly varying channels, where maintaining accurate end-to-end CSI at the gateway is impractical or costly. UT combining is also advantageous when feeder-link signaling overhead, gateway cooperation complexity, or scalability constraints dominate the system design, as it relies on locally estimated CSI and post-processing at the receiver. Consequently, UT-based diversity combining is well suited for robust and scalable deployments under realistic satellite impairments, while precoding remains the preferred solution in highly controlled and synchronization-centric network configurations [55, 56].

1.2 Comparative Analysis of 5G NR and DVB-S2X Waveforms for Satellite Communications

The evolution of satellite communication systems has prompted a renewed interest in the comparative merits of standardized cellular waveforms, such as 5G NR, and legacy satellite-optimized waveforms, notably digital video broadcasting - second generation satellite extension (DVB-S2X). This comparison is particularly relevant in the context of NTN, where waveform robustness, spectral efficiency, and resilience to satellite-specific impairments play a critical role.

DVB-S2X has been specifically designed for satellite environments, with an emphasis on high spectral efficiency and robustness under nonlinear amplification. As highlighted in [57], DVB-S2X operates in licensed Ku/Ka bands and supports high data rates ranging from

several Mbps to Gbps, at the cost of high terminal complexity and energy consumption. Its single-carrier waveform with carefully optimized amplitude and phase-shift keying (APSK) constellations and shaping roll-offs enables efficient operation close to the saturation point of high-power amplifiers (HPAs), which is a defining constraint of satellite downlinks. These design choices make DVB-S2X particularly well-suited for broadband and high-throughput satellite services.

In contrast, 5G NR has been extended to NTN contexts through the third generation partnership project (3GPP) standardization, primarily motivated by ecosystem integration rather than satellite-specific optimization. While 5G NR offers flexible numerology, scalable bandwidth allocation, and seamless integration with terrestrial networks, its default downlink waveform, cyclic prefix (CP)-OFDM, exhibits a high peak-to-average power ratio (PAPR). The detailed physical-layer comparison in [58] demonstrates that under nonlinear satellite HPAs, CP-OFDM suffers from increased out-of-band emissions, degraded modulation quality, and higher block error rates when compared to DVB-S2X single-carrier transmissions. Although 5G NR supports discrete Fourier transform-spread (DFT-s) OFDM as a lower-PAPR alternative, this option is not natively specified for downlink operation in all releases, limiting its applicability to satellite scenarios.

A comprehensive simulative comparison over a geostationary Ka-band satellite system is provided in [59]. The results show that, on the forward link, DVB-S2X consistently outperforms 5G NR physical data shared channel (PDSCH) in terms of spectral efficiency, with an average performance loss for NR ranging from approximately 15% to 26% depending on the target error rate and receiver assumptions. These losses are attributed to several factors intrinsic to the 5G NR waveform, including cyclic prefix overhead, reference signal density, and higher sensitivity to implementation losses and phase noise. Conversely, DVB-S2X benefits from highly optimized framing, pilot structures, and concatenated Bose-Chaudhuri-Hocquenghem (BCH) and Low-Density Parity-Check (LDPC) coding schemes that yield steeper error-rate performance curves under satellite channel conditions.

Despite these disadvantages, 5G NR exhibits notable strengths on the return link. As reported in [59], NR physical uplink shared channel (PUSCH) achieves performance comparable to, and in some scenarios slightly better than, second generation digital video broadcasting – return channel satellite (DVB-RCS2), particularly when considering spectral occupancy and flexible resource allocation. This indicates that 5G NR waveforms can be competitive in

uplink or burst-based satellite links, where nonlinear amplification constraints are less severe, and flexibility becomes a dominant requirement.

Overall, the comparison across the three studies indicates that DVB-S2X remains the more efficient and robust choice for satellite forward links, especially in high-throughput and power-limited regimes. In contrast, 5G NR offers architectural flexibility, integration benefits, and competitive performance in return links and IoT-oriented scenarios.

1.3 FPGAs and Software-Defined Radios in Satellite Communication Prototyping

In recent years, the evolution of satellite systems toward higher throughput, flexible payloads, and multi-orbit architectures has significantly increased system complexity, particularly at the physical layer and payload processing stages. These developments impose stringent requirements on waveform design, synchronization robustness, and error-control coding efficiency under severe propagation impairments and hardware constraints [60].

While analytical modeling and simulation remain indispensable tools in the early stages of satellite system design, they are insufficient to fully capture real-time processing constraints, implementation losses, and interactions between signal processing blocks. As a consequence, hardware-based prototyping has become an essential step for validating satellite communication techniques under realistic operating conditions before deployment. Such prototyping enables the direct evaluation of latency, throughput, numerical precision, and robustness against non-ideal effects that are difficult to assess accurately through simulation alone [60].

FPGAs play a central role in this context due to their ability to deliver high-throughput, low-latency digital signal processing with deterministic timing characteristics. Modern satellite waveforms rely heavily on computationally intensive baseband functions, including framing, synchronization, and advanced forward error correction, which are well suited to parallel FPGA architectures. In particular, the adoption of LDPC codes in contemporary satellite standards has reinforced the need for efficient FPGA-based implementations capable of real-time operation at very high data rates [61].

DVB-S2X standard represents a prominent example of this trend, introducing enhanced coding and modulation schemes to improve spectral efficiency across a wide range of operating conditions [62]. The validation of such standards requires hardware platforms capable of sup-

porting multiple configurations, adaptive schemes, and realistic channel impairments, making reconfigurable FPGA-based prototyping indispensable [62]. As demonstrated in recent implementations, FPGA-based platforms enable the practical evaluation of DVB-S2X receivers and decoders, providing insight into performance–complexity trade-offs beyond theoretical analysis [61].

Complementary to reconfigurable digital hardware, software-defined radio (SDR) platforms provide a flexible framework in which radio functionalities can be reconfigured through software while preserving real-time processing capabilities. By separating programmable baseband processing from broadband radio-frequency front ends, SDR architectures support rapid experimentation and end-to-end prototyping of satellite transmitter and receiver chains. This approach facilitates controlled laboratory testing of satellite links, enabling the systematic study of impairments such as quantization effects, carrier frequency offsets, and timing errors [60].

The combined use of FPGA-based processing and SDR platforms establishes an effective hardware–software co-design methodology for satellite communication research. In this paradigm, time-critical and computationally demanding functions are implemented in reconfigurable logic, while higher-level control and reconfiguration are handled in software, offering both performance and flexibility. Such an approach has become increasingly relevant for the prototyping and validation of modern satellite waveforms and payload architectures compliant with current and emerging standards [62].

Within this thesis, FPGA- and SDR-based prototyping platforms are employed to experimentally validate the proposed satellite communication techniques under realistic conditions. This methodology enables direct hardware verification of theoretical designs and provides practical insights into implementation complexity, performance limits, and robustness that cannot be obtained through simulation alone. The adopted framework therefore, reflects contemporary best practices in satellite communication research and supports the development of reproducible, hardware-validated results.

1.4 Challenges and Research Directions

Despite its potential, cooperative transmission in large LEO and MEO constellations faces several open challenges. The time-varying nature of the satellite topology complicates the

maintenance of consistent cooperation clusters and requires frequent updates of synchronization and coordination parameters [2]. Moreover, sharing accurate channel state information among satellites incurs signaling overhead and may be constrained by limited ISL capacity.

Scalability is another key concern. As the number of satellites increases, fully centralized coordination becomes impractical, motivating distributed and hierarchical cooperation strategies [8]. Furthermore, the stringent synchronization requirements for coherent joint transmission may be difficult to meet under realistic hardware and propagation impairments, making non-coherent or partially coherent schemes attractive alternatives [63].

1.5 Research Motivation

Spatial diversity has long been recognized as a powerful mechanism for improving link reliability by exploiting multiple independent transmission paths. Among spatial diversity techniques, STBC represents a particularly attractive solution due to its ability to provide transmit diversity without requiring channel state information at the transmitter and with low receiver complexity [20]. The simplicity and robustness of STBC make it well-suited for satellite systems, where feedback delays, terminal complexity constraints, and dynamic link conditions limit the applicability of more sophisticated multi-antenna transmission schemes.

However, the effectiveness of STBC critically relies on a set of implicit assumptions, most notably symbol-level time alignment among the transmitted signals. Classical STBC designs, including orthogonal schemes such as the Alamouti code, assume that signals transmitted from different antennas arrive at the receiver with perfect symbol synchronization [20]. Under this assumption, the orthogonality of the space–time code is preserved, enabling simple linear decoding and full diversity gain.

In practical satellite communication systems, achieving perfect symbol-time alignment is significantly more challenging than in terrestrial networks. Satellite links are characterized by long propagation delays, large distance variations, and relative motion between satellites and ground terminals, particularly in LEO constellations [60, 64]. When multiple transmit antennas, beams, or satellites are involved, even small differences in path length or timing reference can introduce symbol time misalignment at the receiver. Such misalignment can arise from satellite motion, imperfect synchronization between payload components, or distributed transmission architectures inherent to modern NTN deployments.

Symbol-time misalignment has profound consequences for STBC performance. Timing offsets distort the intended space–time structure of the transmitted signals, breaking the orthogonality conditions that underpin classical STBC decoding. As a result, ISI is introduced, and the receiver is no longer able to separate the transmitted symbols using simple linear processing [17, 56]. This leads to increased detection complexity, degradation of diversity gains, and potentially severe error-rate performance loss, undermining the primary advantages of STBC.

The impact of timing misalignment is particularly critical in satellite systems where synchronization resources are limited and delays are inherently large. In scenarios involving multi-satellite visibility, cooperative transmission, or distributed antenna architectures, maintaining tight symbol-level synchronization may be infeasible or prohibitively complex [34]. Consequently, the traditional assumption of perfectly synchronous STBC transmission becomes questionable in many realistic satellite use cases, especially in emerging LEO and NTN environments.

Despite these challenges, the potential benefits of STBC in satellite communications remain compelling. STBC offers a power-efficient and low-complexity diversity mechanism that aligns well with the design constraints of satellite terminals and payloads. This creates a strong motivation to revisit STBC from a satellite-specific perspective, explicitly accounting for symbol-time misalignment and its effects on code orthogonality, receiver design, and overall system performance.

Ultimately, understanding the interplay between STBC and symbol-time misalignment is essential for the design of robust spatial diversity techniques suitable for modern satellite systems. Addressing this challenge contributes directly to the broader goal of enabling reliable, scalable, and resilient non-terrestrial networks capable of supporting future global connectivity demands [60, 64].

This doctoral research proposes a UT-assisted synchronization and tracking strategy capable of compensating for large symbol time misalignment and following the remaining one [31]. While complementary work introduced a diversity combining scheme enabling STBC under timing misalignment using block-based ISI compensation, its matrix inversion burden limits its real-time applicability [17]. Moreover, in [56] this idea is extended through a dual-chain UT architecture supporting simultaneous synchronization with two satellites and combining of STBC-encoded symbols under imperfect alignment. The associated low-complexity

receiver leverages block-circulant properties and eigen-block decomposition to reduce computation [65–67].

1.6 Research Questions

Building on the research motivation outlined in this work, which focuses on spatial diversity at the user terminal in cooperative satellite communication systems, several key challenges are identified. This thesis addresses these challenges by investigating a set of research questions aimed at developing novel models, algorithms, and hardware demonstrators that enable the efficient combination of satellite signals from geographically distributed sources at the user terminal.

Question 1: Is it feasible to implement combining techniques for the reception of signals from satellite constellations with path diversity at the User Terminal under realistic conditions?

In this context, this thesis investigates dual-satellite connectivity to a UT employing STBC signals transmitted over statistically independent channels with heterogeneous CSI and propagation delays. A novel STBC combining method is proposed that accounts not only for the phase and amplitude of the received signals, but also for symbol-level time misalignment between them. This approach provides a robust combining solution that prevents SINR degradation when the signals are not perfectly time-aligned. The proposed method is validated through both simulations and real-time hardware experimental evaluations using the DVB-S2X waveform standard

Question 2: Is it feasible to implement combining techniques for the reception of signals from satellite constellations with path diversity under a reasonable complexity at the UT?

To address this question, a computationally efficient combining algorithm is designed and implemented using a hybrid software–hardware architecture. The algorithm exploits the properties of block-circulant matrices together with the proven efficiency of the FFT to significantly reduce the computational burden of the proposed solution. A detailed computational complexity analysis is conducted for both software and FPGA-based implementations, complemented by an evaluation of the FPGA resources utilized in the UT design.

Question 3: What will be the quantified effects, in terms of the signal degradation, of the imperfect CSI at the UT for the diversity combining techniques? Are the signal degradation levels (combined signal SINR) reasonable, such that these techniques can be envisioned for practical implementations?

In this context, the thesis analyzes the impact of symbol time misalignment on the SINR of STBC combined signals by comparing the classical Alamouti scheme with the SINR performance of the proposed solution. In addition, the effects of other relevant impairments, such as Doppler shift, power imbalance, and imperfect parameter estimation, are systematically investigated.

Question 4: What is the most suitable technique to estimate and track the fast-dynamic variations of the channel conditions for the signals traveling from the satellites to the UT?

In this area, the thesis proposes a novel sample time misalignment estimation method to track differential variations in symbol timing between the received signals. In addition, a new modeling framework is developed to evaluate the TDOA between signals, accounting for realistic satellite orbit perturbations, propagation delays, and mismatches arising from imperfections in the locally generated clock signals.

Question 5: What are the benefits of the diversity combining techniques at the UT (CSI-agnostic-at-Gateway) compared to the fully CSI-aware Precoding and distributed beamforming approaches?

In this aspect, the thesis explores how diversity combining techniques implemented at the UT can provide key advantages over fully CSI-aware precoding and distributed beamforming approaches by shifting the reliance on accurate and timely CSI away from the gateway. This is achieved by providing experimental results that support the hypothesis that UT-based diversity combining offers a scalable and resilient alternative that preserves SINR gains under realistic satellite impairments, while maintaining compatibility with existing waveforms such as DVB-S2X and enabling efficient real-time hardware implementation.

1.7 Research Methodologies

The research methodology adopted in this thesis is structured as follows. The study begins with a comprehensive review of the state of the art in relevant research areas, with the aim of identifying existing limitations and research gaps. Based on this review, a channel and UT model is developed to provide a formal framework for addressing the identified gaps. On this basis, novel research problems are formulated and subsequently addressed through detailed analytical investigations and experimental validation. The performance of the proposed solutions is then evaluated and benchmarked against existing methods, leading to the final conclusions of the research.

Summary of Research Methodology Strategy:

- **Algorithm**: This research explores various algorithms, including statistical digital signal processing algorithms, synchronization, and numerical linear algebra.
- **Modeling**: The UT base model was developed by adopting standardized designs specified in the ETSI DVB-S2X standard. The channel model, in turn, was derived from established models reported in peer-reviewed, top-tier IEEE journals, ensuring consistency with the principles of a realistic and practically relevant communication framework.
- **Simulation**: Simulations were conducted using sophisticated and robust tools such as STK, MATLAB, LabView NXG and Vivado Design Suit.
- **Hardware Validation**: The STBC combining algorithm was implemented and experimentally validated through a dedicated hardware demonstration platform. The setup comprised a gateway (GW) responsible for the generation of dual DVB-S2X signals, a channel emulator to introduce controlled impairments, and a user terminal performing signal reception, synchronization, and diversity combining.
- **Research Validation**: The proposed problems and solutions were subjected to rigorous scrutiny through submissions to and acceptances by top-tier IEEE conferences and journals, which served as a validation chamber for the research.

1.8 Contributions and Related Publications

This section outlines the primary contributions of the thesis. Furthermore, the research has led to the publication or submission of several papers in peer-reviewed journals and conference proceedings. These publications are categorized as follows: **J representing journals, and C for conferences**.

Chapter 1

This chapter provides an overview of cooperative satellites transmission and spatial diversity, including various use cases. The motivation for the thesis is also presented, along with the research methodology.

Chapter 2

This chapter introduces a model for the waveform time misalignment at the UT based on an imperfect orbital model for the satellites and clock mismatch, as well as a novel time misalignment estimation and satellite pre-compensation mechanism based on a distributed control loop between UT and the spacecraft. The model is validated via MATLAB simulations under dynamic channel conditions like variable propagation delay, inter-satellite clock skew, and phase noise.

Related publication:

[J] **C. L. M. Rojas**, L. M. Garces Socarras, V. Singh, R. Cuiman Marquez, J. C. Merlano Duncan, V. N. Ha, R. Palisetty, S. Chatzinotas, and B. Ottersten, "A novel waveform time alignment strategy for distributed multi-satellite transmissions in non-terrestrial networks," IEEE Transactions on Aerospace and Electronic Systems, pp. 1–12, 2026 (Under review)

[C] **C. L. M. Rojas**, R. Palisetty, J. Krivochiza, J. L. G. Rios, L. M. Marrero, W. A. Martins, J. C. M. Duncan, and S. Chatzinotas, et al., "Time-Misalignment Estimation in Overlapped DVB-S2X Waveforms," 2024 IEEE Wireless Communications and Networking Conference (WCNC), Dubai, United Arab Emirates, 2024, pp. 1-6, doi: 10.1109/WCNC57260.2024.10570646.

[C] S. Daoud, E. Lagunas, J. L. González-Rios, **C. L. M. Rojas** and S. Chatzinotas, "Differential Delay Effect in Precoded Cooperative Multi-Gateway Satellite Systems," 2025 IEEE 36th International Symposium on Personal, Indoor and Mobile Radio Communications (PIMRC), Istanbul, Turkiye, 2025, pp. 1-7, doi: 10.1109/PIMRC62392.2025.11274691.

Chapter 3

This chapter introduces a dual synchronization-chain UT architecture and a low-complexity receiver capable of combining STBC-encoded signals in the presence of imperfect symbol-time misalignment. An analytical derivation of the proposed STBC combining scheme is presented, along with a numerical implementation approach. The performance of the system is validated via MATLAB simulation that included channel impairments like additive white Gaussian noise (AWGN), symbol time misalignment, Doppler shift, and power imbalance.

Related publication:

[J] **C. L. Marcos Rojas**, J. L. Gonzalez Rios, L. M. Garces Socarras, V. Singh, R. Cuiman Marquez, J. C. Merlano Duncan, V. Nguyen Ha, S. Chatzinotas, and B. Ottersten et al., "Dual Satellite STBC Combining Under Imperfect Symbol Time Alignment," in IEEE Open Journal of the Communications Society, vol. 7, pp. 301-314, 2026, doi: 10.1109/OJCOMS.2025.3648041.

[J] V. Singh, W. A. Martins, R. Palisetty, **C. L. M. Rojas**, J. L. Gonzalez Rios, J. A. V´asquez-Peralvo, J. Krivochiza, J. C. Merlano-Duncan, L. G. Socarras, S. Chatzinotas, and B. Ottersten, et al., "Diversity Combining Scheme for Time-Varying STBC NGSO Multi-Satellite Systems," in IEEE Communications Letters, vol. 28, no. 4, pp. 882-886, April 2024, doi: 10.1109/LCOMM.2024.3359329.

Chapter 4

This chapter describes the hardware testbed developed using National Instruments USRPs and the real-time experiments performed to validate the system. Specific details about the structure of the gateway, the channel emulator, and the dual synchronization-chain UT are provided, as well as a computational complexity analysis and a comparison between the results obtained in the hardware experiments performed in the chapter and the simulation results from the previous one.

Chapter 5

The final chapter presents the main conclusions of the thesis and outlines potential directions for future research.

Chapter 2

Time Misalignment Estimation and Compensation

2.1 Introduction

This chapter introduces a novel waveform time-alignment strategy tailored for NGSO multi-satellite transmissions. First, a system-level analysis is presented to characterize the combined effects of differential propagation delay and relative clock drift among satellites. Based on these insights, a two-stage misalignment estimation method is proposed that leverages coarse frame detection and fine symbol-time tracking using DLL- and Kalman-filter-based architectures. Building on this estimate, a hybrid compensation mechanism is developed that combines discrete sample shifting and continuous fractional resampling to align waveforms on the transmitter side. Numerical evaluations using the DVB-S2X waveform standard and realistic orbital and oscillator models demonstrate that the proposed approach effectively mitigates timing discrepancies under real-world channel impairments, such as satellite motion and uplink feedback delays, thereby enabling the practical implementation of transmit-diversity techniques.

2.2 System Description

Consider the scenario illustrated in Fig. 2.1, where a UT receives P signals from multiple NGSO satellites in different planes or shells of the same constellation, providing cooperative transmission to enhance link resilience. In this case, two main cases can be considered. In the

first one, each satellite transmits on a distinct frequency, and the UT combines the signals using MRC or a similar approach, with buffer memories employed to mitigate the effect of timing misalignment. However, since the same data is transmitted over P different frequencies, the overall spectral efficiency is reduced by a factor of $\frac{1}{P}$. In the second case, all satellites reuse the same frequency, and the UT performs signal combining using STBC. In both cases, compensating for time misalignment between received signals before demodulation is critical. In the first case, large symbol time misalignment requires long memory buffers to store early-arriving symbols until the latest symbols are available for combination. In the second one, where frequency reuse and STBC are employed, even slight symbol-time misalignment among encoded signals can significantly degrade STBC performance [56], necessitating stricter time synchronization.

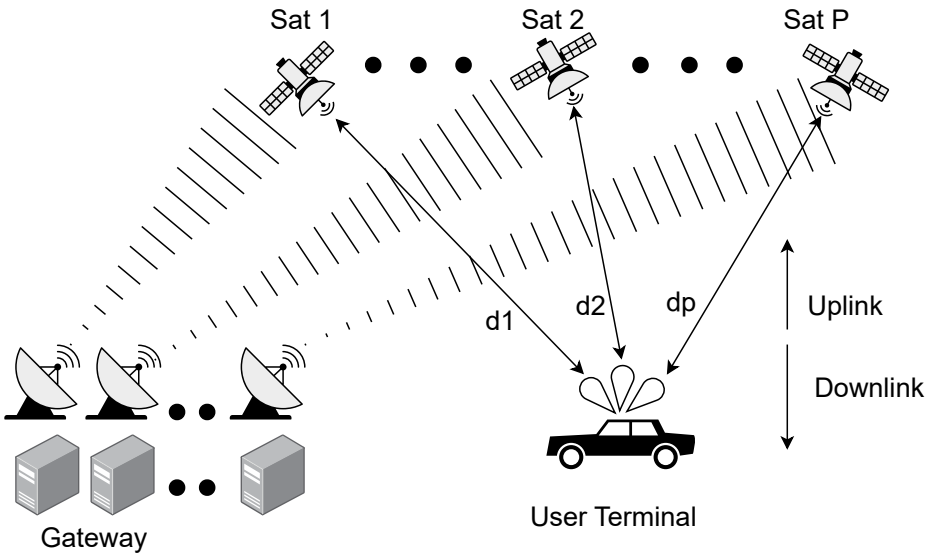

Figure 2.1: UT capable of seeing multiple NGSO satellites, where the signal from each satellite arrives with different propagation delays.

In the proposed system, the differential sample-time misalignment among the received signals is estimated at the UT. This misalignment information is then fed back to the satellites through an uplink connection, where the regenerative payloads apply sample-time pre-compensation to the transmitted signals. This design choice is motivated by the markedly different dynamics of symbol-time and carrier-phase impairments in satellite links.

In satellite communication systems, carrier-phase drift evolves on a significantly faster time scale than symbol-time drift, since phase errors amplify clock and Doppler impairments

by the carrier frequency. In contrast, symbol-time drift accumulates slowly over many symbol intervals and mainly reflects long-term clock offset and Doppler-rate variations [44, 68, 69]. Accordingly, the proposed system focuses on achieving coherent symbol-time transmission via satellite-side sample-time pre-compensation, while residual time misalignment is handled at the UT, depending on the selected transmission scenario.

Although the system was designed specifically for a pulse-shape waveform standard that supports data-aided synchronization and employs digital resamplers as part of the symbol time synchronization mechanism, such as DVB-S2X, a similar approach could be tailored for 5G NR.

Two receiver architectures can be considered. The first architecture (Fig. 2.2) corresponds to the scenario where each satellite operates on a distinct frequency. In this case, a separate radio frequency (RF) front-end and analog-to-digital converter (ADC) is required for each down-converted signal. The second architecture (Fig. 2.3) applies to the frequency reuse scenario, where all signals share the same spectrum, allowing the use of a single ADC. Nevertheless, in both cases, a separate synchronization chain is needed for each of the signals.

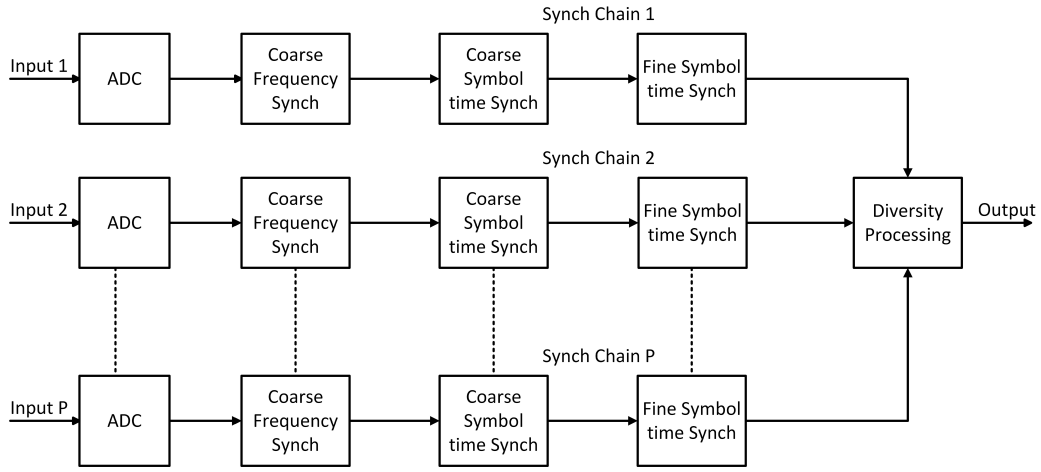

Figure 2.2: UT time synchronization architecture for receiving signals from multiple RF frequencies.

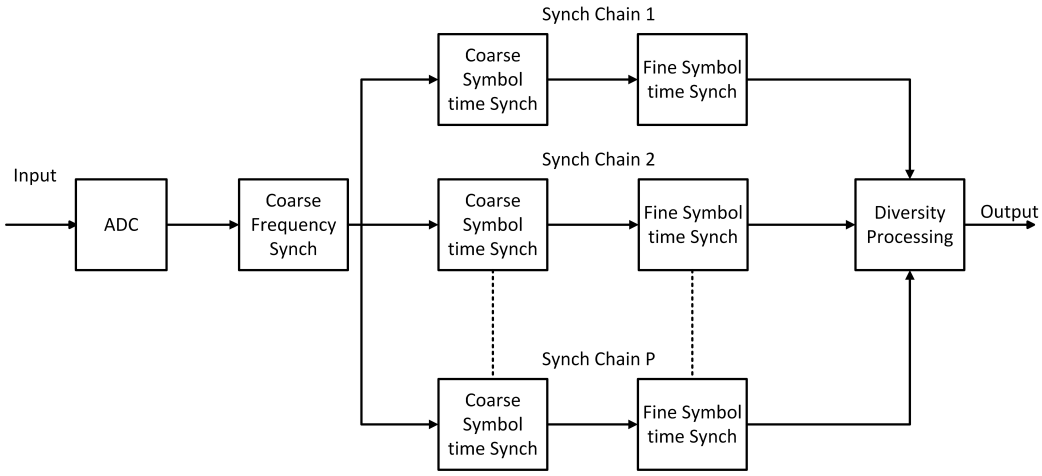

Figure 2.3: UT time synchronization architecture for receiving signals from a single RF frequency.

2.2.1 Orbital Model

To accurately evaluate the performance of the proposed time-alignment strategy under realistic NTN conditions, a highly precise multi-satellite orbital model was developed. The continuous variation of the TDOA and the resulting MTOs among cooperating transmitters are intrinsically linked to the time-varying distances between the UT and the spacecrafts. Consequently, a deterministic geometric model must be established before incorporating stochastic impairments.

The baseline topology was generated utilizing systems tool kit (STK) by Ansys [70]. The scenario mimics modern LEO mega-constellations, operating at an altitude of $H = 480$ Km with an orbital inclination of 53°. A Walker-Delta constellation topology was employed to guarantee deterministic, continuous overlapping coverage over the UT, a fundamental prerequisite for distributed transmit diversity schemes such as MRC or STBC. This spatial diversity was achieved by meticulously phasing the right ascension of the ascending node (RAAN) for adjacent orbital planes and adjusting the true anomaly for intra-plane satellites, ensuring that multiple nodes are simultaneously within the UT's field of view.

The geometric link availability in STK is strictly governed by a minimum elevation angle mask of $\sigma = 25°$ at the UT, a practical constraint necessary to mitigate severe atmospheric attenuation and terrestrial blockage. Considering a spherical Earth model with radius $R_E \approx 6371$ Km, the maximum angular field of view (θ_{FOV}) from the satellite's perspective is derived

using the spherical Law of Sines:

$$\theta_{FOV} = \arcsin\left(\frac{R_E}{R_E + H}\cos(\sigma)\right). \tag{2.1}$$

For the defined parameters, $\theta_{FOV} \approx 57.4°$, which translates to a maximum slant range ($d_{\max}$) of approximately 994 Km and a ground footprint diameter of roughly 1700 Km. Given the ground track velocity of the LEO satellites ($\sim$ 7.1 Km/s), the maximum continuous line-of-sight (LoS) duration for a single satellite is strictly bounded to a window of approximately 4 minutes.

To transition from the ideal deterministic model provided by STK to a realistic channel simulation suitable for evaluating waveform alignment, the absolute J2000 Cartesian coordinates of the satellites and the UT were exported to MATLAB. In operational environments, LEO satellites experience continuous and independent orbital perturbations, primarily due to atmospheric drag variations caused by solar activity [71]. These micro-variations directly impact the differential propagation delay defined in (2.9).

To capture these non-deterministic effects, an Ornstein-Uhlenbeck (O-U) stochastic process was integrated into the kinematic model, a widely validated mathematical approach for characterizing atmospheric density uncertainties and drag variations in LEO [72, 73]. The atmospheric density ρ was interpolated using a smooth piecewise cubic hermite interpolating polynomial (PCHIP) based on the exact altitude, while the stochastic variation of the drag acceleration was modeled as a first-order Gauss-Markov process:

$$a_{err}(t) = a_{err}(t - \Delta t)e^{-\frac{\Delta t}{\tau}} + \sigma_{pct}\sqrt{1 - e^{-\frac{2\Delta t}{\tau}}} \cdot \mathcal{N}(0, 1). \tag{2.2}$$

where τ is the mean-reversion time constant and σ_{pct} is the volatility percentage. This stochastically integrated error is added to the nominal STK vectors to yield the true position vector $\vec{P}_{real}(t)$ for each individual satellite. The instantaneous slant range $D_p(t) = \|\vec{P}_{real}(t) - \vec{P}_{UT}(t)\|$ is then dynamically computed. This perturbed distance dictates the precise propagation delay fed into (2.7), providing a robust and physically accurate testbed to evaluate the proposed two-stage misalignment estimation and compensation mechanism.

2.2.2 Signal Model

In the case where the signals are transmitted in different frequencies and digitized by different ADCs at the UT, the pulse-shape individual signal coming from the P satellite can be expressed as

$$r_p(n) = e^{-j\theta(n)} \sum_k s(k) g(nT_s - kT_s - \tau(n)) + z(n), \tag{2.3}$$

where $s(k)$ denotes the transmitted symbol, T_s is the sampling period, $\theta(n)$ represents the time-varying phase rotation of the received signal, $g(\cdot)$ denotes the impulse response of the overall channel, encompassing the transmitter filter, the wireless channel, and the receiver filter, $\tau(n)$ denotes the symbol-timing error, and $z(n)$ represents the filtered Gaussian noise at the output of the receive filter.

On the other hand, for the scenario where the satellites in the FoV of the receiver employ frequency reuse and a single ADC is used at the UT, the overlapped digitized signals can be expressed as

$$r(n) = \sum_p e^{-j\theta_p(n)} \left(\sum_k s_p(k) g_p(nT_s - kT_s - \tau_p(n)) \right) + z(n). \tag{2.4}$$

The phase rotation of the p-th received signal can be modeled as $\theta_p(n) = \Delta\omega_p n + \varphi_p$, where φ_p denotes a constant phase offset and $\Delta\omega_p = 2\pi\Delta f_p T_s$ represents the carrier frequency offset (CFO) between the p-th received signal and the carrier generated by the UT local oscillator. The time variations in $\theta_p(n)$ and $\tau_p(n)$ arise primarily from two factors: (i) the Doppler shift induced by the relative motion between the satellite and the UT, and (ii) differential deviations from the ideal characteristics of the locally generated clock signals at the satellite and the UT, also known as clock mismatch.

2.2.3 Clock Model

Clock mismatch primarily originates from manufacturing tolerances and material imperfections in the quartz crystal employed for clock generation. In Low Earth Orbit (LEO) satellite constellations, radiation-tolerant temperature-compensated crystal oscillators (TCXOs) and oven-controlled crystal oscillators (OCXOs) are widely adopted, as they provide an effective trade-off between power consumption and frequency stability suitable for modern

small-satellite and large-constellation missions. TCXOs typically exhibit frequency accuracies in the range of ±0.5 to ±5 ppm, whereas OCXOs achieve significantly higher stability, with frequency errors on the order of 0.001–0.05 ppm [74, 75]. Accordingly [76], the onboard clock drift with respect to the nominal frequency can be modeled as:

$$C_{TX}^{(p)}(t) = \Omega t + \phi + v, \tag{2.5}$$

where Ω denotes the clock skew, defined as the difference between the actual and nominal clock frequencies, ϕ denotes the clock offset, i.e., the phase difference, and v represents a random noise term corresponding to phase noise.

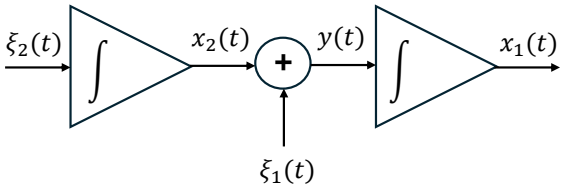

Figure 2.4: Two-state noise clock model.

In [77, 78], the authors describe a two-state noise clock model (Fig. 2.4) derived from the integration of two zero-mean white noise processes $\xi_1(t) \sim \mathcal{N}(0, \boldsymbol{q_1})$ and $\xi_2(t) \sim \mathcal{N}(0, \boldsymbol{q_2})$ with variances $\boldsymbol{q_1}$ and $\boldsymbol{q_2}$, respectively. Following the same approach, the relationship between the clocks in two distributed nodes (transmitter (TX) and receiver (RX)) can be expressed as:

$$C_{RX}(t) = \Omega_p{}' C_{TX}^{(p)}(t) + \phi_p^{'} + v_p^{'}, \tag{2.6}$$

where $\Omega_p{}'$, $\phi_p^{'}$, and $v_p^{'}$ denote the relative clock skew, clock offset, and differential phase-noise term between the TX and RX, respectively. Therefore, under perfect synchronization, $v_p^{'} = 0$, $\phi_p^{'} = 0$, and $\Omega_p{}' = 1$.

2.2.4 Signal Misalignment Characterization

As discussed, the propagation delay (the time it takes for the signal to arrive from TX to RX) is directly proportional to the distance and can be expressed as

$$T_{delay}^{(p)}(t) = \frac{D_p(t)}{c}, \tag{2.7}$$

where $D_p(t)$ is the instantaneous slant range for satellite p and $c = 3 \times 10^8$ m/s is the speed of light.

Using the previous definitions for the propagation delay and clock model, a closed-form expression for the delay of the digitized signal after the ADC can be formulated as

$$d_p(t) = (\Omega_p{}' - 1)t + \phi_p^{'} + v_p^{'} + \left.\frac{T_{delay}^{(p)}(t)}{T_s}\right|_{t=nT_s}. \tag{2.8}$$

From (2.8) an expression for the misalignment between the signals from satellite i and j can be easily derived as

$$\Delta T_s^{(ij)} = d_i(t) - d_j(t). \tag{2.9}$$

2.3 Time Misalignment Estimation Between Signals

One of the aims of this research is to address one of the most critical challenges in multi-satellite cooperative transmission systems: the misalignment of signals upon arrival at the UT. As opposed to computing the propagation time between the satellite and the UT like GNSS-based techniques [43], our focus is on estimating the misalignment, expressed in sample time (T_s), among the signals detected by the receiver. To do that, our approach proposes a combination of coarse and fine symbol time synchronization employing the elements of the architecture shown in Fig. 2.2 and Fig. 2.3. Assuming that the waveform standard employed by the P satellites has a structure as the one shown in Fig. 2.5. Herein, the beginning of the frame consists of L known symbols, which enable each synchronization chain to perform coarse time synchronization (i.e., frame synchronization). Additionally, distributed throughout the frame is a set of pilot fields of length M, which facilitate fine symbol-time synchronization by tracking the drift of $\tau_p(n)$.

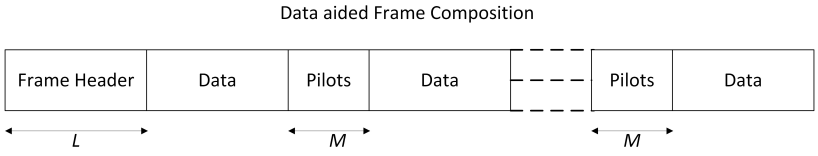

Figure 2.5: Frame structure for pulse-shape waveforms with data-aided synchronization.

In this sense, we can say that the total estimated misalignment between the i and j (where

$i, j \in p$) signals is composed of an integer sample time misalignment ($\Delta I^{(ij)}$) and a fractional sample time misalignment ($\Delta\mu^{(ij)}$), and can be expressed as:

$$\tilde{\Delta T_s}^{(ij)} = \tilde{\Delta I}^{(ij)} + \tilde{\Delta\mu}^{(ij)} \tag{2.10}$$

The integer sample time misalignment can be estimated by calculating the difference (in number of samples) between two distinct Frame Headers coming from different satellites. Suppose that each satellite visible to the UT transmits in the Frame Header field a sequence of symbols $a_p(n)$ of length L. Then, assuming that the total frame length is much longer than the time misalignment between the signals, the integer misalignment between the signals coming from satellite i and j can be calculated as

$$\tilde{\Delta I}^{(ij)} = l^{(i)} - l^{(j)} \tag{2.11}$$

where $l^{(p)}$ represents the sample at which the complete Frame Header from the signal p was detected and is calculated by correlating the known symbols $a_p(n)$ with the output of the receiver filter given by (2.3) and (2.4) as

$$l^{(p)} = \arg\max_{l} \left| \sum_{k=0}^{L-1} a_p(k) r^*(k-l) \right| \tag{2.12}$$

On the other hand, the fractional sample time misalignment is calculated as the difference between the filtered symbol time discrimination function from the synch chain i and j.

$$\tilde{\Delta\mu}^{(ij)} = \mu^{(i)}(n) - \mu^{(j)}(n) \tag{2.13}$$

where $\mu^{(p)}(n) \approx -\tau_p(n)$ is the estimated instant misalignment and traditionally obtained by passing the incoming signal through a DLL as in Fig. 2.6.

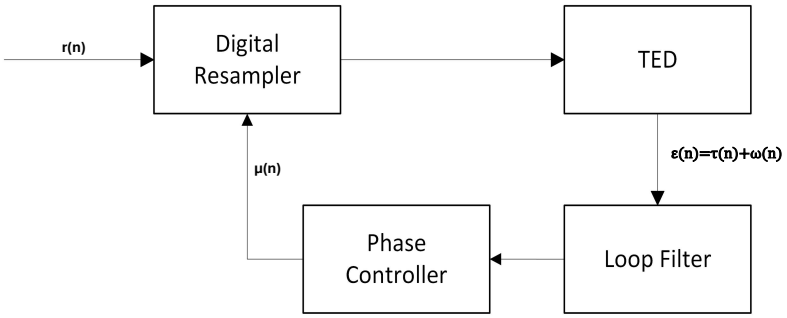

Figure 2.6: Traditional structure of an DLL.

Similar to traditional control loops, a DLL is composed of an actuator (the digital resampler) whose function is to advance or delay the incoming samples by a fractional value $\mu(n)$, a time error detection (TED) function ($\epsilon(n) = \tau(n) + w(n)$) composed by the misalignment $\tau(n)$ and random noise $w(n)$, a loop filter and a phase controller. For the case of a first-order DLL, the relationship between $\mu(n)$ and $\epsilon(n)$ through the loop filter and phase controller can be expressed in the z domain as

$$U(z) = \frac{k_1 z^{-1}}{1 - (1 - k_1)z^{-1}} E(z) \tag{2.14}$$

while in the case of a second-order DLL

$$U(z) = \frac{k_1 z^{-1} + (k_2 - k_1)z^{-2}}{1 - (2 - k_1)z^{-1} + (1 - k_1 + k_2)z^{-2}} E(z) \tag{2.15}$$

Here, k_1 and k_2 are the coefficients that control the loop bandwidth (B_n), and determine the tracking capabilities of the DLL. On the other hand, $E(z)$ is the z transform of the symbol time discrimination function $\epsilon(n)$ that is generated using the pilots' fields in the frame, and any of the data-aided symbol time synchronization methods presented in [79], like Mueller-Müller or Early-Late Gate. In our case, we employed a modified version of the Early-Late Gate discrimination function proposed in [31] and given by:

$$\epsilon(n) = \frac{|E(n)|^2 - |L(n)|^2}{|I(n)|^2}. \tag{2.16}$$

Herein, $I(n)$ denotes the correlation between the known pilot symbols and the received pilots,

while $E(n)$ and $L(n)$ represent the correlations of the known pilots with the samples immediately preceding and following the pilot positions in the frame, respectively. As illustrated in Fig. 2.7, the modified function exhibits a more linear behavior compared to the S-shaped response of the classical ELG formulation.

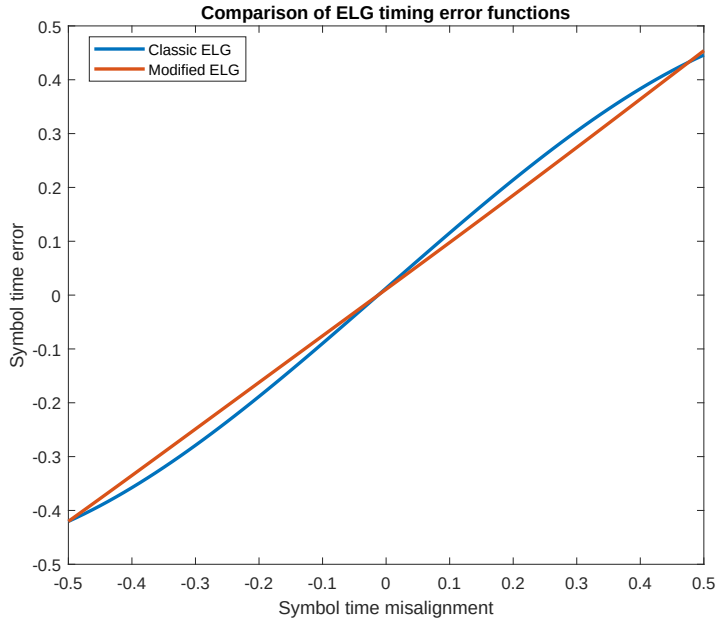

Figure 2.7: Comparison between the classic ELG timing error detection function and the modified version presented in [31].

One important aspect to consider when using orthogonal pilots for data-aided synchronization in overlapped signals is the effect of data scramblers. It is well known that orthogonal pilot symbols retain their orthogonality only when they remain perfectly time-aligned. However, in the scenarios considered in this work, the overlapped signals arrive at the UT with imperfect alignment. In such cases, what ensures that the TED function remains unbiased is the fact that the overlapped signal is scrambled by an independent scrambler, effectively transforming it into zero-mean random noise. This prevents systematic interference with the timing-error discriminator and allows the synchronization process to remain robust despite the misalignment.

A more modern approach to timing-tracking loops replaces the conventional loop filter and phase controller with a Kalman filter (Fig. 2.8). Unlike fixed-bandwidth loop filters, Kalman filters provide adaptive, state-space based tracking, enabling improved performance under dynamic conditions. In environments characterized by high Doppler rates, this adaptive

architecture has been shown to outperform traditional timing-tracking loops [80, 81].

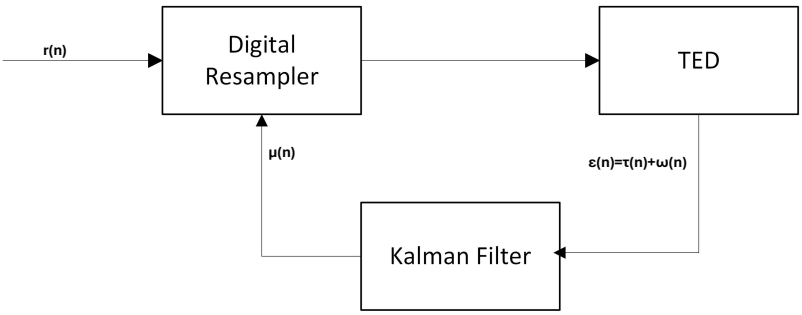

Figure 2.8: Modern DLL with Kalman filter.

To use a Kalman state-space model as an alternative to the classic loop filter and phase controller, first we need to define a state vector given by:

$$\mathbf{x}_k = \begin{bmatrix} \mu_k \\ \dot{\mu}_k \\ \ddot{\mu}_k \end{bmatrix} \tag{2.17}$$

where μ_k, $\dot{\mu}_k$, and $\ddot{\mu}_k$ represent the symbol time offset, the timing drift (first derivative), and the timing drift acceleration, respectively. Then, one can define the state evolution matrix $\mathbf{F}$, where T denotes the coherent integration interval, equivalent to the update interval of the classic loop filter, and the measurement matrix $\mathbf{H}$ as:

$$\mathbf{x}_{k+1} = \underbrace{\begin{bmatrix} 1 & T & \frac{1}{2}T^2 \\ 0 & 1 & T \\ 0 & 0 & 1 \end{bmatrix}}_{\mathbf{F}} \mathbf{x}_k + \mathbf{w}_k \tag{2.18}$$

$$z_k = \mathbf{H}\mathbf{x}_k + v_k, \qquad \mathbf{H} = \begin{bmatrix} 1 & 0 & 0 \end{bmatrix} \tag{2.19}$$

where $\mathbf{w}_k \sim \mathcal{N}(0, \mathbf{Q})$ and $v_k \sim \mathcal{N}(0, R)$ represent the process and observation noise covariance matrices and are given by $\mathbb{E}[\mathbf{w}_k \mathbf{w}_k^T]$ and $\mathbb{E}[\mathbf{v}_k \mathbf{v}_k^T]$ [80].

Once the state-space model has been defined, the Kalman filter estimation process can be divided into the following steps:

- Prediction

$$\hat{\mathbf{x}}_{k|k-1} = \mathbf{F}\hat{\mathbf{x}}_{k-1|k-1}, \tag{2.20}$$

$$\mathbf{P}_{k|k-1} = \mathbf{F}\mathbf{P}_{k-1|k-1}\mathbf{F}^T + \mathbf{Q}. \tag{2.21}$$

- Innovation

$$\mathbf{y}_k = z_k - \mathbf{H}\hat{\mathbf{x}}_{k|k-1}, \tag{2.22}$$

$$\mathbf{S}_k = \mathbf{H}\mathbf{P}_{k|k-1}\mathbf{H}^T + R. \tag{2.23}$$

- Kalman Gain

$$\mathbf{K}_k = \mathbf{P}_{k|k-1}\mathbf{H}^T\mathbf{S}_k^{-1}. \tag{2.24}$$

- Correction

$$\hat{\mathbf{x}}_{k|k} = \hat{\mathbf{x}}_{k|k-1} + \mathbf{K}_k\mathbf{y}_k, \tag{2.25}$$

$$\mathbf{P}_{k|k} = (\mathbf{I} - \mathbf{K}_k\mathbf{H})\mathbf{P}_{k|k-1}. \tag{2.26}$$

In our case, since we are using a TED function given by (2.16), then (2.22) is modified as $\mathbf{y}_k = \epsilon(n)$.

2.4 Time Misalignment Compensation

By equipping the spacecraft regenerative payload with additional memory resources, the system can partially compensate for signal misalignment by advancing or delaying the waveform through a memory buffer. However, implementing such a buffer requires a structure more sophisticated than a simple shift register that provides only discrete delays. Relying solely on discrete sample shifts would distort the waveform and interfere with the timing-synchronization loop at the UT. To address this limitation, we introduce an approach that combines discrete and continuous time-delay mechanisms, as illustrated in Fig. 2.9. Nevertheless, a single large initial discrete shift can reduce waveform misalignment from

thousands of samples to just a few, and thereafter, a smoother sample shift should be applied using the proposed architecture.

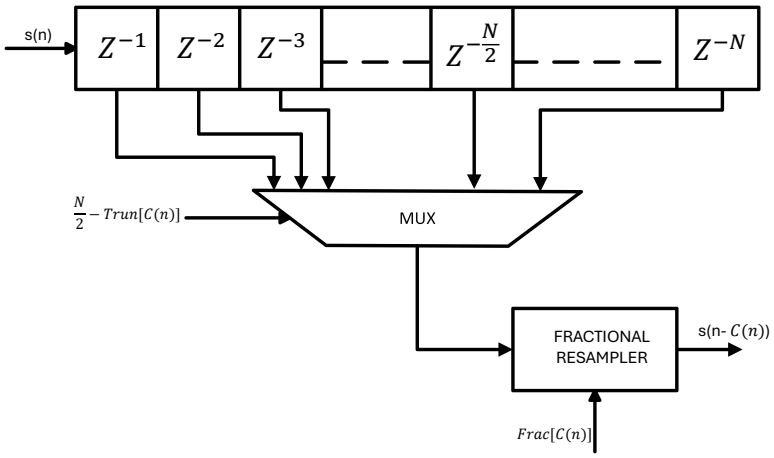

Figure 2.9: Time compensation scheme based on discrete and continuous shifts.

At the spacecraft side, the output signal enters the compensation mechanism located in the satellite payload chain as in Fig. 2.10. Such a mechanism is composed of a buffer of size N, a multiplexer, and a fractional resampler. The multiplexer selects the integer number of samples by which the signal will be advanced or delayed. This integer value is obtained from the expression $\frac{N}{2} - Trun[C(n)]$ where $C(n) \in \mathbb{R}$ denotes the compensation value. When $C(n) = 0$, the signal is delayed by a fixed initial value of $\frac{N}{2}$, which allows advancing the signal samples in case it is necessary. The integer part of $C(n)$ must also satisfy the bound $|Trun[C(n)]| < \frac{N}{2}$. After applying the integer delay, the fractional resampler is used to advance or delay the signal by the fractional component of the compensation value $Frac[C(n)]$, the structure of this resampler was presented in [31]. The compensation value would be updated in small (semicontinuous) steps such that $C(n) \approx -\Delta\tilde{T}_s^{(ij)}$. The combination of integer and fractional delay can be incorporated into the spacecraft payload with minimal additional computational complexity, requiring little more than a shift register of N locations and a five-tap FIR filter for the fractional resampler, along with minor supporting components such as the multiplexer and the loop controller.

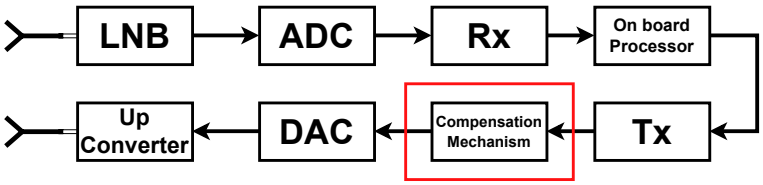

Figure 2.10: Sample time compensation mechanism position in satellite payload chain.

Using the time-misalignment estimate reported by the UT as the error signal, a distributed control loop can be employed to update the value of $C(n)$. This loop uses a second-order loop filter similar to (2.15), but incorporates an additional delay d in the error term to account for the propagation time of the uplink signal from the UT to the satellite. Consequently, the overall system function of the distributed control loop can be expressed as

$$C(z) = \frac{k_1 z^{-1} + (k_2 - k_1) z^{-2}}{1 - (2 - k_1) z^{-1} + (1 - k_1 + k_2) z^{-2}} \tilde{\Delta T_s}^{(ij)}(z) z^{-d}. \tag{2.27}$$

2.5 Numerical Results

To validate the proposed system, we generated the orbital motion of two satellites using the orbital model presented in Section 2.2.1, as illustrated in Fig. 2.11. The atmospheric effects described in the same section introduce a cumulative orbital deviation, reflected in the evolution of the orbital error (deviation from the perfect orbit) shown in Fig. 2.12.

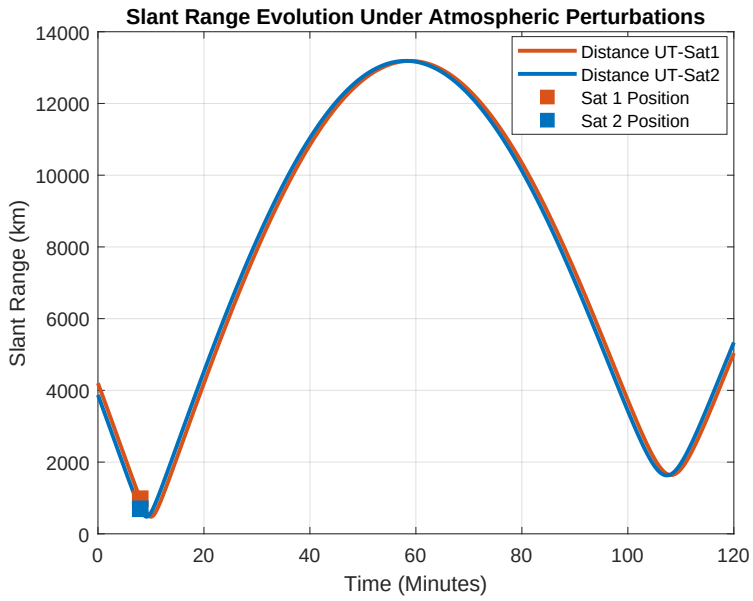

Figure 2.11: Slant Range of two LEO satellites following an imperfect orbit.

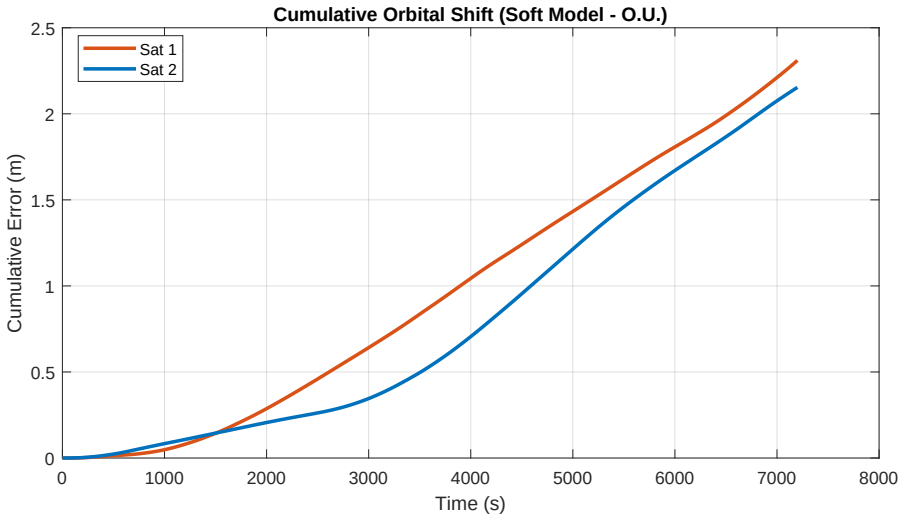

Figure 2.12: Cumulative error vs time.

The two satellites transmit DVB-S2X signals with parameters described in table. 4.1, which are to be combined at the UT. However, the UT is only capable of receiving signals from both satellites during a limited portion of the orbital period. For LEO constellations, this interval typically lasts only a few minutes. Fig. 2.13 shows a reduced section of the full orbit in Fig. 2.11. Assuming the UT can maintain synchronization with both satellites for a total of 4 minutes (2 minutes before and 2 minutes after the closest point in the orbit),

we can examine how the waveform misalignment evolves according to (2.9) when both the differential propagation path and the clock mismatch between the satellites are included in the simulations. It can be observed that, from the initial acquisition time at minute 7 to approximately minute 11, the misalignment departs from that induced solely by the differential propagation path. This deviation is caused by the mismatch between the internal clocks of Sat 1 and Sat 2.

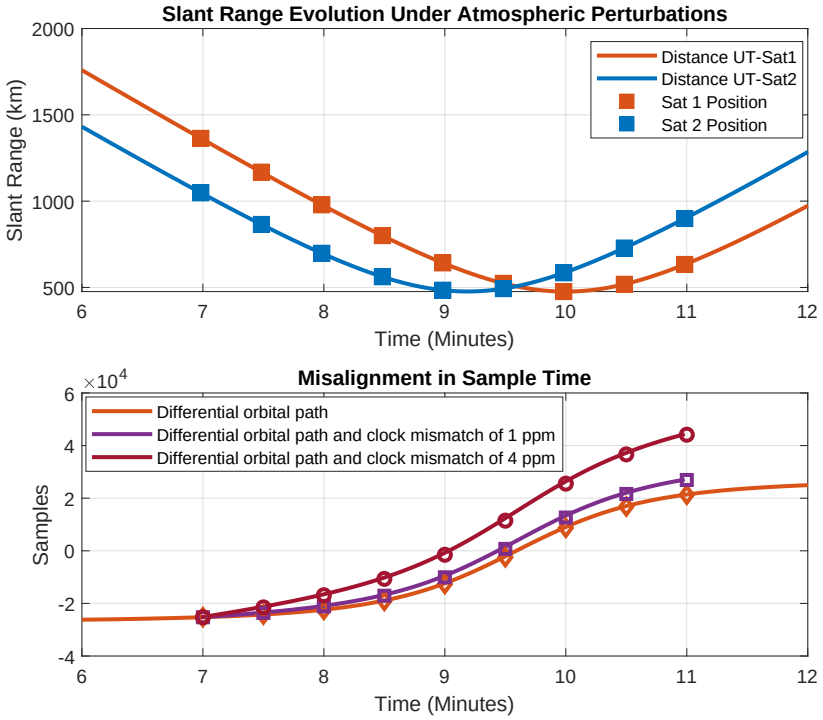

Figure 2.13: Different position of two satellites in LEO orbit around the point closer to the UT (upper image), and the misalignment between the waveforms from the UT perspective (lower image).

In the simulations, both satellites employ clocks operating at 24 MHz. We evaluate two scenarios: an ideal case in which the clocks are perfectly synchronized, and practical cases in which they exhibit mismatches of 1 ppm and 4 ppm. As expected, larger clock offsets lead to more pronounced deviations from the misalignment introduced solely by the differential propagation path.

The next step was to validate the proposed misalignment estimation procedures with realistic impairments, including a high interference scenario (scenario discussed in Section 2.2 where the two signals are overlapped in time and frequency), variable propagation delay

caused by satellite motion, and phase noise resulting from clock mismatch between the satellites and the UT. The specific simulation parameters for the communication link are outlined in Table 2.1.

Fig. 2.14 presents the estimated sample-time misalignment between the received signals at minute 7 of the scenario depicted in Fig. 2.13. The results are shown for three inter-satellite clock-skew values, 0ppm, 1ppm, and 4ppm. The simulation also incorporates different phase-noise bandwidths (1 Hz, 5 Hz, and 10 Hz) and phase-noise-attenuation levels (-75 dB, -65 dB, and -55 dB), allowing the impact of these parameters on the estimation performance to be assessed.

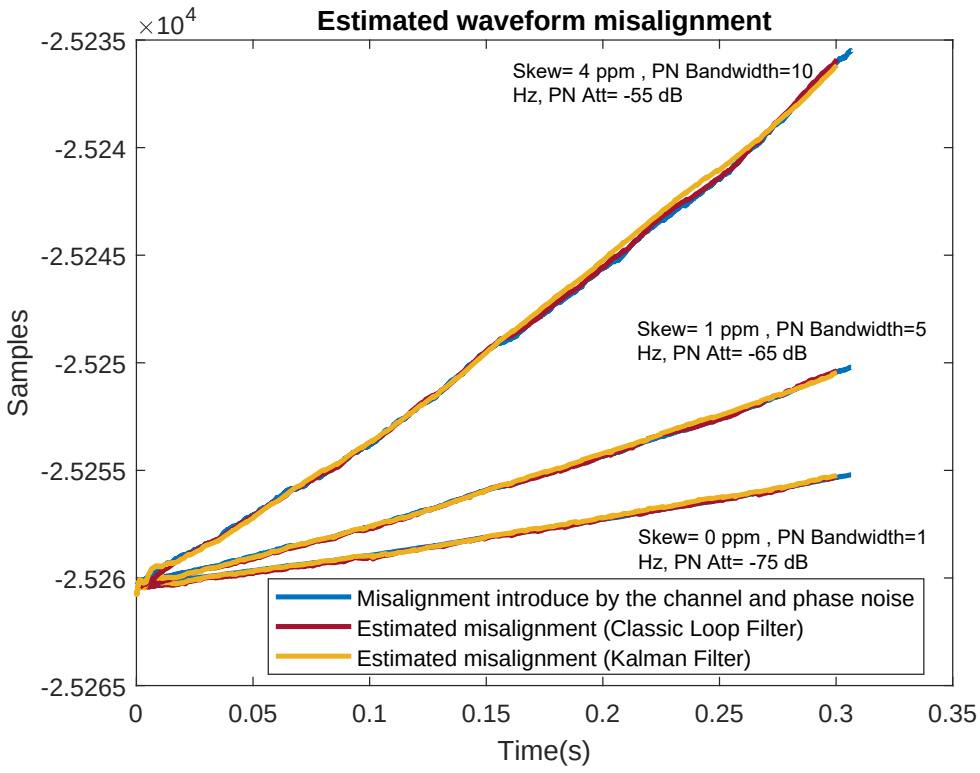

Figure 2.14: Estimated misalignment for different values of inter-satellite clock skew and phase noise.

Although the overall estimation performance is comparable for both approaches (the conventional loop filter and the Kalman filter), a closer inspection of the TED output, defined in (2.16) and shown in Fig. 2.15, reveals notable differences in convergence behavior. Specifically, the symbol-time error converges more rapidly to zero when the Kalman filter is employed compared to the classical loop-filter implementation. Moreover, the bandwidth of the

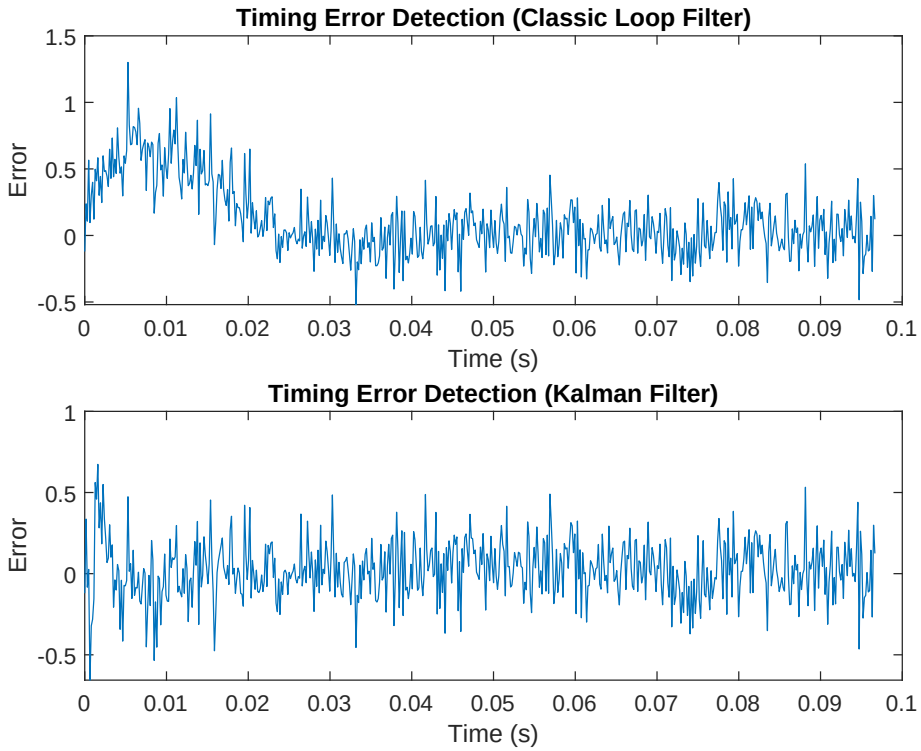

Figure 2.15: TED function when classic loop filter is employed (upper) vs when Kalman filter is employed (lower).

conventional loop filter must be manually tuned to satisfy the system requirements, whereas the Kalman filter inherently adapts to the operating conditions through its state-space formulation.

As discussed in Section 2.4, the objective is to reduce the sample-time misalignment from thousands of samples to only a few by performing an initial estimation, followed by a large corrective shift in the compensation mechanism. The alignment procedure accounts not only for the previously described impairments but also for the feedback delay from the UT to the satellites.

Table 2.1: Simulation Parameters

Waveform Standard	DVB-S2X format 2
Transmitted Signals	2
Walsh-Hadamard indices	5 and 13
Modulation Scheme	QPSK
Bandwidth	6 MHz
Oversampling Factor	4
Sampling/Clock frequency	24 MHz
SRRC Parameters	filter span=80 symbols, roll-off factor=0.2
SINR of received signals	The signals are overlapped therefore the effective SINR=0
Sample Time Misalignment	Variable
Clock Skew	0, 1 and 4 ppm
Phase Noise Bandwidth	1, 5 and 10 Hz
Phase Noise Attenuation	-75, -65 and -55 dB

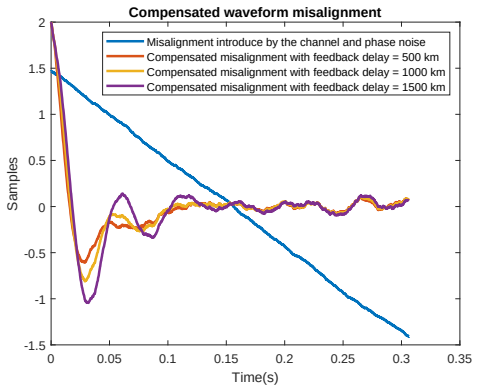

(a) Phase noise bandwidth of 1 Hz and phase noise attenuation of -75 dB.

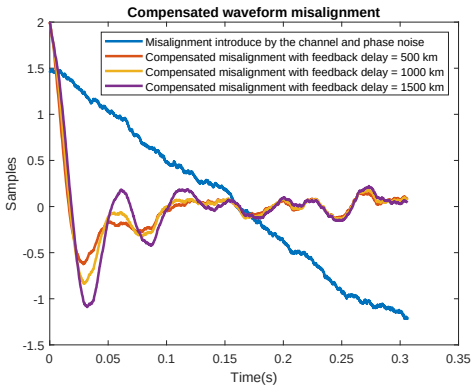

(b) Phase noise bandwidth of 5 Hz and phase noise attenuation of -65 dB.

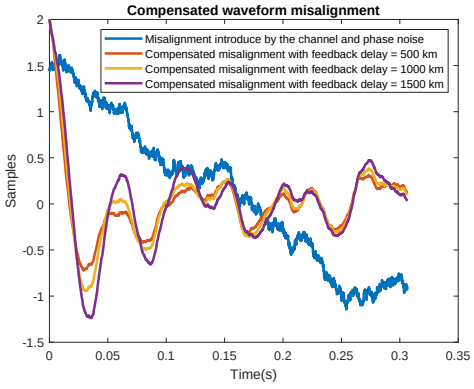

(c) Phase noise bandwidth of 10 Hz and phase noise attenuation of -55 dB.

Figure 2.16: Compensated misalignment under realistic feedback delays and phase noise.

Fig. 2.16 illustrates the waveform-alignment performance after an initial correction shift reduces the misalignment from more than 25000 samples to less than 2. Right after, the compensation mechanism starts a smooth shift of the output signal based on the misalignment feedback received from the UT. To properly simulate the distributed control loop, feedback distances of 500 Km, 1000 Km, and 1500 Km were added to the simulation parameters. It can be noticed how the increments in the feedback distances, phase noise bandwidth, and phase noise attenuation harm the alignment procedure, since it is visible how this impairment increases the system oscillations. Nevertheless, the residual misalignment is sufficiently small to enable transmit-diversity operation even in the most stringent scenario of overlapped STBC-encoded signals. As demonstrated experimentally in [56], the performance degradation of Alamouti-combined signals caused by symbol-time misalignment can be effectively compensated for offsets up to 0.5 symbol periods, which corresponds to two samples under the oversampling factor of four considered in this work.

Another aspect that must be considered is the update rate of the compensation values transmitted from the UT to the satellite. In the proposed system, the misalignment estimate is refreshed at every pilot sequence embedded in the DVB-S2X superframe. For DVB-S2X format-2 waveforms, pilot sequences occur every 956 symbols; with a sampling frequency of 24 MHz (corresponding to a 6-MHz symbol rate), this results in an update interval of approximately 159.33 μs. Each compensation update transmitted from the UT to the spacecraft is subject to a propagation delay, the values of which are summarized in Table. 2.2. As expected, larger propagation delays lead to more pronounced oscillations during the acquisition phase of the distributed compensation loop.

Table 2.2: Up-link propagation delay in seconds

Up-link distance	**Propagation delay in seconds**
500 Km	1.66 ms
1000 Km	3.33 ms
1500 Km	5.00 ms

2.6 Conclusions

This chapter addressed one of the fundamental barriers to enabling cooperative transmit-diversity schemes in distributed NGSO satellite systems: the presence of significant and dynamically

varying symbol-time misalignment at the UT. Through a detailed system analysis, we demonstrated that the combined effects of differential propagation delay and heterogeneous clock drifts can cause multi-satellite waveforms to arrive thousands of samples apart. Such misalignment severely degrades the performance of diversity-combining techniques, often rendering them ineffective in practical multi-satellite deployments. The proposed methodology provides a comprehensive framework that not only estimates these impairments with high accuracy but also compensates for them in real time.

A dual-stage estimation framework was introduced, consisting of integer misalignment detection via coarse frame synchronization and fractional misalignment tracking through DLL and Kalman-filter architectures. Simulation results show that while conventional DLL-based approaches with static loop bandwidth provide good convergence, Kalman filtering offers enhanced robustness under variable Doppler and phase-noise conditions. This enables more reliable fine-tracking performance, particularly in high-dynamics orbital regimes.

To complement the estimation process, a distributed waveform-alignment mechanism combining discrete sample shifts with continuous fractional resampling was developed. This hybrid method substantially reduces distortion and ensures smooth alignment, overcoming limitations of purely discrete shifting approaches. Numerical evaluations further confirm that the proposed distributed control-loop architecture maintains tight alignment even under significant feedback delays between the UT and satellites, thereby supporting practical implementation in real LEO systems.

Chapter 3

STBC Combining Under Imperfect Symbol Time Alignment

3.1 Introduction

This chapter introduces a robust receiver architecture that demonstrates strong resilience against SINR degradation caused by symbol time misalignment between received STBC encoded signals, and maintains robust performance even under additional impairments such as AWGN, power imbalance and Doppler shifts. Moreover, we present an efficient implementation of the receiver, and evaluate its performance in software simulations.

3.2 System Description

Consider the system model represented in Fig. 3.1, where a UT can receive signals from two distinct NGSO satellites. To provide spatial diversity, the same symbol stream is transmitted by the two satellites with distinct STBC codes. The two superimposed waveforms incorporate orthogonal pilot sequences, enabling independent synchronization for each satellite. Although the UT employs a single RF input, it requires two separate digital reception chains (one per satellite) as well as a diversity processing block, as illustrated in Fig. 3.2.

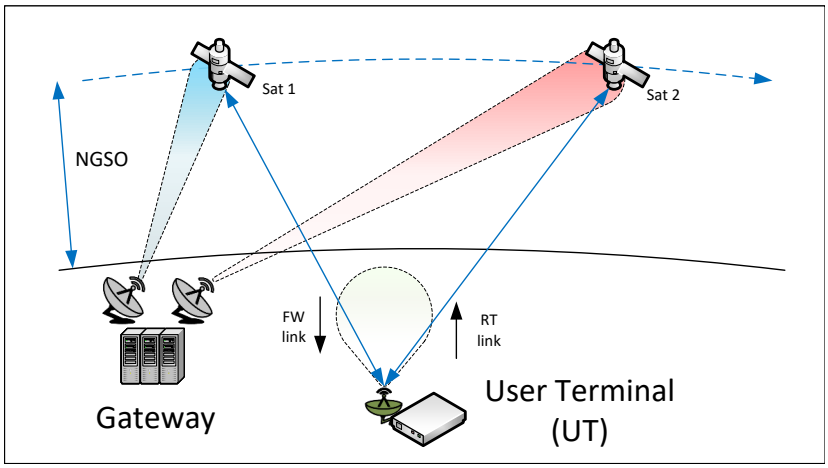

Figure 3.1: Dual satellite STBC communication scenario, with a forward link and a return link.

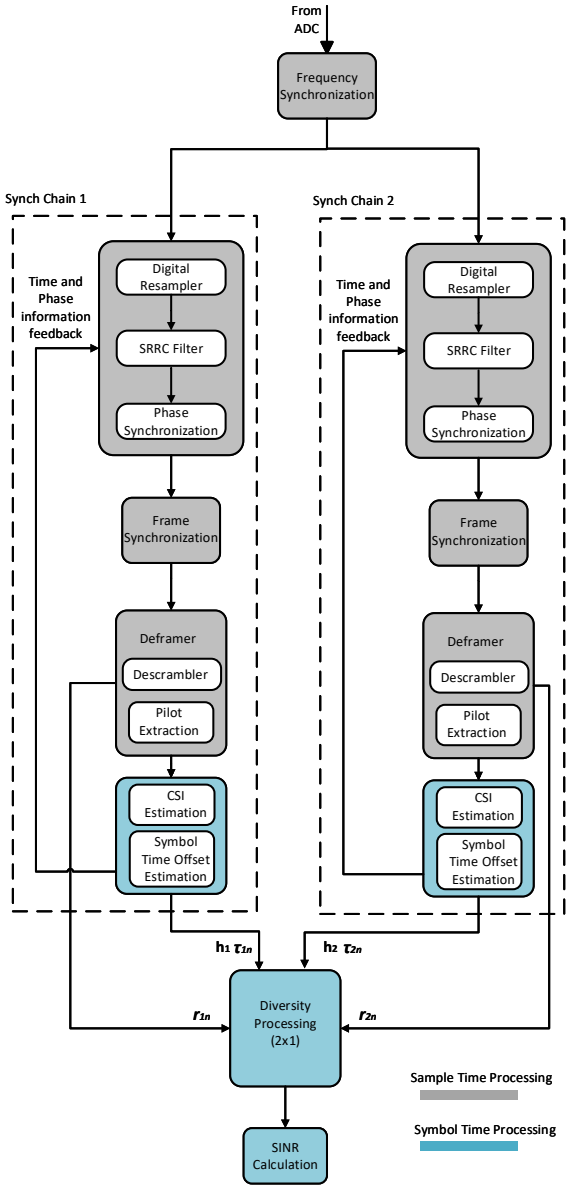

Figure 3.2: Receiver schematic with two synchronization chains (one for each satellite signal) and a diversity processing block that combines such signals after synchronization.

The encoded data symbols are embedded within the DVB-S2X waveform standard, where each waveform is transmitted using a distinct Walsh-Hadamard sequence to enable independent synchronization chains. Despite this separation, both waveforms occupy the same frequency spectrum. As a result, while each synchronization chain can lock onto only one of the two signals, both waveforms are in superposition within each chain.

Due to the relative motion between the satellites and the UT, each signal experiences a distinct and time-varying propagation path, resulting in misalignment between the incoming symbols. This misalignment not only degrades the performance of STBC due to inter-symbol delays, but also introduces ISI caused by improper time synchronization at the input of the square root raised cosine (SRRC) filter. Moreover, even after compensating for the integer symbol time misalignment as proposed in [31], the remaining fractional misalignment exhibits a time-varying behavior that must be continuously estimated.

Once the automatic gain control (AGC) and synchronization chains in Fig. 3.2 have locked onto their respective signals, the received symbols r_{1n} and r_{2n}, observed at the output of each chain, can be mathematically modeled as in (3.1) and (3.2). Let the synchronized encoded symbols from the first and second chains be denoted by a_n and b_n, respectively. It is important to note that each synchronization chain also includes the inverse sequence of encoded symbols, which remains unsynchronized and therefore acts as a source of interference in the received signal.

$$r_{1n} = a_n + \alpha_n e^{j\theta_n} \left(\sum_{k=-\infty}^{\infty} b_k g(nT_{sym} - kT_{sym} - \tau_n) \right) + z_n, \tag{3.1}$$

$$r_{2n} = b_n + \frac{1}{\alpha_n} e^{-j\theta_n} \left(\sum_{k=-\infty}^{\infty} a_k g(nT_{sym} - kT_{sym} + \tau_n) \right) + z_n. \tag{3.2}$$

Herein, α_n, θ_n, and $\tau_n = \tau_{1n} - \tau_{2n}$ denote the differential amplitude, phase, and symbol time, between the incoming signals, where τ_{1n} and τ_{2n} are the symbol time misalignment of the individual signals before the compensation applied by the digital resampler. The function g represents the impulse response of the overall channel, encompassing the transmitter filter, the wireless channel, and the receiver filter, under the assumption of a single-path (non-dispersive) scenario. T_{sym} denote the symbol period, and z_n corresponds to AWGN filtered by the SRRC filter. To combine the signals, a diversity processing block is introduced after both synchronization chains. This block utilizes the received symbols, STBC encoding matrices,

CSI estimation, and symbol time misalignment estimation to recover the original transmitted information.

3.3 Diversity Processing 2x1

The overall communication system illustrated in Fig. 3.1 can be characterized as a Multiple-Input Single-Output (MISO) configuration, in which each signal transmitted by the gateway is forwarded by a separate satellite. Spatial diversity is achieved by transmitting identical information (with different STBC codes) through both satellites, resulting in two statistically independent propagation channels. In the proposed scenario, the multipath delay spread is negligible due to the dominant line-of-sight component and minimal scattering, allowing the channel to be modeled as flat fading. This channel is represented by a complex coefficient h, which varies over time as a result of factors such as atmospheric conditions, satellite motion, UT mobility, and hardware impairments.

3.3.1 Signal Model of STBC

In a transmit diversity system with N_T antennas, a generic STBC codeword is sent over an interval of P symbol periods. Assuming that the channel propagation conditions remain invariant over the length of P, the transmitted codeword can be written as a matrix $\mathbf{S}$ with dimensions $P \times N_T$ that contains K complex symbols. Hence, the code length is P and its code rate (transmitted symbols per codeword) $R = \frac{K}{P}$ [82]. Then $\mathbf{S}$ can be expressed as:

$$\mathbf{S} = \sum_{i=1}^{K} (\mathbf{A}_i^R s_i^R + \mathbf{A}_i^I s_i^I) \tag{3.3}$$

where the information symbols are $s_i = s_i^R + j s_i^I$, representing the real (I) and imaginary (Q) components of s_i. Matrices $\mathbf{A}_i^R$ and $\mathbf{A}_i^I$, both of dimension $P \times N_T$, are called the encoding matrices of the STBC.

In the case of Alamouti STBC [20], with $N_T = K = P = 2$, the codeword matrix containing the encoded symbols can be written as:

$$\mathbf{S} = \begin{bmatrix} s_1 & s_2 \\ -s_2^* & s_1^* \end{bmatrix}, \tag{3.4}$$

where the corresponding encoding matrices are:

$$\mathbf{A}_1^R = \begin{bmatrix} 1 & 0 \\ 0 & 1 \end{bmatrix}, \mathbf{A}_2^R = \begin{bmatrix} 0 & 1 \\ -1 & 0 \end{bmatrix}, \mathbf{A}_1^I = \begin{bmatrix} 1 & 0 \\ 0 & -1 \end{bmatrix}, \mathbf{A}_2^R = \begin{bmatrix} 0 & 1 \\ 1 & 0 \end{bmatrix}. \tag{3.5}$$

The row of the STBC codeword represents the symbol to be transmitted at a particular time slot, while the column represents the symbol to be transmitted at a specific transmit antenna. Each encoding branch represents an independent communication link with a code rate of 1, which translates to an increase in the spectral efficiency when the two branches are received with the same power.

The encoded symbols are then modified by the channel coefficients $h_1 = \alpha_n e^{j\theta_n}$ and $h_2 = \frac{1}{h_1}$ respectively, and subsequently impacted by the differential time of arrival at the UT. Since the Alamouti scheme encodes two symbols over two consecutive time slots, a common representation of the received signal involves organizing the symbols into a column vector, stacking their real and imaginary components as

$$\mathbf{s} = \begin{bmatrix} s_{1R} \\ s_{1I} \\ s_{2R} \\ s_{2I} \end{bmatrix}. \tag{3.6}$$

Each symbol stream in the corresponding transmitter is encoded using the stack representation of the encoding matrices in (3.5)

$$\mathbf{A}_1 = \begin{bmatrix} 1 & 0 & 0 & 0 \\ 0 & 1 & 0 & 0 \\ 0 & 0 & -1 & 0 \\ 0 & 0 & 0 & 1 \end{bmatrix}, \tag{3.7a}$$

$$\mathbf{A}_2 = \begin{bmatrix} 0 & 0 & 1 & 0 \\ 0 & 0 & 0 & 1 \\ 1 & 0 & 0 & 0 \\ 0 & -1 & 0 & 0 \end{bmatrix}. \tag{3.7b}$$

Then at the receiver, the differential flat fading channel effects can be written in a stack

representation as well, given by the matrix as

$$\mathbf{H}_i = \begin{bmatrix} \Re(h_i) & \Im(h_i) & 0 & 0 \\ -\Im(h_i) & \Re(h_i) & 0 & 0 \\ 0 & 0 & \Re(h_i) & \Im(h_i) \\ 0 & 0 & -\Im(h_i) & \Re(h_i) \end{bmatrix}, i \in \{1, 2\}. \tag{3.8}$$

As such, to analyze the ISI introduced by the time misalignment, a block of more than two symbols must be considered. Suppose that the ISI spreads over K sets of stacked (as in (3.6)) consecutive symbols $\mathbf{s}_K$, one can re-express (3.1) and (3.2) in matrix form as

$$\mathbf{r}_{1K} = ((\mathbf{I} \otimes \mathbf{A}_1) + \mathbf{G}(\mathbf{I} \otimes (\mathbf{H}_2\mathbf{A}_2)))\mathbf{s}_K + \mathbf{z}_K, \tag{3.9a}$$

$$\mathbf{r}_{2K} = ((\mathbf{I} \otimes \mathbf{A}_2) + \mathbf{G}^T(\mathbf{I} \otimes (\mathbf{H}_1\mathbf{A}_1)))\mathbf{s}_K + \mathbf{z}_K, \tag{3.9b}$$

wherein, $\mathbf{I}$ be the identity matrix with dimensions $(K \times K)$, $\mathbf{G}$ being a matrix function of the symbol time misalignment between the signals, formed as a block-circulant $(4K \times 4K)$ matrix whose rows are the shifted values of the overall (transmitter and receiver) SRRC function evaluated on the parameter τ_n.

Fig. 3.3 shows the difference in the ISI contribution of the SRRC filter when the input symbols are time synchronized vs when they are not. For the case of $\tau_n = 0$ (time synchronized symbols), $\mathbf{G} = \mathbf{I}$, however, when $\tau_n \neq 0$ (not time synchronized symbols), $\mathbf{G} \neq \mathbf{I}$.

As in any practical system, the parameters τ_n, α_n, and θ_n used to describe the received signal model must be estimated, hence, the estimated (imperfect) values may differ from the actual (perfect) ones. For the case of time misalignment estimation, we can define the imperfect estimation as:

$$\tilde{\tau}_n = \tau_n + \tau_\epsilon \tag{3.10}$$

Where τ_ϵ is the error of the estimation. Furthermore, since the matrix $\mathbf{G}$ is formed using the estimated values of the misalignment, the imperfect version of it would be defined as:

$$\tilde{\mathbf{G}}(\tau_n + \tau_\epsilon) = \mathbf{G} + \mathbf{G}_\epsilon \tag{3.11}$$

Where $\mathbf{G}_\epsilon$ would be an error in the representation of the ISI contribution from the SRRC

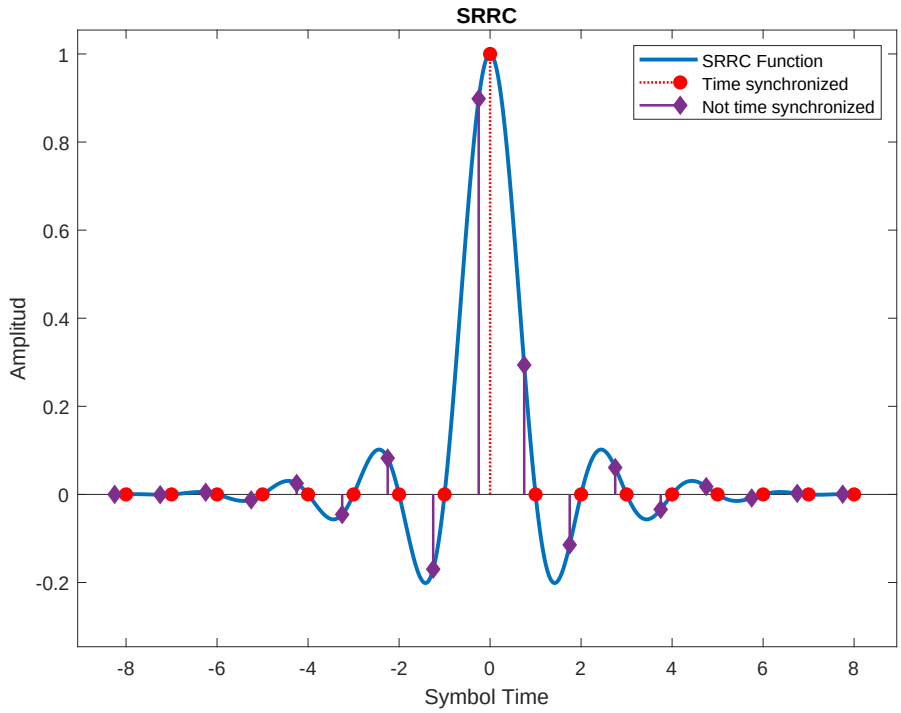

Figure 3.3: The blue curve represents the continuous SRRC filter function. In contrast, the red circles indicate the discrete weights used to weight the output of the synchronized symbols, while the purple diamonds represent the weights applied to the non-synchronized symbols.

filter.

On the other hand, the relationship between the perfect and imperfect CSI estimation can be expressed as in [83]:

$$\tilde{h}_i = \sqrt{1-\sigma_h^2}h_i + \sqrt{\sigma_h^2}h_\epsilon \tag{3.12}$$

Where σ_h^2 is the estimator error variance, and h_ϵ is the error which follows a normal distribution $\mathcal{CN}(0, \sigma_h^2)$.

If we define the effective channel matrices in (3.9a) and (3.9b) as the following quantities

$$\mathbf{\Psi}_1 = (\mathbf{I} \otimes \mathbf{A}_1) + \tilde{\mathbf{G}}(\mathbf{I} \otimes (\tilde{\mathbf{H}}_2\mathbf{A}_2)), \tag{3.13a}$$

$$\mathbf{\Psi}_2 = (\mathbf{I} \otimes \mathbf{A}_2) + \tilde{\mathbf{G}}^T(\mathbf{I} \otimes (\tilde{\mathbf{H}}_1\mathbf{A}_1)), \tag{3.13b}$$

we can recover the transmitted symbols via pseudo-inverse approximation given by

$$\tilde{\mathbf{s}}_{1K} = \underbrace{\left(\mathbf{\Psi}_1{}^{\top}\mathbf{\Psi}_1\right)^{-1}\mathbf{\Psi}_1{}^{\top}}_{\mathbf{\Gamma}_{\text{sol1}}}\mathbf{r}_{1K}, \tag{3.14a}$$

$$\tilde{\mathbf{s}}_{2K} = \underbrace{\left(\mathbf{\Psi}_2{}^{\top}\mathbf{\Psi}_2\right)^{-1}\mathbf{\Psi}_2{}^{\top}}_{\mathbf{\Gamma}_{\text{sol2}}}\mathbf{r}_{2K}. \tag{3.14b}$$

Herein, $\mathbf{\Gamma}_{\text{sol1}}$ will be called solution matrix 1 and $\mathbf{\Gamma}_{\text{sol2}}$ will be solution matrix 2. For the final approximation of the transmitted symbols, we use the maximum ratio combining of the two branches as

$$\tilde{\mathbf{s}_K} = \frac{|h_1|\tilde{\mathbf{s}_{1K}} + |h_2|\tilde{\mathbf{s}_{2K}}}{|h_1|^2+|h_2|^2}. \tag{3.15}$$

An analytical expression for the SINR after the combining was developed in [17] and is given by:

$$SINR = 10log_{10}\left(\frac{\sigma_s^2}{\sigma_z^2}\right) - 10log_{10}\left(\frac{\|\mathbf{\Gamma}_{\text{sol}}\boldsymbol{Q}\|_F^2}{2K}\right), \tag{3.16}$$

where σ_s^2 is the variance of the transmitted symbols, σ_z^2 represents the variance of the filtered noise, $\mathbf{\Gamma}_{\text{sol}} = [\mathbf{\Gamma}_{\text{sol1}}; \mathbf{\Gamma}_{\text{sol2}}]$ is the concatenated solution matrices for each branch and $\boldsymbol{Q} = [Q_1; Q_2]$ denotes the matrix for the AWGN at the receiver, filtered by the SRRC and downsampled.

3.3.2 Numerical Approach

To implement the analytical approach presented above, one must find efficient numerical methods for calculating the solution matrices $\mathbf{\Gamma}_{\text{sol1}}$, $\mathbf{\Gamma}_{\text{sol2}}$ and multiply them by the incoming symbols. While analyzing (3.14a) and (3.14b), it becomes evident that, following a classical linear algebra approach, two matrix multiplications and one matrix inversion are required to compute $\mathbf{\Gamma}_{\text{sol1}}$ and $\mathbf{\Gamma}_{\text{sol2}}$. Due to the time-varying nature of the parameters h_1, h_2, and τ_n, both solution matrices must be updated rapidly to track channel variations and adapt to varying conditions without significantly degrading system performance. Although matrix inversion is a common operation in adaptive communication systems, its computational complexity increases rapidly with matrix size. Consequently, considerable research work has focused on exploiting specific matrix structures to reduce the complexity of inversion algorithms [65].

From (3.13a) and (3.13b), it can be noticed that all Kronecker products are performed

between an identity matrix $\boldsymbol{I}$ of dimensions $(K \times K)$ and squared matrices of dimensions (4×4), which leads to block-circulant matrices of dimension $(4K \times 4K)$. On the other hand, the structure of the $\mathbf{G}$ matrix is also block-circulant with dimensions $(4K \times 4K)$. Therefore, $\boldsymbol{\Psi}_1$ and $\boldsymbol{\Psi}_2$ are block-circulant matrices composed of K smaller (4×4) real matrices $\boldsymbol{\varphi}_1, \cdots \boldsymbol{\varphi}_K$ in each of the K rows, represented as $\boldsymbol{\Psi}_i,\ i \in \{1, 2\}$

$$\boldsymbol{\Psi_i} = \begin{bmatrix} \boldsymbol{\varphi}_1 & \boldsymbol{\varphi}_2 & \cdot & \cdot & \boldsymbol{\varphi}_{K-1} & \boldsymbol{\varphi}_K \\ \boldsymbol{\varphi}_K & \boldsymbol{\varphi}_1 & \cdot & \cdot & \boldsymbol{\varphi}_{K-2} & \boldsymbol{\varphi}_{K-1} \\ \boldsymbol{\varphi}_{K-1} & \boldsymbol{\varphi}_K & \cdot & \cdot & \boldsymbol{\varphi}_{K-3} & \boldsymbol{\varphi}_{K-2} \\ \cdot & \cdot & \cdot & \cdot & \cdot & \cdot \\ \boldsymbol{\varphi}_2 & \boldsymbol{\varphi}_3 & \cdot & \cdot & \boldsymbol{\varphi}_K & \boldsymbol{\varphi}_1 \end{bmatrix}. \tag{3.17}$$

One advantage of block-circulant matrices is that their inverse can be calculated relatively easily with the help of the Discrete Fourier Transform (DFT). A description of such an approach is proposed in [65], and is based on an extension of the Fourier decomposition of circulant matrices.

If a circulant matrix $\boldsymbol{C}_{N\times N}$ is composed of shifted versions of a column vector $\boldsymbol{c}_{N\times1}$, then such a matrix can be decomposed as

$$\boldsymbol{C} = \boldsymbol{F^H} \left(\text{diag}\left(\sqrt{N}\boldsymbol{F}\boldsymbol{c}\right)\right) \boldsymbol{F}, \tag{3.18}$$

with $\boldsymbol{F}$ represents the Fourier unitary matrix, whose components are $f_{n,k} = \exp\left[\frac{-j2\pi nk}{N}\right]$. Further, the inverse $\boldsymbol{C}^{-1}$ can be given as

$$\begin{aligned} \boldsymbol{C^{-1}} &= \left(\boldsymbol{F}^H \,\text{diag}\left(\sqrt{N}\boldsymbol{F}\boldsymbol{c}\right) \boldsymbol{F}\right)^{-1} \\ &= \boldsymbol{F}^{-1} \,\text{diag}^{-1}\left(\sqrt{N}\boldsymbol{F}\boldsymbol{c}\right) \left(\boldsymbol{F}^H\right)^{-1} \\ &= \boldsymbol{F}^H \,\text{diag}^{-1}\left(\sqrt{N}\boldsymbol{F}\boldsymbol{c}\right) \boldsymbol{F}. \end{aligned} \tag{3.19}$$

This approach can be naturally extended to compute the pseudo-inverse required for obtaining the solution matrices $\boldsymbol{\Gamma}\text{sol}_\mathbf{1}$ and $\boldsymbol{\Gamma}\text{sol}_\mathbf{2}$, without introducing significant additional complexity. For this purpose, we define the (4×4) complex matrices $\varphi^{(1)}, \ldots, \varphi^{(K)}$, which are related to

$\varphi_1, \ldots, \varphi_K$ through the DFT relations as

$$\boldsymbol{\varphi}_k = \sum_{n=1}^{K} \boldsymbol{\varphi}^{(n)} \alpha_n^{k-1}, \quad k = 1, \cdots, K, \tag{3.20a}$$

$$\boldsymbol{\varphi}^{(n)} = \frac{1}{K} \sum_{k=1}^{K} \boldsymbol{\varphi}_k \left(\alpha_n^*\right)^{k-1}, \quad n = 1, \cdots, K, \tag{3.20b}$$

with $\alpha_n = \exp\left[j\frac{2\pi}{K}(n-1)\right]$. Now, one can compute $\boldsymbol{\Gamma}_{\text{soli}}, i \in \{1, 2\}$ as

$$\boldsymbol{\Gamma}_{soli} = \begin{bmatrix} \boldsymbol{\xi}_1 & \boldsymbol{\xi}_2 & \cdot & \cdot & \boldsymbol{\xi}_{K-1} & \boldsymbol{\xi}_K \\ \boldsymbol{\xi}_K & \boldsymbol{\xi}_1 & \cdot & \cdot & \boldsymbol{\xi}_{K-2} & \boldsymbol{\xi}_{K-1} \\ \boldsymbol{\xi}_{K-1} & \boldsymbol{\xi}_K & \cdot & \cdot & \boldsymbol{\xi}_{K-3} & \boldsymbol{\xi}_{K-2} \\ \cdot & \cdot & \cdot & \cdot & \cdot & \cdot \\ \boldsymbol{\xi}_2 & \boldsymbol{\xi}_3 & \cdot & \cdot & \boldsymbol{\xi}_K & \boldsymbol{\xi}_1 \end{bmatrix}, \tag{3.21}$$

$$\text{with } \boldsymbol{\xi}_k = \frac{1}{(K)^2} \sum_{n=1}^{K} \alpha_n^{k-1} \left(\left(\boldsymbol{\varphi}^{(n)}\right)^H \boldsymbol{\varphi}^{(n)} \right)^{-1} \left(\varphi^{(n)}\right)^H. \tag{3.22}$$

Herein, $\boldsymbol{\xi}_k$ is a real matrix of dimension (4×4). Once again, we can leverage the block-circulant structure of the solution matrix when multiplying it by the incoming symbols. This process can be made relatively simple, since multiplying a row vector by a block-circulant matrix (as in (3.14a) and (3.14b)) is equivalent to performing a circular convolution between the first row of blocks in the solution matrix, and the row vector. Furthermore, circular convolution can be approximated by linear convolution if one of the sequences is padded with zeros at the beginning and the end as:

$$\mathbf{s}_{\tilde{iK}} = \boldsymbol{\xi}_K \circledast \mathbf{r}_{iK} \approx [\mathbf{0}\boldsymbol{\xi}_K\mathbf{0}] * \mathbf{r}_{iK}. \tag{3.23}$$

It's noteworthy that linear convolution is a well-researched topic and can be easily implemented in the form of an FIR filter.

3.4 Numerical Results

To numerically evaluate the proposed system's performance, we generated two Alamouti encoded symbol streams and embedded them into DVB-S2X waveforms. The simulation

parameters are presented in Table. 4.1 and were selected based on the properties of the hardware equipment used to validate the system implementation in the next chapter. Since the experiments in this chapter are limited to software simulations, a wider range of impairments (AWGN, time misalignment, power imbalance, and Doppler Shift) were used to test the system performance.

When using the Alamouti scheme with two antennas, an expected SINR gain of 3 dB can be achieved after combining the signals [20]. However, this gain is contingent upon two critical conditions: precise time alignment and equal amplitude of both signals. If a symbol-time misalignment is introduced between the waveforms, the resulting combined SINR undergoes significant degradation, primarily due to ISI induced by the SRRC filter at the UT, as detailed in (3.1) and (3.2).

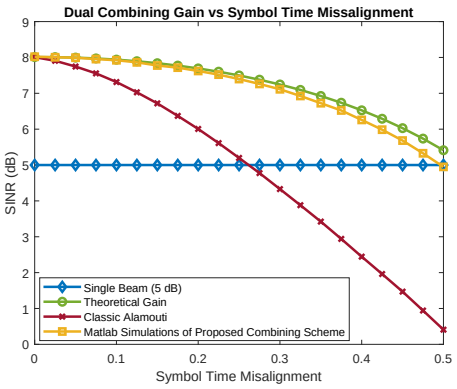

(a) Individual SNR=5 dB

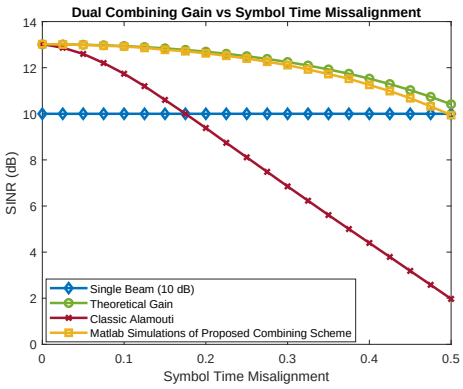

(b) Individual SNR=10 dB

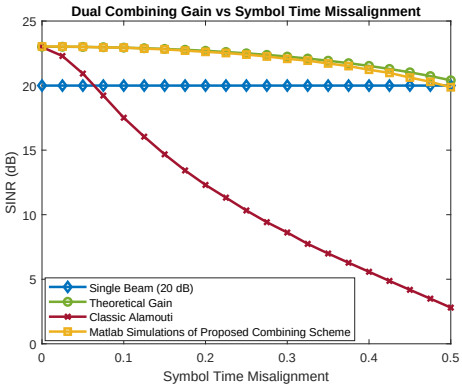

(c) Individual SNR=20 dB

Figure 3.4: SINR in Alamouti scheme vs symbol time misalignment when combining two signals in three individual SNR regimes of 5, 10, 20 dBs.

Fig. 3.4 illustrates the SINR improvements achieved through the methods described in

this chapter. The blue curve represents the SNR of a single beam (i.e., the signal from an individual satellite), while the remaining three curves depict the SINR of combined signals under both synchronous (zero symbol time misalignment) and asynchronous (non-zero symbol time misalignment) combining scenarios. In the synchronous case, the combined signals exhibit a 3 dB SINR gain relative to the individual beams from each satellite. However, as time misalignment increases, the SINR performance of the classic Alamouti combining receiver (red curve) degrades significantly. Notably, the combined signals most susceptible to time misalignment are those with higher individual SNR, where the impact of ISI is more pronounced. In contrast, signals with lower individual SNR exhibit less degradation from ISI, as additive noise becomes the dominant factor affecting signal quality. On the other hand, the proposed combining method demonstrates strong resilience to such degradation. Specifically, the green curve shows the theoretical SINR gain in (3.16), and the yellow curve presents results from MATLAB simulations. Notably, even when the symbol time misalignment reaches 0.5, resulting in a loss of combining gain, the SINR degradation remains limited to approximately 3 dB.

If we consider the case with the SNR regimes of 5 and 10 dBs for individual signals and analyze the symbol error rate (SER) (Fig. 3.5), it becomes obvious how the proposed receiver outperforms the classic Alamouti receiver when time synchronization between the signals is lost.

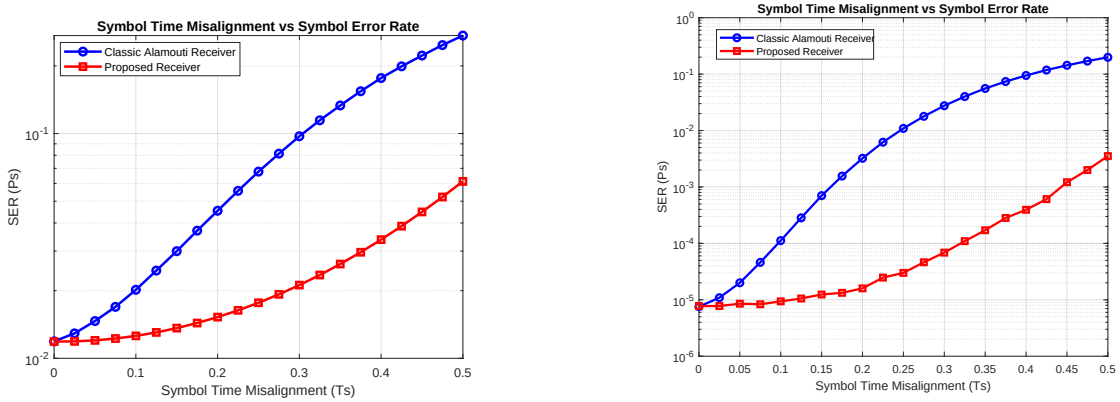

(a) Individual SNR=5 dB

(b) Individual SNR=10 dB

Figure 3.5: SER in Alamouti scheme vs symbol time misalignment when combining two signals in two individual SNR regimes of 5 and 10 dBs.

In most cases, signals transmitted from distributed satellites arrive at the receiver with different amplitudes, a phenomenon known as power imbalance. This effect is primarily

caused by variations in propagation path lengths and fading events. In waveform standards such as DVB-S2X, adaptive modulation and coding (modcod) schemes are typically employed, thus a degradation in signal SNR often results in a shift to a lower-order modulation and a higher forward error correction (FEC) rate, leading to reduced throughput. Therefore, the capability of providing a semi-stable SINR gain under time-varying channel conditions is a highly desired one.

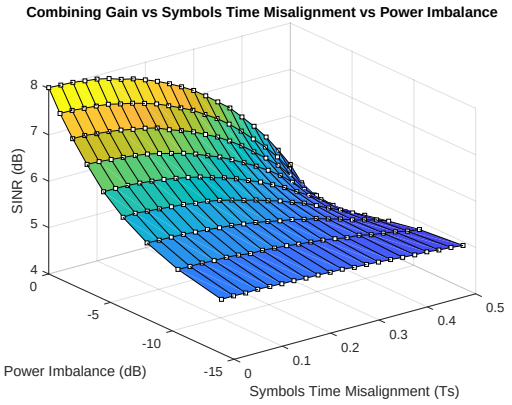

(a) Individual SNR=5 dB

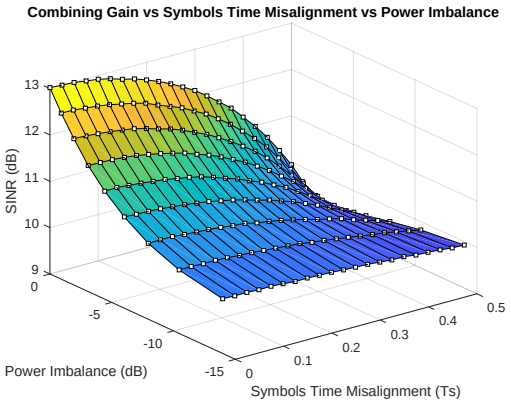

(b) Individual SNR=10 dB

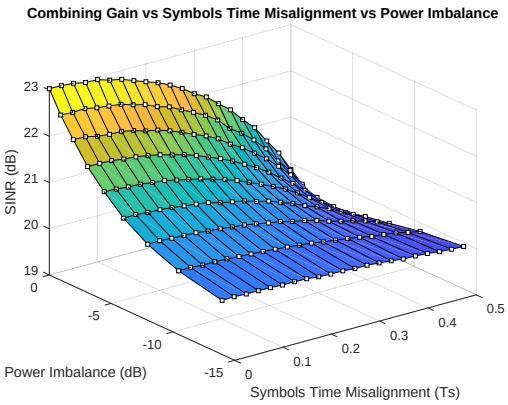

(c) Individual SNR=20 dB

Figure 3.6: SINR gain vs symbol time misalignment vs power imbalance, when combining two signals in the three SNR regimes 5, 10, and 20 dBs.

Figs. 3.6 illustrates the variation in SINR gain as a function of symbol time misalignment and power imbalance for the three SNR regimes analyzed before. In this analysis, the SNR of one signal is progressively reduced, introducing a power imbalance of up to 14 dB between the signals, while the misalignment is incrementally increased from 0 to 0.5 symbol time. As observed, the system consistently maintains a quasi-stable SINR, with degradations limited to approximately 3 dB even in the worst-case scenario of 0.5 symbol time misalignment. This

is possible due to the redundancy provided by the power stability of the signal with the stable (time-invariant) amplitude.

One of the key parameters for effective signal combining using Alamouti scheme is the differential phase between the incoming symbols. In satellite communication systems, however, this differential phase can exhibit rapid variations when signals originate from different satellites. These fluctuations are primarily caused by frequency shifts resulting from the Doppler effect. Although some compensation methods can be employed [33], a remnant Doppler shift (as commonly known) will always persist.

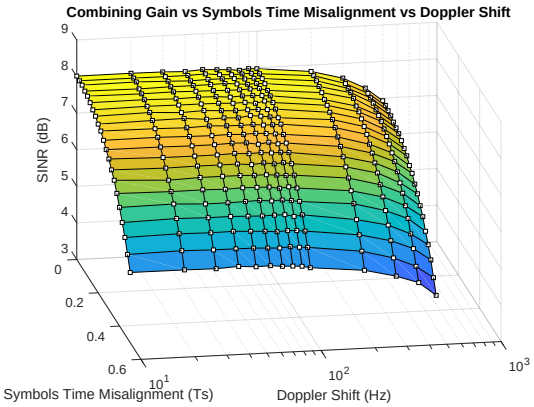

(a) Individual SNR=5 dB

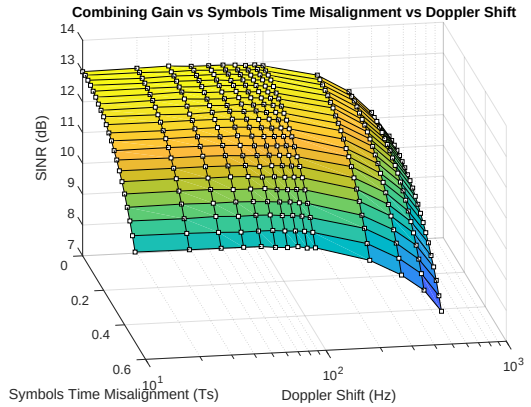

(b) Individual SNR=10 dB

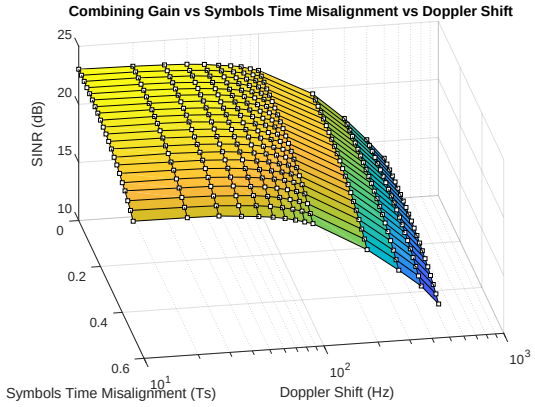

(c) Individual SNR=20 dB

Figure 3.7: SINR gain vs symbol time misalignment vs Doppler shift.

Fig. 3.7 illustrates the impact of Doppler shifts up to 500 Hz on the SINR gain. Where the differential phase measurement is updated every 956 symbols, corresponding to the pilot spacing in the DVB-S2X format 2 standard. It can be observed that as the Doppler shift increases, the SINR gain decreases, reflecting the growing difficulty of the synchronization

system in accurately tracking the differential phase between signals.

Another source of performance degradation arises from inaccuracies in the estimation of the parameters used for signal combining. Since system performance critically depends on the accurate characterization of the effective channel matrices, denoted by $\Psi_{1,2}$, it is important to evaluate the sensitivity of the combining scheme to these imperfections. In particular, estimation errors in the symbol-time misalignment and in the differential CSI can significantly affect the achievable combining gain. Fig. 3.8 illustrates the resulting SINR performance when the estimated symbol-time misalignment includes an error τ_ϵ equal to 0%, 1%, 2%, 3%, and 4% of the total symbol period.

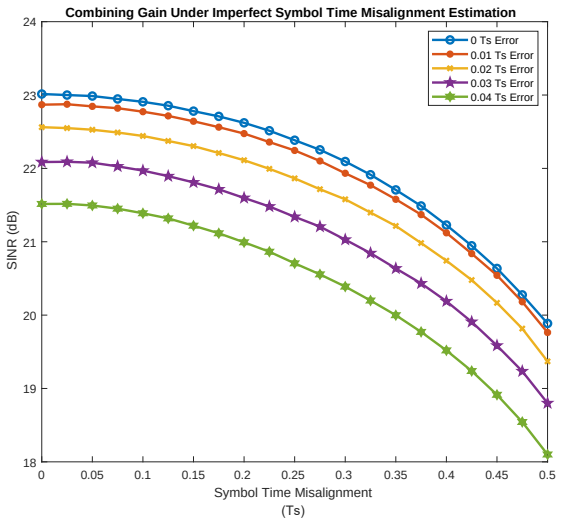

Figure 3.8: SINR of combined signals with individual SNR of 20 dB under imperfect symbol time misalignment estimation.

Another critical aspect is the impact of symbol time misalignment on the estimation of CSI in overlapped waveforms. It is well established that perfectly aligned Walsh Hadamard sequences (like the ones used in the pilot fields) exhibit complete orthogonality. However, when this orthogonality degrades due to time misalignment, the variance of the CSI estimator increases accordingly. (Fig. 3.9).

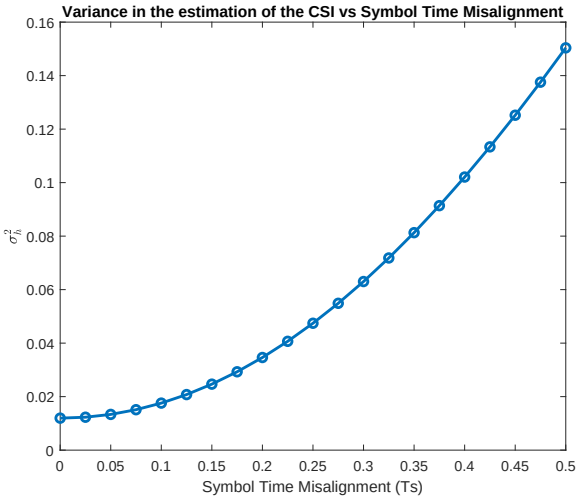

Figure 3.9: Variance in the CSI estimation under imperfect pilot alignment.

As it is to be expected, an increase in the variance of the CSI estimation has a negative impact on the resulting SINR after combining. Fig 3.10 shows the degradation in the combining gain when the variance from Fig. 3.9 is introduced into the CSI estimation used to generate the solution matrices. Similar results are shown in Fig. 3.11 where an increase in SER can be noticed for an imperfect CSI estimation.

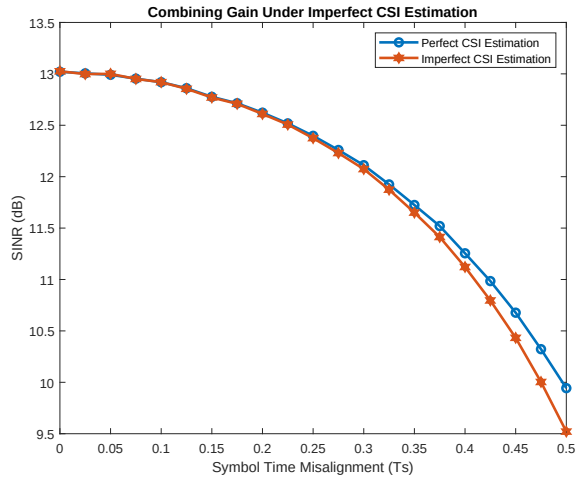

Figure 3.10: Effect of variance in the CSI estimation when combining two signals with individual SNR of 10 dB.

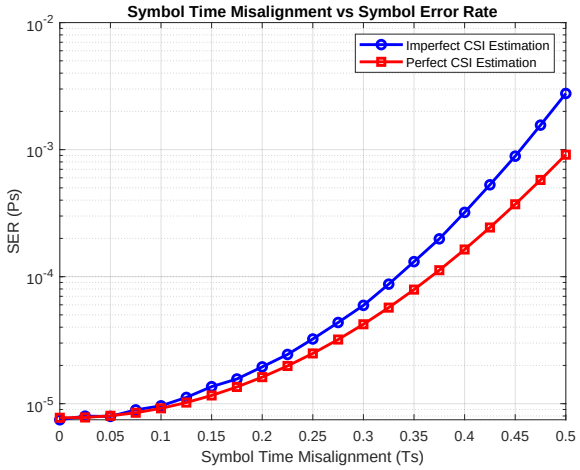

Figure 3.11: Symbol Error Rate for performance under imperfect CSI estimation, when combining two signals with individual SNR of 10 dB.

Both Figures 3.10 and 3.11 are a reflection of how the symbol time misalignment has a direct impact not only on the combining process, but also on the parameter estimation before the combining process. The greater the variance in the CSI estimation due to waveform misalignment, the more the combined results will deviate from the one obtained under perfect CSI estimation.

3.5 Conclusions

This chapter presents a novel receiver architecture designed for distributed STBC-based satellite communication scenarios, addressing the critical challenge of symbol-level time misalignment alongside other practical impairments such as power imbalance and Doppler shift. An analytical description of the system is provided, complemented by numerical methods that facilitate real-time implementation. By explicitly incorporating time-misalignment information into the combining process, the proposed receiver achieves substantial performance gains over conventional approaches, particularly under imperfect signal alignment. The robustness of the system is further demonstrated under typical satellite impairments, maintaining consistent SINR and SER performance. In addition, an error analysis is conducted to quantify performance degradation resulting from estimation inaccuracies in symbol-time misalignment and CSI, both essential for the combining operation. Future work will explore extensions to alternative waveform standards, including OFDM-based systems as adopted in 5G NR.

Chapter 4

Testbed Development

4.1 Introduction

This chapter focuses on the hardware validation of the methods introduced in Chapter 3, specifically addressing the transmission of the Alamouti encoded signals, the incorporation of channel impairments, and the reception and combining of the symbol streams. The measurement results are then compared with the theoretical and software-based outcomes presented in the previous chapter.

4.2 Prototyping Telecommunication Systems Using LabVIEW and National Instruments USRP

The increasing complexity of modern telecommunication systems has motivated the adoption of flexible prototyping platforms capable of bridging the gap between theoretical design, numerical simulation, and real-world experimentation. In this context, LabVIEW (Laboratory Virtual Instrument Engineering Workbench) combined with National Instruments USRP devices, provides a powerful environment for the rapid development and validation of wireless communication system prototypes. LabVIEW is a graphical programming environment specifically designed for measurement, signal processing, and control applications. Its dataflow-based programming paradigm allows users to construct signal processing chains using intuitive block diagrams, which closely resemble theoretical system models commonly used in telecommunications. This visual approach greatly facilitates the implementation of complex algorithms such as modulation and demodulation, channel coding, synchronization,

and channel estimation, while maintaining readability and modularity of the system design. Furthermore, LabVIEW offers extensive libraries for digital signal processing (DSP), communications, and FPGA programming, enabling both high-level system modeling and low-level hardware control within a unified framework.

The USRP is a flexible SDR platform that enables real-time transmission and reception of RF signals over a wide range of frequencies and bandwidths. NI USRP devices integrate high-speed ADCs, digital-to-analog converters (DACs), RF front-ends, and programmable logic, allowing signal generation and acquisition under realistic channel conditions. When coupled with LabVIEW, the USRP acts as a configurable RF front-end that translates baseband signal processing algorithms into real over-the-air transmissions, thus enabling experimental validation of communication concepts that go beyond purely simulated environments.

A key advantage of the LabVIEW–USRP combination lies in its end-to-end prototyping capability. A complete telecommunication system comprising a transmitter, propagation channel, and receiver can be designed, implemented, and tested using a single integrated platform. At the transmitter side, baseband signal generation, modulation schemes (e.g., PSK, QAM, OFDM), pulse shaping, and framing can be defined in software. These signals are then passed to the USRP for RF upconversion and transmission. At the receiver, the USRP digitizes the incoming RF waveform and streams the samples back to LabVIEW, where synchronization, equalization, demodulation, and decoding algorithms are applied in real time.

Another important feature of this framework is its support for real-time experimentation and hardware-in-the-loop validation. Unlike offline simulations, the LabVIEW–USRP platform exposes the communication system to practical impairments such as oscillator phase noise, carrier frequency offset, timing errors, hardware nonlinearities, and environmental channel effects. This allows researchers to assess the robustness of their algorithms under realistic operating conditions and to iteratively refine system parameters based on empirical measurements.

In addition, LabVIEW provides seamless integration with FPGAs embedded within many NI USRP models. Computationally intensive or latency-critical signal processing tasks can be offloaded to hardware accelerators, enabling high-throughput and low-latency implementations that are representative of practical transceiver architectures. This capability is particularly valuable for prototyping advanced communication techniques such as massive MIMO,

adaptive beamforming, and low-latency physical-layer processing. From a research perspective, the LabVIEW–USRP ecosystem supports rapid prototyping and reproducibility. Parameterized system designs, reusable virtual instruments, and automated measurement routines facilitate systematic performance evaluation and comparison across different scenarios. As a result, this platform is well suited for validating theoretical models, testing novel algorithms, and producing experimentally grounded results for academic publications and doctoral research.

In summary, LabVIEW combined with NI USRP devices constitutes a versatile and efficient platform for designing and prototyping telecommunication systems. By enabling real-time, over-the-air experimentation with close alignment between theory, simulation, and hardware implementation, this approach significantly enhances the credibility and practical relevance of research outcomes in modern wireless communications.

4.3 Experimental Testbed

To emulate the scenario in Fig. 3.1, three USRPs from NI were employed, one for the gateway, one for the channel emulator, and one for the UT, all of them interconnected as shown in Fig. 4.1 and 4.2. The gateway and channel emulator were implemented on the USRP model 2944R, which features an internal FPGA Kintex-7 410T from Xilinx (AMD). On the other hand, the UT was implemented on a USRP model 2974 owing to the additional presence of an internal Intel Core i7 6822EQ processor, which communicates through PCI Express with the FPGA (same family as in the 2944R), which makes this model ideal for the fast interactions required between the software and hardware parts of the design.

Fig. 4.3 illustrates a diagram of the gateway in which random data bits are generated, mapped into M-PSK symbols, encoded, and transmitted through the two RF outputs of the 2944R USRP.

An important aspect to consider in the gateway design is the impact of the scrambler on the non-synchronized symbols in (3.9a) and (3.9b). The ISI introduced by timing misalignment, as the signal passes through the SRRC filter at the UT, affects the scrambled symbols. However, the compensation for this timing misalignment occurs after the symbols are descrambled. As a result, the ISI that is compensated does not match the ISI originally introduced by the SRRC filter (see proof in Appendix A). For this reason, in our experiments,

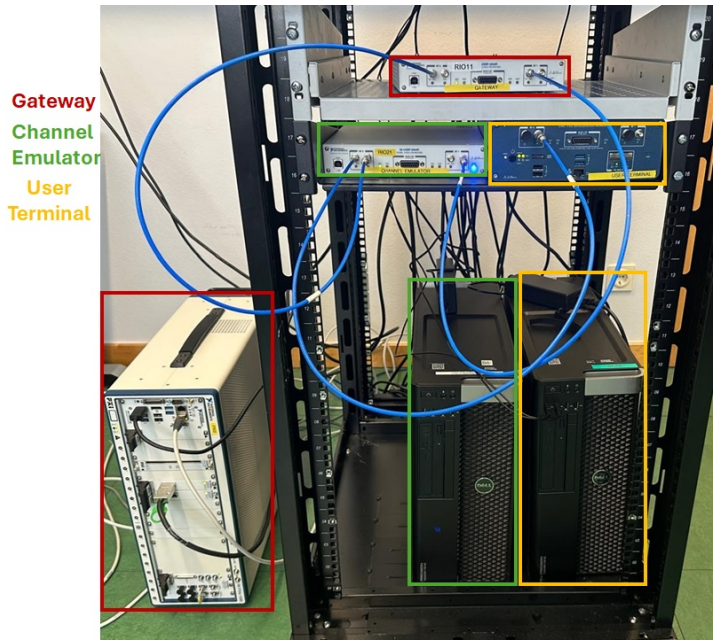

Figure 4.1: 2 × 1 Diversity combining Testbed. Each USRP is connected to a PC running LabVIEW which is used to initialize and configure the experiments.

we chose to deactivate the data scrambler while keeping the synchronization sequence scrambler active. This configuration is feasible due to the two-way scrambler mechanism defined in the DVB-S2X standard [62].

The channel impairments used in the hardware validation were added to the signals using a satellite link channel emulator, whose block diagram is shown in Fig. 4.4. The emulator introduces controllable impairments, including differential delays [84], amplitude, phase rotation, and additive noise [85]. The last step in the channel emulator is to add the signals into a single stream and transmit it to the UT. This configuration is illustrated in Fig. 4.1, where two input lines from the gateway feed into the channel emulator, and a single output line connects the emulator to the UT. A detailed description of the communication link parameters is provided in Table 4.1.

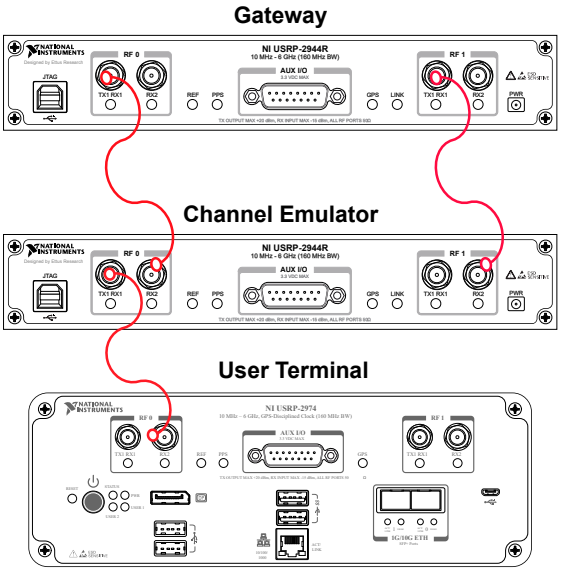

Figure 4.2: Detailed connection between RF input and outputs of Gateway, Channel Emulator, and UT USRPs.

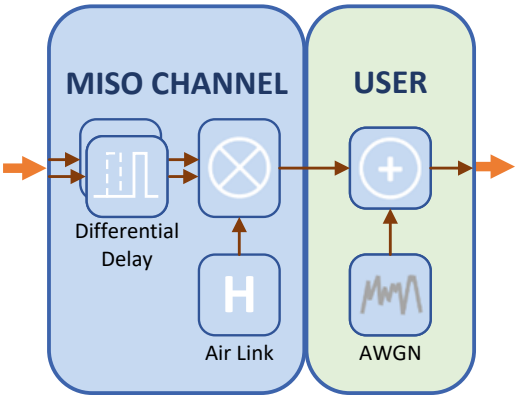

Figure 4.4: Satellite link channel emulator. Differential Delay: Allows for the control of the sample time misalignment between waveforms. Air Link (Channel Matrix): Is used to apply phase rotation and change the amplitude of the signals. AWGN: Introduces Gaussian noise to the link.

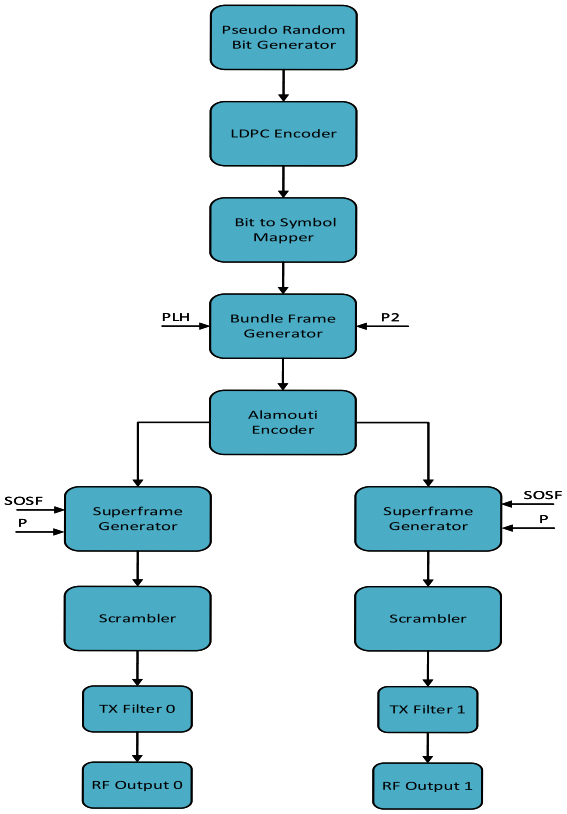

Figure 4.3: In the gateway diagram, the Alamouti encoder is placed after the bundle frame generation but before the superframe generator so that the synchronization sequences (SOSF and P) can be used in the synchronization process needed at the UT before the combining.

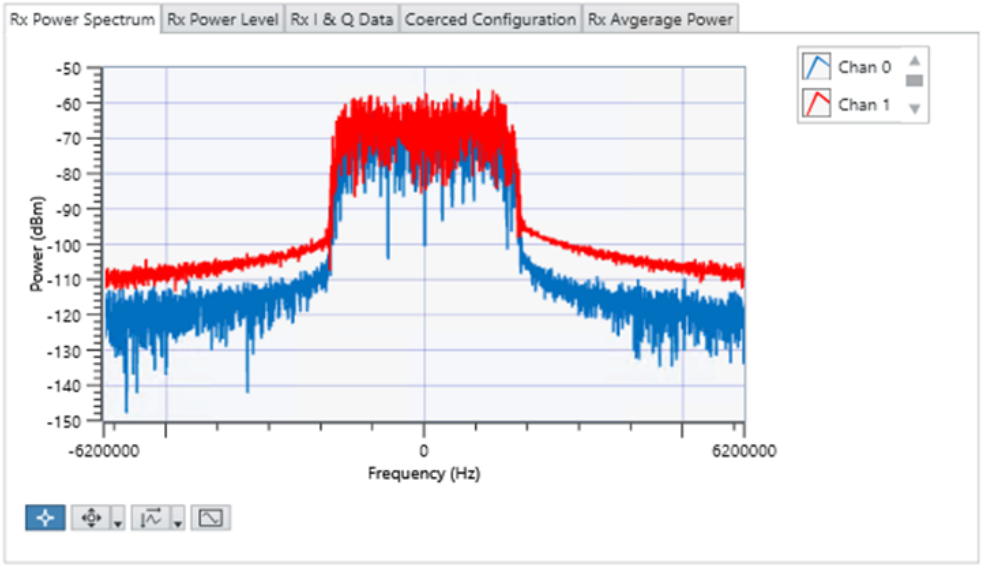

Figure 4.5: Spectrum of the 2 transmitted signals (view for the channel emulator terminal).

Table 4.1: Communication Link Parameters

Waveform	DVB-S2X format 2
Transmitted Signals	2
Walsh-Hadamard indices	5 and 13
Modulation Scheme	QPSK
Bandwidth	3.1 MHz
Oversampling Factor	4
SRRC Parameters	filter span=80 symbols, roll-off factor=0.2
SNR of individual signals	Variable
Symbols Time Misalignment	Variable, between -0.5 and 0.5 (-2 to 2 samples)
Uplink carrier frequency (gateway to channel emulator)	1.13 GHz
Downlink carrier frequency (channel emulator to UT)	1.376 GHz

4.4 Hardware-Software Partitioning at the UT

To implement the (2×1) diversity processing from Fig. 3.2 at the receiver, a hybrid design approach is adopted, integrating both software and hardware components, as illustrated in Fig. 4.6. The most time-critical operation, combining the incoming symbols using FIR filter banks, was implemented in hardware (Fig. 4.7). In contrast, the solution matrices ((3.14a) and (3.14b)) do not require updates at every symbol period, it only needs to adapt quickly enough to track variations in the propagation channel. Therefore, Algorithm 1, which generates the filter coefficients, was implemented in software. This approach also enables the use of floating-point arithmetic during the pseudo-inverse computation, thereby avoiding quantization errors associated with fixed-point representations.

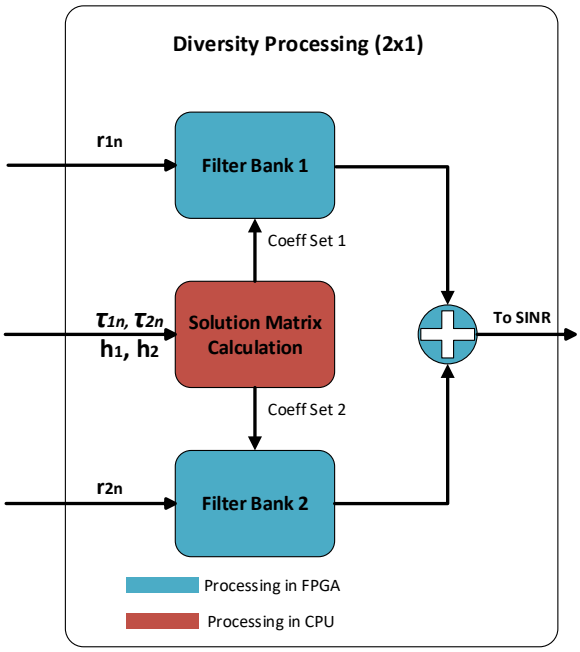

Figure 4.6: Internal structure of the 2×1 diversity processing block in Fig. 3.2. The channel coefficients and time misalignment estimation are sent to an embedded processor, which generates the solution matrices. This processor later updates the filter coefficients in the hardware.

Algorithm 1 Filters coefficients generation using DFT approach.

1: Set $\tau_n \Leftarrow (\tau_{1n} - \tau_{2n})$.
2: Set $\boldsymbol{G} \Leftarrow SRRC(\tau_n)$.
3: Form $\boldsymbol{H}$ using (3.8).
4: Form $\boldsymbol{\Psi}$ using (3.13a) or (3.13b).
5: Set $\boldsymbol{\varphi}^{(n)} \Leftarrow FFT(\boldsymbol{\varphi}_k)$.
6: **for** $n = 1, 2, \ldots, K$ **do**
7: Set $\gamma^{(n)} \Leftarrow \left(\left(\boldsymbol{\varphi}^{(n)}\right)^H \boldsymbol{\varphi}^{(n)} \right)^{-1} \left(\boldsymbol{\varphi}^{(n)}\right)^H$.
8: Set $\boldsymbol{\xi}_k \Leftarrow IFFT(\gamma^{(n)})$.
9: Update filters coeffs with $\boldsymbol{\xi}_k$.

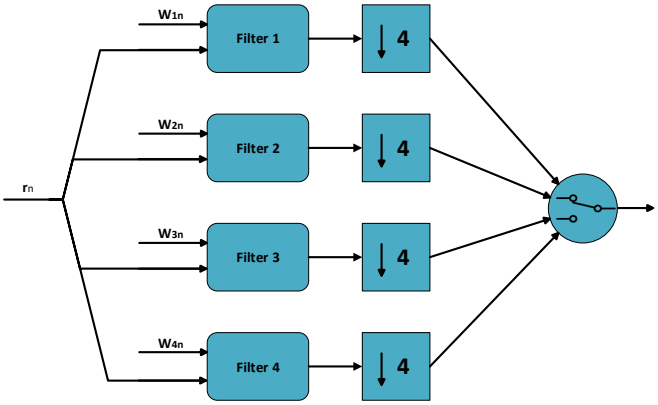

Figure 4.7: FIR filter bank used to perform linear convolution between the incoming symbols (is stack representation as in (3.6)) and the first four rows of the corresponding solution matrix.

Once the coefficients are generated, the filters are updated with the first four rows of the solution matrix. Each $\boldsymbol{\xi}_k$ block in (3.22) is a real matrix of 4×4, hence the total number of coefficients will be $4 \times 4 \times K$. The output of each filter is downsampled by a factor of 4, and then a selector switches continuously from the output of each downsampler.

4.5 Numerical Results

Fig. 4.8, 4.9, 4.10 and 4.11 show the received (STBC encoded) symbols constellations plots at the end of each synchronization chain before and after combining.

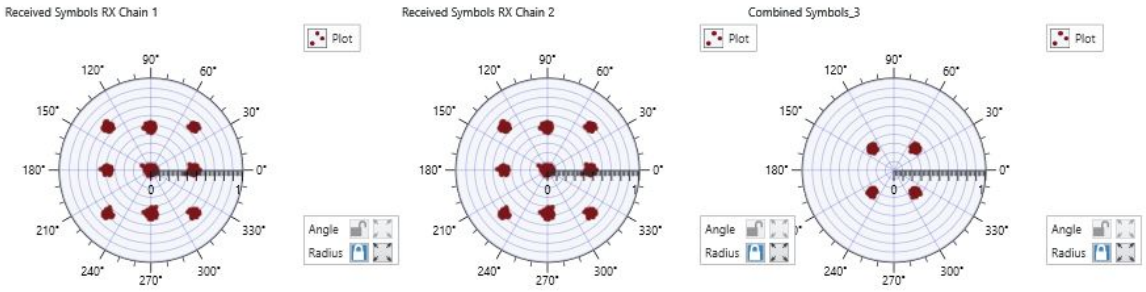

Figure 4.8: Received and combined symbols for 0 symbol time misalignment and 23.14 dB of SINR (The single satellite SNR is of 20 dB).

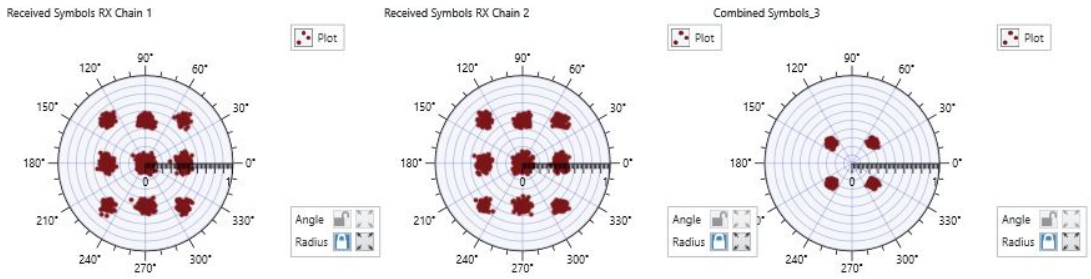

Figure 4.9: Received and combined symbols for 0.125 symbol time misalignment and 23.001 dB of SINR (The single satellite SNR is of 20 dB).

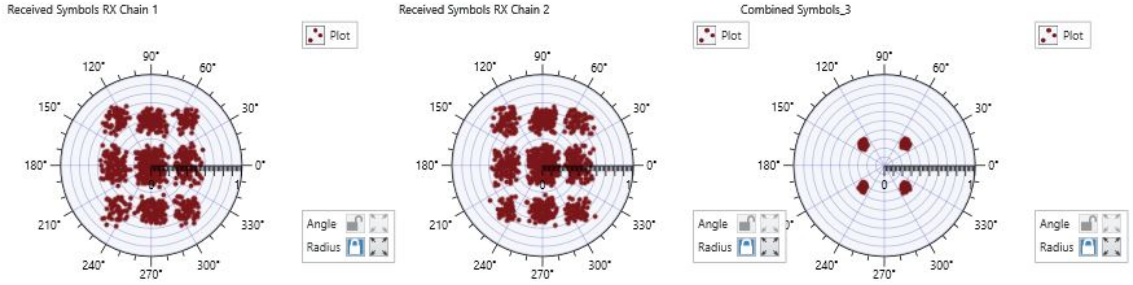

Figure 4.10: Received and combined symbols for 0.25 symbol time misalignment and 22.588 dB of SINR (The single satellite SNR is of 20 dB).

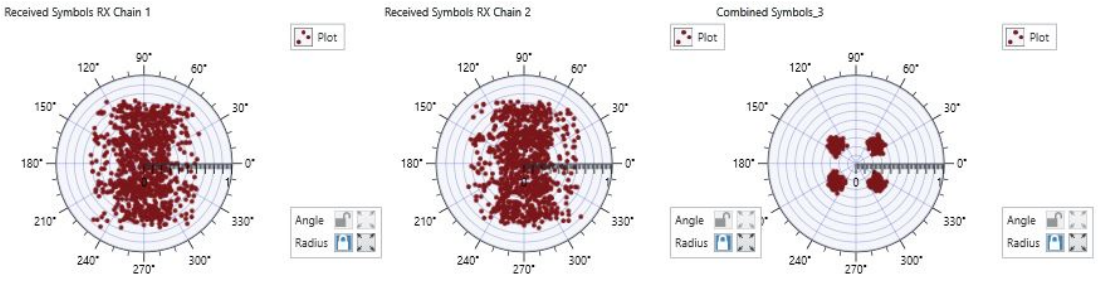

Figure 4.11: Received and combined symbols for 0.5 symbol time misalignment and 20.562 dB of SINR (The single satellite SNR is of 20 dB).

The effect of the ISI introduced by the SRRC filter is quite noticeable as the symbol time misalignment increases from 0 to 0.5 symbols. Nevertheless, the combining block still manages to recover the original symbols.

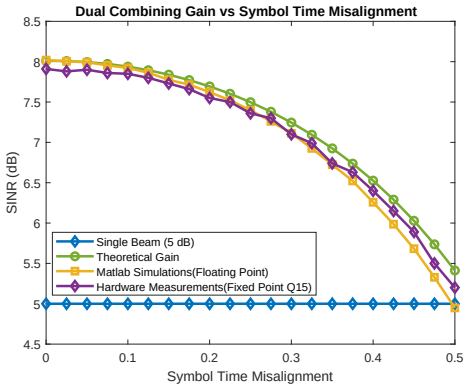

(a) Individual SNR=5 dB

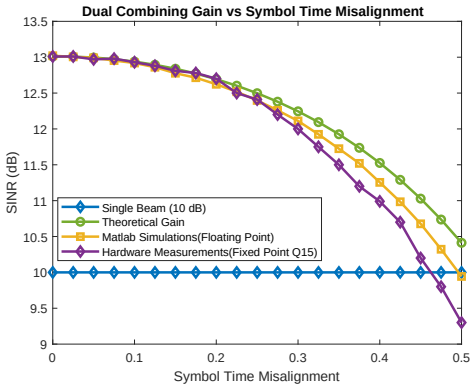

(b) Individual SNR=10 dB

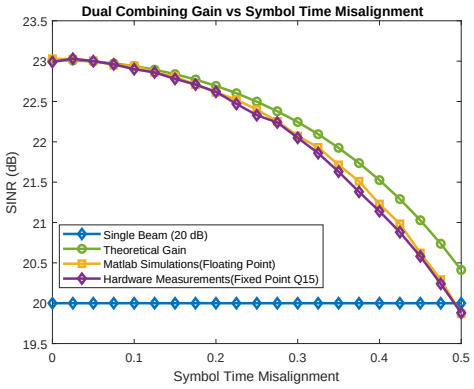

(c) Individual SNR=20 dB

Figure 4.12: Comparison of SINR measurements from hardware, simulation, and theoretical results when combining two signals with equal power.

Fig. 4.12 shows the results of the SINR measurements in hardware for the three individual SNR regimes studied so far, while Fig. 4.13 shows the SINR measurements in hardware when a power imbalance is introduced between the signals.

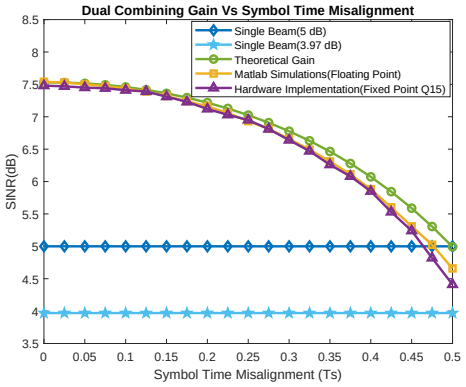

(a) Individual SNRs of 5 and 3.97 dB

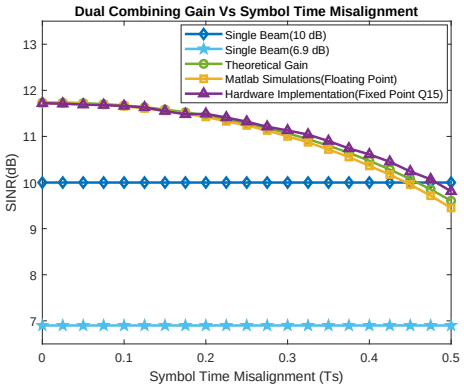

(b) Individual SNRs of 10 and 6.9 dB

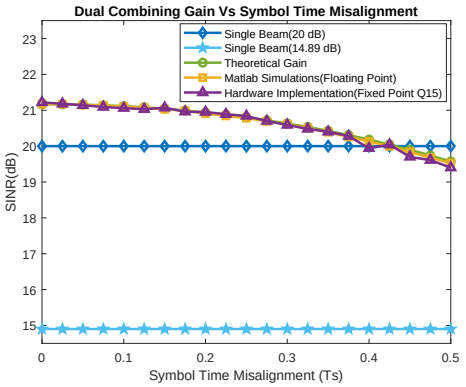

(c) Individual SNRs of 20 and 14.9 dB

Figure 4.13: Comparison of SINR measurements from hardware, simulation, and theoretical results when combining two signals with unequal power.

All experiments were conducted using the communication-link parameters listed in Table 4.1. As observed from the results, the simulation and hardware measurements exhibit only minor discrepancies. In both equal-amplitude and unequal-amplitude signal-combination scenarios, the outcomes remain closely aligned, demonstrating strong agreement between the simulated and experimental setups.

Another critical aspect of our design is the analysis of the combining filters length. Filters with too few taps fail to adequately compensate for the ISI introduced by the SRRC filter, while excessively long filters increase computational complexity without significant performance gains. An upper bound for the filter length can be defined based on the symbol span of the SRRC filter, which in our case is 80 symbols. To determine a suitable lower bound, we conducted experiments analyzing the SINR gain as a function of the number of taps in the filter bank, under varying conditions of symbol time misalignment and individual SNR.

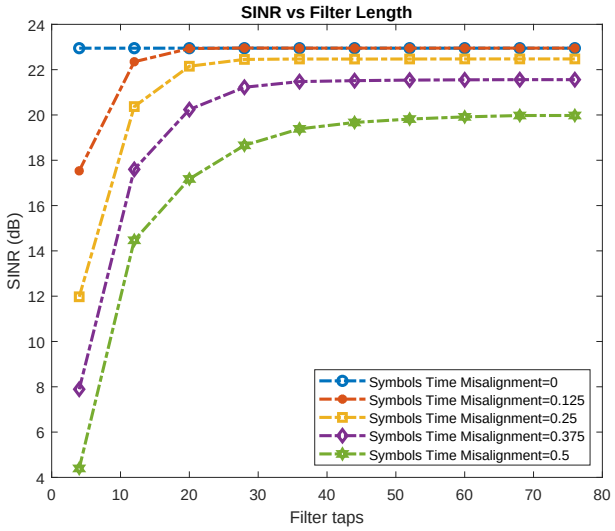

Figure 4.14: SINR gain vs filter length when combining two signals with 20 dB of SNR each.

For the scenario more susceptible to ISI, the one with individual signal SNRs of 20 dB, Fig. 4.14 shows that lower time misalignments between signals require fewer filter taps to effectively compensate for ISI. Moreover, beyond 60 taps, the SINR gain saturates, even in the worst-case misalignment of 0.5 symbol time.

Since the receiver is fully implemented in an embedded system, computational resources are limited. Therefore, each arithmetic operation must be carefully examined to ensure efficiency. Given the division between software and hardware components, it is appropriate to conduct separate analyses: one for the floating-point operations executed in software, and another for the fixed-point operations carried out in hardware.

The proposed Algorithm 1 introduces considerable computational complexity. It involves multiple matrix multiplications, both real and complex, with a complexity of $\mathcal{O}(N^3)$, as well as K 4×4 complex matrix inversion using either Lower-Upper decomposition or Gauss-Jordan elimination, which also has a complexity of $\mathcal{O}(N^3)$. Additionally, the algorithm performs several Fast Fourier Transform (FFT) computations using the radix-2 algorithm, requiring $\mathcal{O}(\frac{K}{2} log_2(K))$ complex multiplications and $\mathcal{O}(K log_2(K))$ complex additions [86].

Table 4.2: Floating Point Operations in Algorithm 1 (for an individual Rx chain)

Operation	**Description**	**Complexity (Real Flops)**
Computing τ_n	One real substraction	$\mathcal{O}(1)$
Computing $\boldsymbol{G}$	Pre-computed values	-
Form $\boldsymbol{H}$ using (Eq. 3.8)	Read values from FPGA	-
Form $\boldsymbol{\Psi_{1,2}}$ using (3.13a) and (3.13b)	One 4×4 real matrix multiplication, One $N \times N$ real matrix multiplication and one $N \times N$ real matrix addition	$\mathcal{O}(4^3)+\mathcal{O}(N^3)+\mathcal{O}(N^2)$
Compute FFT	Perform 16 FFT of K samples each (where φ_K is composed by K (4×4) matrices)	$16[\mathcal{O}(4(\frac{K}{2})log_2(K)) + \mathcal{O}(2(Klog_2(K) + (\frac{K}{2})log_2(K))]$
Compute Pseudo-Inverse of K 4×4 complex matrices	Each complex pseudo inverse requires 2 (4×4) complex matrix multiplication and one 4×4 complex matrix inversion	$\mathcal{O}(2(480)) + \mathcal{O}(856)$
Compute IFFT	Perform 16 IFFT of K samples each (where $\gamma^{(n)}$ is composed by K (4×4) matrices)	$16[\mathcal{O}(4(\frac{K}{2})log_2(K)) + \mathcal{O}(2(Klog_2(K) + (\frac{K}{2})log_2(K))]$

Table 4.2 presents a comprehensive breakdown of the computational complexity involved in calculating the filters coefficients. All complex operations are represented by their equivalent number of real floating-point operations to provide a uniform and precise comparison.

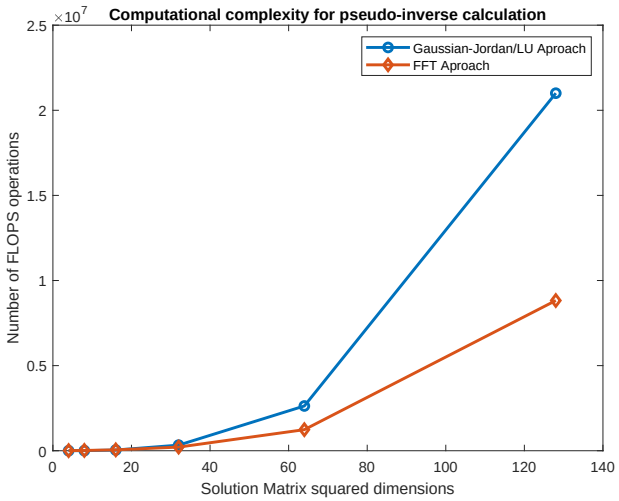

Figure 4.15: Computational complexity using classical matrix inversion methods vs using our proposed method.

Fig. 4.15 compares the overall computational complexity of calculating the pseudo inverse in (3.14a) and (3.14b), using the proposed Algorithm 1, against conventional matrix inversion techniques such as Lower-Upper decomposition and Gauss-Jordan elimination. All matrix sizes are powers of two, in accordance with the radix-2 FFT algorithm requirements. The results indicate that for smaller matrices, the computational complexities are comparable. However, as the matrix size increases, the proposed method demonstrates a notable efficiency gain, requiring less than half the number of floating-point operations for a 64×64 matrix and nearly 2.7 times fewer operations for a 128×128 matrix.

In contrast, hardware complexity analysis is more straightforward. According to digital filter theory, the number of multiplications in an N-tap FIR filter scales with $\mathcal{O}(N)$, and the number of additions scales with $\mathcal{O}(N-1)$ [87]. Fig. 4.16 illustrates the total number of fixed-point operations per symbol, accounting for both filter banks required to merge the two data streams as a function of the filter length. While Fig. 4.17 shows the total amount of FPGA resources employed in the design of the UT.

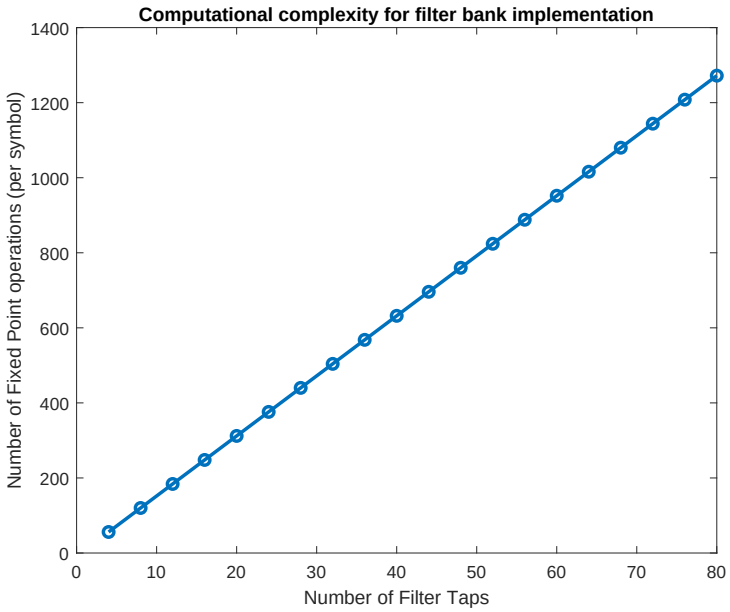

Figure 4.16: Computational complexity of the two filter banks used in the combining process.

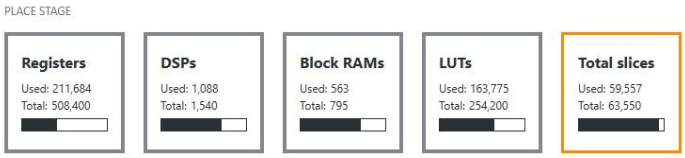

Figure 4.17: Total FPGA resources employed by the UT

4.6 Conclusions

In this chapter, a real-time hardware validation of the methods and simulations introduced in Chapter 3 was presented. A complete testbed environment comprising the GW, channel emulator, and user terminal UT was deployed to enable a realistic end-to-end assessment of system performance, covering the entire chain from signal encoding to channel impairments, real-time combining, and SINR estimation. The experimental results confirm that the proposed system enhances transmission reliability by effectively combining two STBC-encoded signals, even under practical impairments such as symbol timing misalignment, AWGN and power imbalance.

Chapter 5

Conclusions and Future Work

5.1 Conclusion

This thesis investigated the feasibility of exploiting path diversity from multiple satellites at the UT in NTNs under realistic operational conditions. The central premise of this work was that future NGSO constellations will increasingly provide simultaneous visibility of multiple satellites, creating opportunities for cooperative transmission and spatial diversity. However, the practical realization of these gains is fundamentally challenged by differential propagation delays, clock mismatches, Doppler effects, and the lack of perfect synchronization among distributed transmitters.

The first research question asked whether diversity combining techniques for signals received from satellite constellations can be implemented at the UT under realistic channel conditions. The results obtained throughout this thesis provide a positive answer. It was shown that conventional STBC receivers experience substantial performance degradation when symbol-time misalignment exists between the received waveforms, a condition that is unavoidable in practical multi-satellite systems. To address this limitation, a novel UT-assisted diversity combining architecture was developed that explicitly incorporates symbol-time misalignment into the combining process. Both simulation results and real-time hardware experiments demonstrated that meaningful diversity gains can be preserved despite asynchronous waveform arrivals. The close agreement between theoretical analysis, software simulations, and hardware measurements confirms that diversity combining from geographically distributed satellites is not only theoretically possible but also practically realizable.

The second research question concerned the computational feasibility of implementing

such combining techniques at the UT. The proposed receiver architecture addressed this challenge through the exploitation of block-circulant matrix structures and Fourier-domain processing. These mathematical properties enabled the development of a low-complexity implementation that significantly reduced the computational burden associated with conventional matrix inversion methods. The FPGA implementation and complexity analysis demonstrated that the receiver can operate within realistic processing constraints while maintaining performance comparable to more computationally demanding approaches. Therefore, the thesis establishes that diversity combining under symbol-time misalignment can be achieved with a complexity level compatible with practical user-terminal implementations.

The third research question focused on quantifying the effects of imperfect CSI and other estimation errors on diversity-combining performance. The analysis showed that symbol-time misalignment, Doppler shifts, power imbalance, and CSI estimation errors all contribute to performance degradation. However, the resulting degradation remained bounded and predictable. In particular, the proposed combining architecture maintained stable SINR gains across a wide range of operating conditions and exhibited significantly greater robustness than conventional Alamouti receivers. Even under imperfect synchronization and channel estimation, the achievable performance remained sufficiently attractive to justify practical deployment. These results demonstrate that the proposed techniques are resilient to the types of impairments expected in realistic NGSO satellite environments.

The fourth research question investigated how fast-varying timing conditions between satellites and the UT can be estimated and tracked. To answer this question, this thesis introduced a comprehensive modeling framework that captures waveform misalignment arising from orbital dynamics, propagation-delay variations, and clock imperfections. Building upon this framework, a dual-stage estimation architecture was developed, combining coarse frame-level synchronization with fine symbol-time tracking based on delay-locked loops and Kalman filtering. The results demonstrated that the proposed approach accurately estimates and tracks differential timing variations even under realistic phase-noise and feedback-delay conditions. Furthermore, the introduction of a distributed compensation loop between the UT and the satellite payloads enabled the reduction of timing offsets from thousands of samples to a level compatible with practical diversity combining. These findings demonstrate that waveform-level alignment can be effectively achieved in distributed multi-satellite systems without requiring unrealistically strict synchronization assumptions.

The fifth research question examined the benefits of UT-based diversity combining relative to fully CSI-aware gateway precoding and distributed beamforming approaches. The results suggest that UT-based diversity combining offers a compelling alternative in environments characterized by asynchronous transmissions, limited coordination, rapidly varying channels, and scalability constraints. Unlike gateway-centric approaches, the proposed solution does not require global CSI acquisition or stringent synchronization among transmitting satellites. Instead, it transfers the adaptation process to the receiver, where local measurements can be exploited directly. The demonstrated robustness to timing misalignment and practical implementation feasibility indicate that UT-based diversity combining represents a scalable and resilient architecture for future large-scale satellite constellations.

Beyond answering the individual research questions, this thesis provides a broader contribution to the development of cooperative satellite communications. The results challenge the conventional assumption that effective transmit diversity requires near-perfect synchronization among distributed transmitters. Instead, the findings demonstrate that practical diversity gains can be recovered through intelligent receiver processing combined with moderate transmitter-side timing compensation. This significantly relaxes the synchronization requirements traditionally associated with cooperative satellite transmission and opens a realistic path toward the deployment of diversity-enabled NTN architectures.

In summary, this thesis establishes that cooperative multi-satellite reception with path diversity is feasible, computationally practical, robust to realistic impairments, and implementable in real hardware. The proposed synchronization, compensation, and combining techniques collectively provide a scalable framework for exploiting the spatial diversity inherently available in future satellite constellations. As a result, this work advances the state of the art in cooperative satellite communications and contributes enabling technologies for resilient, high-capacity, and synchronization-tolerant non-terrestrial networks.

5.2 Future Work

While this thesis focused primarily on dual-satellite cooperation, an important extension of the proposed framework involves generalization to scenarios with more than two cooperating satellites. Multi-node diversity combining raises new challenges related to synchronization scalability, channel estimation accuracy, and computational complexity, but also offers the

potential for increased diversity and robustness in dense constellations. Another promising direction concerns the joint treatment of symbol-time, carrier-frequency, and phase alignment within a unified estimation and compensation framework. Although this thesis deliberately separated time-alignment and phase-tracking processes, tighter integration may yield further gains under highly dynamic conditions. Learning-based or adaptive filtering techniques could also be explored to enhance robustness in rapidly time-varying environments.

Future work may additionally investigate the extension of the proposed combining techniques to alternative waveforms and access schemes, such as OFDM-based systems used in 5G NR non-terrestrial networks. The interaction between time misalignment, cyclic prefixes, and multi-carrier structures presents new opportunities and challenges for diversity combining. Finally, incorporating additional hardware impairments—such as nonlinear amplification, quantization effects, and burst-mode operation would further strengthen the applicability of the proposed methods to operational systems. Combined with system-level evaluations involving higher-layer protocols and scheduling strategies, such investigations would help bridge the gap between physical-layer innovation and end-to-end NTN performance.

Appendix A

SCRAMBLER EFFECT ON THE INTER-SYMBOL INTERFERENCE

Suppose we want to transmit a vector of complex symbols $\boldsymbol{x} \in \mathbb{C}$. On the GW side, the symbols are first encoded by a generic encoding matrix $\mathbf{E}$ and then scrambled by a scrambling vector $\boldsymbol{s}$, before going through the transmission filter. On the UT side the received symbols can be expressed as

$$\mathbf{r} = \text{diag}\,(\boldsymbol{d})\boldsymbol{G}h\,\text{diag}\,(\boldsymbol{s})\boldsymbol{E}\boldsymbol{x}, \tag{A.1}$$

where h is a scalar representing the channel CSI that remains constant for the duration of the symbol's transmission, $\boldsymbol{G}$ is the ISI introduced by the SRRC filter due to improper time synchronization, and $\boldsymbol{d}$ is the descrambler sequence applied to the incoming symbols, and has the property $\text{diag}(\boldsymbol{d})\,\text{diag}(\boldsymbol{s}) = I$. If we wish to recover the transmitted symbols using the approach proposed in (3.14a) and (3.14b) based on the estimation of h and $\boldsymbol{G}$, we can write

$$\begin{aligned}\tilde{\mathbf{x}} = &\Big[((\boldsymbol{G}h\boldsymbol{E})^H(\boldsymbol{G}h\boldsymbol{E}))^{-1}(\boldsymbol{G}h\boldsymbol{E})^H\Big] \\ &\times \Big[\text{diag}\,(\boldsymbol{d})\boldsymbol{G}(\,\text{diag}\,(\boldsymbol{s})h\boldsymbol{E}\boldsymbol{x})\Big].\end{aligned} \tag{A.2}$$

if $\boldsymbol{G} = \boldsymbol{I}$ then (A.2) transforms into:

$$\tilde{\mathbf{x}} = \Big[((h\boldsymbol{E})^H(h\boldsymbol{E}))^{-1}(h\boldsymbol{E})^H\Big]h\boldsymbol{E}\boldsymbol{x}. \tag{A.3}$$

Then the transmitted symbols can be recovered appropriately, otherwise if a scrambler sequence is used while the signal is affected by improper time synchronization (like the overlapped signals in (3.9a) and (3.9b)), the ISI distortion compensated is not the same as the one introduced by the SRRC filter.

Bibliography

[1] E. Lagunas, S. Chatzinotas, and B. Ottersten, "Low-earth orbit satellite constellations for global communication network connectivity," *Nature Reviews Electrical Engineering*, vol. 1, pp. 656–665, 2024.

[2] C. Westphal, L. Han, and R. Li, "Leo satellite networking relaunched: Survey and current research challenges," *ITU Journal on Future and Evolving Technologies*, vol. 4, no. 4, pp. 711–744, 2023.

[3] IEEE Communications Society, "Best readings in satellite mega-constellations," 2024, available online. [Online]. Available: https://www.comsoc.org/publications/best-readings/satellite-mega-constellations

[4] W. L. Pritchard, H. Suyderhoud, and R. A. Nelson, *Satellite Communication Systems Engineering*. Prentice Hall, 1993.

[5] I. Ali, P. G. Bonanni, N. Al-Dhahir, and J. E. Hershey, *Doppler Applications in LEO Satellite Communication Systems*, ser. The Springer International Series in Engineering and Computer Science. Kluwer Academic Publishers, 2002, vol. 656.

[6] M. Krondorf, "Initial synchronization procedure and doppler pre-compensation for leo-satcom terminals," *Telecom*, vol. 6, no. 4, 2025. [Online]. Available: https://www.mdpi.com/2673-4001/6/4/81

[7] D. Gesbert, S. Hanly, H. Huang, S. Shamai Shitz, O. Simeone, and W. Yu, "Multi-cell mimo cooperative networks: A new look at interference," *IEEE Journal on Selected Areas in Communications*, vol. 28, no. 9, pp. 1380–1408, 2010.

[8] Y. Sun, R. Li, Z. Song, R. Li, S. Zhang, and M. Peng, "Performance analysis of leo multi-satellite cooperative transmission based on stochastic geometry," in *Proceedings of the*

2nd International Conference on Networks, Communications and Intelligent Computing (NCIC 2024), Z. Yang and G. Sun, Eds. Singapore: Springer Nature Singapore, 2025, pp. 53–65.

[9] X. Zhang, S. Sun, M. Tao, Q. Huang, and X. Tang, "Multi-satellite cooperative networks: Joint hybrid beamforming and user scheduling design," *IEEE Transactions on Wireless Communications*, vol. 23, no. 7, pp. 7938–7952, 2024.

[10] A. B. De F. Diniz, T. Eriksson, and U. Gustavsson, "Doppler shift estimation for satellite communications using linear estimators," in *2024 IEEE 25th International Workshop on Signal Processing Advances in Wireless Communications (SPAWC)*, 2024, pp. 686–690.

[11] F. Kunzi and O. Montenbruck, "Precise onboard time synchronization for leo satellites," *NAVIGATION: Journal of the Institute of Navigation*, vol. 69, no. 3, 2022. [Online]. Available: https://navi.ion.org/content/69/3/navi.531

[12] H. Al-Hraishawi, H. Chougrani, S. Kisseleff, E. Lagunas, and S. Chatzinotas, "A survey on nongeostationary satellite systems: The communication perspective," *IEEE Communications Surveys & Tutorials*, vol. 25, no. 1, pp. 101–132, 2023.

[13] Y. Liu, F. Yao, and S. Yu, "Study on diversity methods in mobile satellite communication systems," in *2009 International Conference on Wireless Communications & Signal Processing*, 2009, pp. 1–4.

[14] Q. Zhang, L. Xu, J. Huang, T. Yang, J. Jiao, Y. Wang, Y. Shi, C. Zhang, X. Zhang, K. Zhang, Y. Gong, N. Deng, N. Zhao, Z. Gao, S. Wang, S. Han, X. Xu, L. You, D. Wang, S. Jiang, D. Zhao, N. Zhang, L. Hu, X. He, Y. Li, X. Gao, and X. You, "Distributed satellite information networks: architecture, enabling technologies, and trends," *Science China. Information sciences*, vol. 68, no. 9, pp. 190 301–, 2025.

[15] X. Lu and J. Xu, "Novel multi-satellite transmit diversity schemes," in *Second International Conference on Space Information Technology*, C. Wang, S. Zhong, and J. Wei, Eds., vol. 6795, International Society for Optics and Photonics. SPIE, 2007, p. 67950R. [Online]. Available: https://doi.org/10.1117/12.772928

[16] A. Gharanjik, B. Shankar M. R., P.-D. Arapoglou, and B. Ottersten, "Multiple gateway transmit diversity in q/v band feeder links," *IEEE Transactions on Communications*, vol. 63, no. 3, pp. 916–926, 2015.

[17] V. Singh, G. Eappen, W. A. Martins, R. Palisetty, C. L. M. Rojas, J. L. Gonzalez-Rios, J. A. Vásquez-Peralvo, J. Krivochiza, J. C. Merlano-Duncan, L. G. Socarras, S. Chatzinotas, and B. Ottersten, "Diversity combining scheme for time-varying stbc ngso multi-satellite systems," *IEEE Communications Letters*, vol. 28, no. 4, pp. 882–886, 2024.

[18] "IRIS: the new EU Secure Satellite Constellation." [Online]. Available: https://defence-industry-space.ec.europa.eu/eu-space/iris2-secure-connectivity_en

[19] A. Modenini, A. Ugolini, A. Piemontese, and G. Colavolpe, "On the use of multiple satellites to improve the spectral efficiency of broadcast transmissions," *IEEE Transactions on Broadcasting*, vol. 61, no. 4, pp. 590–602, Dec. 2015.

[20] S. Alamouti, "A simple transmit diversity technique for wireless communications," *IEEE Journal on Selected Areas in Communications*, vol. 16, no. 8, pp. 1451–1458, 1998.

[21] D. Gesbert, M. Shafi, D. shan Shiu, P. Smith, and A. Naguib, "From theory to practice: an overview of mimo space-time coded wireless systems," *IEEE Journal on Selected Areas in Communications*, vol. 21, no. 3, pp. 281–302, 2003.

[22] A. Roy and R. Roy, "Reliability benefit of network coding and cooperative communication," *Physical Communication*, vol. 29, pp. 217–229, 2018. [Online]. Available: https://www.sciencedirect.com/science/article/pii/S1874490717306250

[23] M. Sellathurai, P. Guinand, and J. Lodge, "Space-time coding in mobile satellite communications using dual-polarized channels," *IEEE Transactions on Vehicular Technology*, vol. 55, no. 1, pp. 188–199, Jan. 2006.

[24] Y. Dhungana, N. Rajatheva, and C. Tellambura, "Dual hop MIMO OSTBC for LMS communication," *IEEE Wireless Communications Letters*, vol. 1, no. 2, pp. 105–108, Apr. 2012.

[25] A. M. K. and S. K. Jindal, "Ostbc transmission in shadowed-rician land mobile satellite links," *IEEE Transactions on Vehicular Technology*, vol. 65, no. 7, pp. 5771–5777, 2016.

[26] E. A. Kaban, W. Pamungkas, and A. F. Isnawati, "Mimo-ofdm 2x2 stbc alamouti simulation analysis," in *2024 IEEE International Conference on Communication, Networks and Satellite (COMNETSAT)*, 2024, pp. 602–608.

[27] R. He and Z. Shen, "System design and performance of ship-borne satellite high-speed data reliable transportation based on coded stbc-ofdm," in *2022 7th International Conference on Intelligent Computing and Signal Processing (ICSP)*, 2022, pp. 1302–1306.

[28] C. Wang, X. Zhuo, Y. Hu, W. Wu, L. Tang, Y. Zhao, F. Qu, and Z. Bu, "Performance analysis of satellite–terrestrial communication network with inter-satellite cooperative relay protocol," *IEEE Internet of Things Journal*, vol. 13, no. 3, pp. 3661–3675, 2026.

[29] M. Toka, M. Vaezi, and W. Shin, "Outage analysis of alamouti-noma scheme for hybrid satellite–terrestrial relay networks," *IEEE Internet of Things Journal*, vol. 10, no. 6, pp. 5293–5303, 2023.

[30] H. Lee and S. Kim, "Space-time block code based cooperative physical layer security schemes for leo satellite systems," in *2023 14th International Conference on Information and Communication Technology Convergence (ICTC)*, 2023, pp. 554–557.

[31] C. L. M. Rojas, R. Palisetty, J. Krivochiza, J. L. G. Rios, L. M. Marrero, W. A. Martins, J. C. M. Duncan, and S. Chatzinotas, "Time-misalignment estimation in overlapped dvb-s2x waveforms," in *2024 IEEE Wireless Communications and Networking Conference (WCNC)*, 2024, pp. 1–6.

[32] L. M. Marrero, J. C. Merlano-Duncan, J. Querol, S. Kumar, J. Krivochiza, S. K. Sharma, S. Chatzinotas, A. Camps, and B. Ottersten, "Architectures and synchronization techniques for distributed satellite systems: A survey," *IEEE Access*, vol. 10, pp. 45 375–45 409, 2022.

[33] J. L. González-Rios, L. Martínez-Marrero, E. Lagunas, J. Krivochiza, L. M. Garcés-Socarrás, R. Palisetty, J. M. Duncan, and S. Chatzinotas, "Doppler shift in precoded cooperative multi-gateway satellite systems: Effects and mitigation," in *2024 IEEE Wireless Communications and Networking Conference (WCNC)*, 2024, pp. 1–6.

[34] O. Kodheli, E. Lagunas, N. Maturo, S. K. Sharma, B. Shankar, J. F. M. Montoya, J. C. M. Duncan, D. Spano, S. Chatzinotas, S. Kisseleff, J. Querol, L. Lei, T. X. Vu,

and G. Goussetis, "Satellite communications in the new space era: A survey and future challenges," *IEEE Communications Surveys & Tutorials*, vol. 23, no. 1, pp. 70–109, 2021.

[35] R. Mudumbai, D. R. Brown Iii, U. Madhow, and H. V. Poor, "Distributed transmit beamforming: challenges and recent progress," *IEEE Communications Magazine*, vol. 47, no. 2, pp. 102–110, Feb. 2009.

[36] M. A. Vazquez, A. Perez-Neira, D. Christopoulos, S. Chatzinotas, B. Ottersten, P.-D. Arapoglou, A. Ginesi, and G. Taricco, "Precoding in multibeam satellite communications: Present and future challenges," *IEEE Wireless Communications*, vol. 23, no. 6, pp. 88–95, Dec. 2016.

[37] M. Doostmohammadian and T. Charalambous, "Distributed target tracking based on localization with linear time-difference-of-arrival measurements: A delay-tolerant networked estimation approach," *Systems & Control Letters*, vol. 196, p. 106009, 2025. [Online]. Available: https://www.sciencedirect.com/science/article/pii/S0167691124002974

[38] O. Ennasr and X. Tan, "Time-difference-of-arrival (tdoa)-based distributed target localization by a robotic network," *IEEE Transactions on Control of Network Systems*, vol. 7, no. 3, pp. 1416–1427, 2020.

[39] M. Liu, F. Yi, P. Liu, and B. Li, "Cramer-rao lower bounds of tdoa and fdoa estimation based on satellite signals," in *2018 14th IEEE International Conference on Signal Processing (ICSP)*, 2018, pp. 654–657.

[40] M. Maróti, B. Kusy, G. Simon, and A. Lédeczi, "The flooding time synchronization protocol," in *Proceedings of the 2nd International Conference on Embedded Networked Sensor Systems*, ser. SenSys '04. New York, NY, USA: Association for Computing Machinery, 2004, p. 39–49. [Online]. Available: https://doi.org/10.1145/1031495.1031501

[41] S. Rucksana, C. Babu, and S. Saranyabharathi, "Efficient timing-sync protocol in wireless sensor network," in *2015 International Conference on Innovations in Information, Embedded and Communication Systems (ICIIECS)*, 2015, pp. 1–5.

[42] A. Berger, M. Pichler, J. Klinglmayr, A. Pötsch, and A. Springer, "Low-complex synchronization algorithms for embedded wireless sensor networks," *IEEE Transactions on Instrumentation and Measurement*, vol. 64, no. 4, pp. 1032–1042, 2015.

[43] S.-M. M. Yang, *Modern Digital Radio Communication Signals and Systems*, 2nd ed. Springer, 2020.

[44] F. Kunzi and O. Montenbruck, "Precise onboard time synchronization for leo satellites," *NAVIGATION: Journal of the Institute of Navigation*, vol. 69, no. 3, 2022. [Online]. Available: https://navi.ion.org/content/69/3/navi.531

[45] X. Chen and Z. Luo, "Asynchronous interference mitigation for leo multi-satellite cooperative systems," *IEEE Transactions on Wireless Communications*, vol. 23, no. 10, pp. 14 956–14 971, 2024.

[46] M. Caus, M. Shaat, A. I. Pèrez-Neira, M. Schellmann, and H. Cao, "Cooperative dual leo satellite transmission in multi-user otfs systems," in *2023 IEEE International Conference on Acoustics, Speech, and Signal Processing Workshops (ICASSPW)*, 2023, pp. 1–5.

[47] J. Qu, H. Shi, N. Qiao, C. Wu, C. Su, and A. Razi, "New three-dimensional positioning algorithm through integrating tdoa and newton's method," *EURASIP Journal on Wireless Communications and Networking*, vol. 2020, no. 77, 2020. [Online]. Available: https://link.springer.com/article/10.1186/s13638-020-01684-7

[48] W. Song, D. Yan, C. Shi, F. Zheng, C. Wu, G. Jing, Y. Wang, and X. Meng, "Bds/gps tens of picoseconds time synchronization method with application to communication network," *IEEE Internet of Things Journal*, vol. 12, no. 11, pp. 17 244–17 262, 2025.

[49] W.-Y. Yeo and D.-J. Lee, "Uplink time synchronization based on time drift measurements in non-terrestrial networks," *IEEE Access*, vol. 12, pp. 168 877–168 893, 2024.

[50] Y. Shao and Y. Liu, "Single-symbol iteration based delay-locked loop for 5g nr positioning," in *2023 IEEE 23rd International Conference on Communication Technology (ICCT)*, 2023, pp. 1–5.

[51] W. Wang, Y. Tong, L. Li, A.-A. Lu, L. You, and X. Gao, "Near optimal timing and frequency offset estimation for 5g integrated leo satellite communication system," *IEEE Access*, vol. 7, pp. 113 298–113 310, 2019.

[52] K. Wang, Y. Ma, S. Liu, J. Loo, W. Lin, Z. Deng, and J. Li, "Sampling frequency offset analysis and compensation for ofdm-based leo satellite communication system," *IEEE Transactions on Communications*, vol. 73, no. 9, pp. 8362–8376, 2025.

[53] Z. Zhang, Y. Wu, Z. Ma, X. Lei, L. Lei, and Z. Wei, "Coordinated multi-satellite transmission for otfs-based 6g leo satellite communication systems," *IEEE Journal on Selected Areas in Communications*, vol. 43, no. 1, pp. 156–170, 2025.

[54] Z. Yu, X. Chen, Q. Wei, L. Yin, C. Jiang, and T. Q. S. Quek, "Bandwidth-efficient tdoa estimation in generalized differential positioning with ofdm satellite signals of opportunity," *IEEE Transactions on Vehicular Technology*, vol. 74, no. 12, pp. 19 001–19 015, 2025.

[55] S. Daoud, E. Lagunas, J. L. González-Rios, C. L. M. Rojas, and S. Chatzinotas, "Differential delay effect in precoded cooperative multi-gateway satellite systems," in *2025 IEEE 36th International Symposium on Personal, Indoor and Mobile Radio Communications (PIMRC)*, 2025, pp. 1–7.

[56] C. L. Marcos Rojas, J. L. Gonzalez Rios, L. M. Garces Socarras, V. Singh, R. Cuiman Marquez, J. C. Merlano Duncan, V. Nguyen Ha, S. Chatzinotas, and B. Ottersten, "Dual satellite stbc combining under imperfect symbol time alignment," *IEEE Open Journal of the Communications Society*, vol. 7, pp. 301–314, 2026.

[57] S. Jung, P. Kim, J.-Y. Lee, and J. G. Ryu, "Comparative study of potential solutions for satellite iot communications," in *2025 16th International Conference on Information and Communication Technology Convergence (ICTC)*, 2025, pp. 2022–2023.

[58] G. George, S. Roy, S. Raghunandan, C. Rohde, and T. Heyn, "5g new radio in nonlinear satellite downlink: A physical layer comparison with dvb-s2x," in *2021 IEEE 4th 5G World Forum (5GWF)*, 2021, pp. 499–504.

[59] B. Chamaillard, A. Traoré, N. Borios, and S. Cioni, "Physical layer simulative comparison of dvb-s2x/rcs2 and 3gpp 5g nr-ntn technologies over geostationary satellite scenario," in *2025 12th Advanced Satellite Multimedia Systems Conference and the 18th Signal Processing for Space Communications Workshop (ASMS/SPSC)*, 2025, pp. 1–8.

[60] G. Maral, M. Bousquet, and Z. Sun, *Satellite Communications Systems: Systems, Techniques and Technology*, 6th ed. John Wiley & Sons, 2020.

[61] E. A. Likhobabin, A. A. Ovinnikov, R. S. Goriushkin, P. B. Nikishkin, and E. I. Khokhryakov, "High throughput fpga implementation of ldpc decoder architecture for dvb-s2x standard," in *2022 International Conference on Information, Control, and Communication Technologies (ICCT)*, 2022, pp. 1–4.

[62] *Digital Video Broadcasting (DVB): Second Generation Framing Structure, Channel Coding and Modulation Systems for Broadcasting, Interactive Services, News Gathering and Other Broadband Satellite Applications; Part 2: DVB-S2 Extensions (DVB-S2X)*, ETSI Std. EN 302 307-2, 2021.

[63] M. Caus, M. Shaat, A. I. Pèrez-Neira, M. Schellmann, and H. Cao, "Cooperative dual leo satellite transmission in multi-user otfs systems," in *2023 IEEE International Conference on Acoustics, Speech, and Signal Processing Workshops (ICASSPW)*, 2023, pp. 1–5.

[64] M. M. Azari, S. Solanki, S. Chatzinotas, O. Kodheli, H. Sallouha, A. Colpaert, J. F. Mendoza Montoya, S. Pollin, A. Haqiqatnejad, A. Mostaani, E. Lagunas, and B. Ottersten, "Evolution of non-terrestrial networks from 5g to 6g: A survey," *IEEE Communications Surveys & Tutorials*, vol. 24, no. 4, pp. 2633–2672, 2022.

[65] R. Vescovo, "Inversion of block-circulant matrices and circular array approach," *IEEE Transactions on Antennas and Propagation*, vol. 45, no. 10, pp. 1565–1567, 1997.

[66] C. A. Corral, "Inversion of matrices with prescribed structured inverses," in *2002 IEEE International Conference on Acoustics, Speech, and Signal Processing*, vol. 2, 2002, pp. II–1501–II–1504.

[67] "A parallel algorithm for the inversion of matrices with simultaneously diagonalizable blocks," *Computers & Mathematics with Applications*, vol. 174, pp. 340–351, 2024.

[68] S.-M. M. Yang, *Synchronization of Frame, Symbol Timing and Carrier*. Cham: Springer International Publishing, 2020. [Online]. Available: https://doi.org/10.1007/978-3-030-57706-3_7

[69] P. Kim and H. Park, "Robust symbol timing synchronization for initial access under leo satellite channel," *Sensors*, vol. 23, no. 19, 2023. [Online]. Available: https://www.mdpi.com/1424-8220/23/19/8320

[70] Ansys, Inc., "Systems Tool Kit (STK)," Exton, PA, USA, 2023. [Online]. Available: https://www.ansys.com/products/missions/ansys-stk

[71] D. A. Vallado, *Fundamentals of Astrodynamics and Applications*, 4th ed. Hawthorne, CA, USA: Microcosm Press, 2013.

[72] L. B. M. Sagnières and I. Sharf, "Uncertainty characterization of atmospheric density models for orbit prediction of space debris," in *Proceedings of the 7th European Conference on Space Debris*, Darmstadt, Germany, April 2017.

[73] J. Li, H.-X. Shen, P. Huang, Y. Chu, and H. Baoyin, "Thermospheric density estimation method using a first-order Gauss–Markov process," *Journal of Spacecraft and Rockets*, vol. 61, no. 6, 2024.

[74] Q-Tech Corporation, "New space applications add to mix of space-qualified crystal oscillators," https://q-tech.com/wp-content/uploads/Q-Tech-New-Space-White-Paper.pdf, 2018, accessed: 13 April 2026.

[75] Microchip Technology Inc., "Low earth orbit (leo) quartz oscillators," https://www.microchip.com/en-us/products/clock-and-timing/components/oscillators/space/l-series, 2020, accessed: 13 April 2026.

[76] E. Serpedin and Q. M. Chaudhari, *Synchronization in Wireless Sensor Networks: Parameter Estimation, Performance Benchmarks, and Protocols*. Cambridge University Press, 2009.

[77] J. McNeill, S. Razavi, K. Vedula, and D. Richard Brown, "Experimental characterization and modeling of low-cost oscillators for improved carrier phase synchronization," in *2017 IEEE International Instrumentation and Measurement Technology Conference (I2MTC)*, 2017, pp. 1–6.

[78] L. M. Marrero, J. C. M. Duncan, J. Querol, S. Chatzinotas, A. J. C. Carmona, and B. Ottersten, "Effects of differential oscillator phase noise in precoding performance,"

in *Advances in Communications Satellite Systems. Proceedings of the 37th International Communications Satellite Systems Conference (ICSSC-2019)*, 2019, pp. 1–15.

[79] F. Ling, "Synchronization in digital communication systems," Cambridge, 2017.

[80] S. Akhlaghi, N. Zhou, and Z. Huang, "Adaptive adjustment of noise covariance in kalman filter for dynamic state estimation," in *2017 IEEE Power and Energy Society General Meeting*, 2017, pp. 1–5.

[81] A. Patapoutian, "On phase-locked loops and kalman filters," *IEEE Transactions on Communications*, vol. 47, no. 5, pp. 670–672, 1999.

[82] C. Yuen, Y. L. Guan, and T. T. Tjhung, *Quasi-Orthogonal Space-Time Block Code*. PUBLISHED BY IMPERIAL COLLEGE PRESS AND DISTRIBUTED BY WORLD SCIENTIFIC PUBLISHING CO., 2007. [Online]. Available: https://www.worldscientific.com/doi/abs/10.1142/p524

[83] X. Chen and C. Yuen, "On interference alignment with imperfect csi: Characterizations of outage probability, ergodic rate and ser," *IEEE Transactions on Vehicular Technology*, vol. 65, no. 1, pp. 47–58, 2016.

[84] J. L. Gonzalez-Rios, E. Lagunas, H. Al-Hraishawi, L. M. Garces Socarras, and S. Chatzinotas, "In-Lab Carrier Aggregation Testbed for Satellite Communication Systems," in *30th Ka and Broadband Space Communications Conference*, 2025.

[85] G. Eappen, J. L. Gonzalez, V. Singh, R. Palisetty, A. Haqiqtnejad, L. M. Marrero, J. Krivochiza, J. Querol, N. Maturo, J. C. M. Duncan, E. Lagunas, S. Andrenacci, and S. Chatzinotas, "Optimal linear precoding under realistic satellite communications scenarios," *IEEE Open Journal of Vehicular Technology*, vol. 6, pp. 81–91, 2025.

[86] W. H. Press, S. A. Teukolsky, W. T. Vetterling, and B. P. Flannery, *Numerical Recipes in C*. Cambridge: Cambridge University Press, 1992, iSBN 0–521–43108–5.

[87] J. G. Proakis and D. K. Manolakis, *Digital Signal Processing (4th Edition)*. USA: Prentice-Hall, Inc., 2006.